Interfacial behaviour of β-sheet forming antimicrobial peptide GL13K

Hala Youssef

A Thesis
In the Department
of
Chemistry and Biochemistry

Presented in Partial Fulfillment of the Requirements
for the Degree of Doctor of Philosophy (Chemistry) at
Concordia University
Montréal, Québec, Canada

May 2019

CONCORDIA UNIVERSITY

School of Graduate Studies

This is to certify that the thesis prepared

By: Hala Youssef

Entitled: Interfacial behaviour of β-sheet forming antimicrobial peptide GL13K

and submitted in partial fulfillment of the requirements for the degree of

Doctor of Philosophy (Chemistry)

complies with the regulations of the University and meets the accepted standards with respect to originality and quality.

Signed by the final examining committee:

_____ Chair
Dr. Michael Sacher

_____ External Examiner
Dr. Michel Lafleur

_____ External to Program
Dr. David Kwan

_____ Examiner
Dr. Louis Cuccia

_____ Examiner
Dr. Paul Joyce

_____ Thesis Supervisor
Dr. Christine DeWolf

Approved by

_____
Dr. Yves Gélinas, Graduate Program Director

2019/06/19

_____
Dr. André Roy, Dean, Faculty of Arts and Science

ABSTRACT

Interfacial behaviour of β-sheet forming antimicrobial peptide GL13K

Hala Youssef, Ph. D.

Concordia University, 2019

Antimicrobial peptides (AMPs) have been proposed as promising alternatives to conventional antibiotics. They are highly selective and efficient bactericidal agents that are already present as elements of innate immunity. GL13K is a synthetic peptide, derived from residues 141-153 of the human parotid secretory protein, and it is an AMP that is bactericidal against Gram-positive and Gram-negative bacteria. Previous biophysical studies with this peptide showed that it selectively forms β-sheets in the presence of anionic membranes and targets membranes via the carpet method.

In this thesis, initial studies focused on the surface behaviour of GL13K to determine whether it has the propensity to form amyloidic structures. Once it was established that GL13K does not aggregate into amyloidic fibrils at the air/water interface or when transferred to solid support, studies with anionic monolayers of varied membrane fluidity were conducted using dioleoylphosphatidylglycerol (DOPG) and mixed DOPG:cholesterol and DOPG:diphytanoylphosphatidylglycerol (DPhPG) films. Both cholesterol and DPhPG, a branched, anionic lipid, lower the permeability of membranes, but only cholesterol increases membrane viscosity. These studies showed that membrane viscosity plays a greater role in the prevention of peptide insertion into membranes. This suggests that cholesterol may contribute to the protection of eukayotic cells from AMPs by attenuating peptide insertion.

Some bacteria have developed resistance to AMPs by upregulating the production of lysyl-phosphatidylglycerol (LPG) to mask the negative charge on their membranes. Model membranes consisting of dipalmitoylphosphatidylglycerol (DPPG) and mixtures of DPPG and DP3AdLPG, a stable analogue of LPG, were used to determine how this lysylation alters GL13K behaviour at the air/water interface. The functionalization of the headgroup attenuates the formation of crystalline β-sheets by disrupting the hydrogen bonding network. Peptide crystallinity appears to

increase when the peptide is bound to the headgroup region which could either attenuate activity or alter the mechanism of activity. This highlights the need for further research in this area to determine if a direct relationship between peptide crystallinity and function exists.

ACKNOWLEDGEMENTS

First and foremost, I would like to express my deepest gratitude to my supervisor Dr. Christine DeWolf for her endless support. I do not know where I would be without her guidance and encouragement.

Next, I would like to thank Dr. Rolf Schmidt for his assistance these past four years. He has been a constant throughout my graduate studies, from training, to troubleshooting, to the many, many discussions we have had over the years.

I am profoundly grateful to Dr. Gerald Brezesinski for agreeing to host me at the MPIKG. I truly appreciated the opportunity to learn from him.

I would like to thank Dr. Christian Salesse for teaching me how to analyze and interpret PM-IRRAS data and for our discussions, Dr. Wei Bu and Dr. Binhua Lin for our discussions about x-ray reflectivity and GIXD, and Dr. Vinod Balhara for his previous work with the GL13 peptides.

I am also grateful to Dr. Louis Cuccia and Dr. Paul Joyce for agreeing to be on my committee and their insightful suggestions.

I would like to acknowledge the financial support provided by NSERC, FQRNT, CQMF, and MITACS.

To my group members throughout the years (Abdullah, Erum, Renaud, Sahana, Ruxandra, Daisy, Shirin, Janet, Javier, Jocelle, Jennifer), thank you for all the support and the laughs. You helped make our lab a wonderful place to be.

Finally, I would like to thank my family for a lifetime of unconditional love and support. It has been a long road, and I know I could not have done it without my mother in particular. Thank you for never giving up on me.

I wish my dad and grandfather were here to see this.

CONTRIBUTION OF AUTHORS

Chapter 3- The interfacial self-assembly of antimicrobial peptide GL13K into non-fibral crystalline β-sheets

This manuscript is a communication that will be submitted to Colloids and Surfaces B: Biointerfaces with the following authors:

Youssef, H., Dewolf, C. E.

Author contributions: I conducted all of the experimental work, data analyses, and prepared the manuscript. My supervisor, C. DeWolf, assisted with experimental design, data interpretation and manuscript writing.

Chapter 4- Membrane fluidity governs the insertion of the antimicrobial peptide GL13K

This manuscript will be submitted to *Biochimica et Biophysica Acta- Biomembranes* with the following authors:

Youssef, H., Dewolf, C. E.

Author contributions: I conducted all of the experimental work, data analyses, and prepared the manuscript. My supervisor, C. DeWolf, assisted with experimental design, data interpretation and manuscript writing.

Chapter 5- Lysyl headgroup modifications disrupts the organization of antimicrobial peptides bound to the membrane interface

The data presented are from a manuscript-in-preparation with the following authors:

Youssef, H.; Harvey, R; Woelk, C.; Brezesinski, G.; Dewolf, C. E.

Author contributions: I conducted the experimental work, data analyses, data interpretation and wrote the first draft of the manuscript. C. Woelk and C. Harvey synthesized and provided the lipids and assisted with synchrotron data collection. G. Brezesinski designed the research plan,

assisted with synchrotron data collection and data analysis. C. DeWolf contributed to data interpretation and manuscript writing.

Table of Contents

List of figures

List of tables

List of abbreviations

AFM	Atomic force microscopy
AMP	Antimicrobial peptide
AMR	Antimicrobial resistance
APD	Antimicrobial peptide database
BAM	Brewster angle microscopy
BPI	Bactericidal/permeability increasing protein
CD	Circular dichroism
Ch	Cholesterol
DOPC	1,2-dioleoylphosphatidylcholine
DOPG	1,2-dioleoylphosphatidylglycerol
DP3AdLPG	3-aza-dehydroxyl lysyl-phosphatidylglycerol
DPhPC	1,2-diphytanoylphosphatidylcholine
DPhPG	1,2-diphytanoylphosphatidylglycerol
DPPC	1,2-dipalmitoylphosphatidylcholine
DPPG	1,2-dipalmitoylphosphatidylglycerol
FTIR	Fourier transform infrared spectroscopy
GIXD	Grazing incidence x-ray diffraction
GUVs	Giant unilamellar vesicles
hPSP	Human parotid secretory protein
IAPP	Islet amyloid polypeptide
IR	Infrared
IRRAS	Infrared reflection absorption spectroscopy
LB	Langmuir-Blodgett

LBP	Lipopolysaccharide-binding protein
LPG	Lysyl-phosphatidylglycerol
LPS	Lipopolysaccharide
LTA	Lipoteichoic acid
LUVs	Large unilamellar vesicles
MCT	Mercury cadmium telluride (detector)
MDR	Multidrug-resistant
MprF	Multiple peptide resistance factor
NMR	Nuclear magnetic resonance
PA	Phosphatic acid
PC	Phosphatidylcholine
PE	Phosphatidylethanolamine
PG	Phosphatidylglycerol
PI	Phosphatidylinositol
PM-IRRAS	Polarization modulated-infrared reflection absorption spectroscopy
POPC	1-palmitoyl-2-oleoylphosphatidylcholine
POPG	1-palmitoyl-2-oleoylphosphatidylglycerol
PrP	Prion proteins
PS	Phosphatidylserine
SLBs	Supported lipid bilayers
SM	Sphingomyelin
sPLUNC	Short palate, lung and nasal epithelium clone
TRXF	Total reflection x-ray fluorescence
UV	Ultraviolet
WHO	World Health Organization

XR	X-ray reflectivity

Chapter 1. Introduction

1.1. Motivation

The abuse of antibiotic prescription and administration in humans as well as in livestock and agriculture has resulted in pathogens that have developed multiple mutations rendering them resistant against various antibiotics.[1] In the race to treat infections by these pathogens, higher dosages of these antibiotics are being administered and the escalation is increasing the cost of available treatments while reducing their efficacy.[2,3] The international post-antibiotic era is imminent and has already begun in many developing countries, with the example of India where the majority of adults are carriers of β-lactam-resistant bacteria.[4] The World Health Organization (WHO)'s most recent global report shows highly resistant bacteria in most WHO regions, and the list of antibiotic-resistant pathogens is long and continuing to grow as these pathogens are becoming multidrug-resistant (MDR) and spreading quickly.[5] It was projected that within the next thirty years, antimicrobial resistance (AMR) will cause more deaths than cancer (Figure 1.1).[6] One of the promising fields of study to find alternative treatments is antimicrobial peptide research.

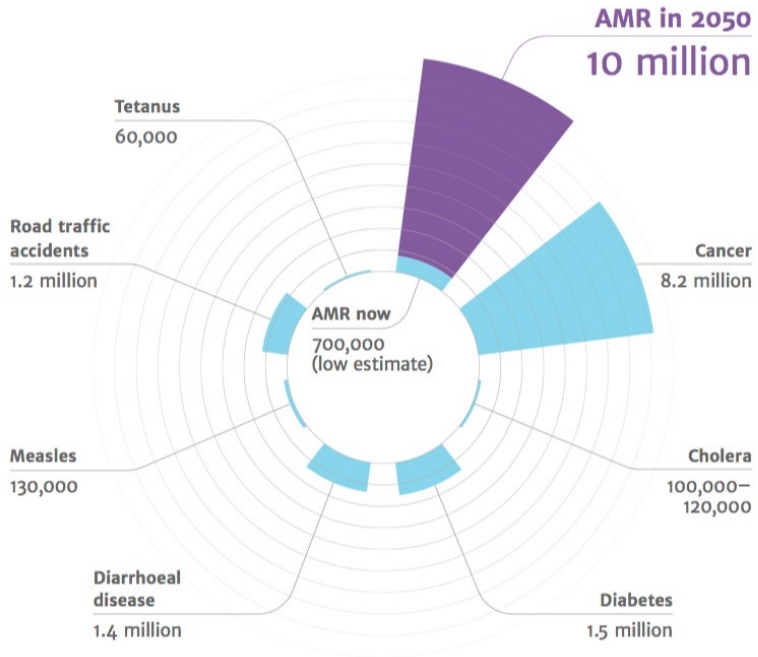

Figure 1.1 Projected number of deaths due to antimicrobial resistance in 2050[6]

1.2. Antimicrobial peptides

Natural antimicrobial peptides are an integral part of innate immunity in both the plant and animal kingdoms as they are effective against a large range of pathogens, including bacteria, fungi, viruses and protozoa.[7] They are typically cationic, ranging between 10 and 100 amino acids, and they can fold into amphipathic structures in the presence of bacterial membranes. These amphipathic structures can be α-helices, β-sheets, a mixture of α-helices and β-sheets, or unstructured (Figure 1.2).[8]

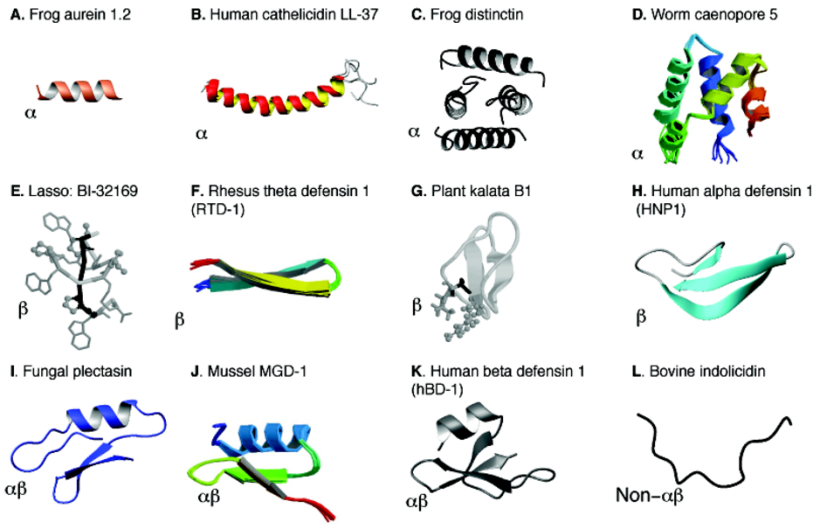

Figure 1.2 Examples of AMPs from each family, where their classification is indicated on the bottom left of each panel[8]

There are various databases in which AMPs have been compiled including the Antimicrobial Peptide Database (APD). The APD is a database that has been manually curated and includes peptides of known, or partially known, sequences that have been demonstrated to be antimicrobial. To date, 3117 antimicrobial peptides have been registered with the University of Nebraska Medical Center (UNMC)'s Antimicrobial Peptide Database (APD). The vast majority of these peptides contain fewer than 100 amino acids and are from natural sources, though they have included some synthetic peptides and peptides of significance that are larger than 100 residues.[9]

1.2.1. Activity α-helical vs. β-sheet forming AMPs

Membrane disrupting AMPs tend to adopt amphipathic secondary structures and the most common AMP secondary structure is α-helical. Many of the well-known AMPs fall into this category including magainin I,[10] gramicidins A,[11] B, and C,[12] and melittin.[13] There are far fewer AMPs that fold into β-sheets, and most of those require disulfide bridges to maintain their secondary structure. Arenicin-1, protegrin-1, and tachyplesin are AMPs that form β-hairpins which are stabilized by disulfide bridges.[14–16] Capistruin and the lariatin peptides have disulfide bridges that stabilize the formation of a lasso-like structure, where the β-sheet holds the lasso together and greatly contributes to the stabilization of the overall structure.[17,18] Other β-sheet-forming peptides are cyclic e.g. gramicidin S, defensin, and labaditin.[19–21] While most AMPs are unstructured in solution and undergo a conformational change upon interaction with a membrane, cyclic peptides are structured in solution which may contribute to their higher bactericidal efficiency.[22] The forced conformation induced by disulfide bridges has also been shown to be important for bactericidal activity.[22–24]

1.2.2. Functional relationship between AMPs and amyloids

β-sheet-forming amyloids have been linked to numerous neurodegenerative diseases including Parkinson's disease, Alzheimer's disease, spongiform encephalopathies (mad cow disease), and type II diabetes.[25] Amyloids have antimicrobial properties, where the intermediate amyloid oligomers were more effective than the monomers or the fibrils.[26–28] While there is no distinct sequence conservation among amyloid β (Aβ) peptides, prion proteins (PrP), and islet amyloid polypeptide (IAPP), all three form the characteristic cross-β structure.[29] It has been proposed that there is a functional link between antimicrobial peptides and amyloids. Amyloid fibril formation appears to be dependent on a nucleation seed[30–32] and self-complementing β-sheets that form interdigitated hydrophobic zippers.[26,29] However, experimental and computational findings suggest that a propensity to form β-sheets does not necessarily imply fibril formation.[33,34] While both AMPs and amyloids contain a larger proportion of hydrophobic residues, amyloids are not usually charged. While de la Paz *et al.* even suggested that high charge prevents fibril formation,[33] protegrin-1 was found to undergo amyloidosis and form fibrils at a much faster kinetics than Aβ 1-42[35] despite its +7 net charge.

1.3. AMP mechanisms of attack

Initially, three AMP mechanisms of attack were proposed: the barrel-stave, toroidal pore, and carpet mechanisms (Figure 1.3).[36] They all begin with the accumulation of the peptide in the outer leaflet, parallel to the membrane. The barrel-stave and toroidal pore mechanisms are similar: after accumulation in the membrane to a threshold concentration, the peptides reorient to form transmembrane pores that cause bacterial death. The main difference between the two mechanisms is that the pores formed by the toroidal pore mechanism are composed of both peptides and lipids.

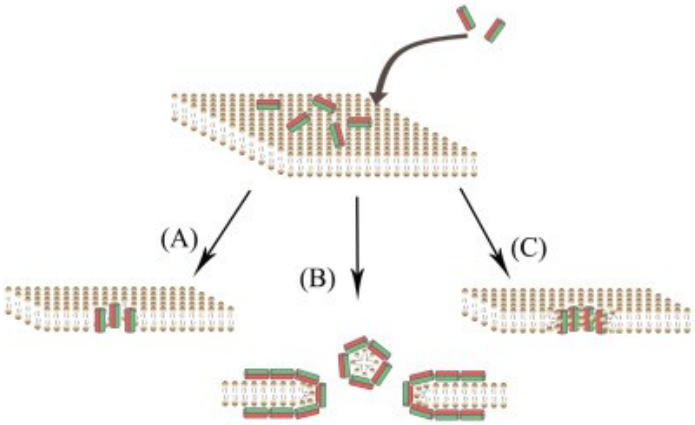

Figure 1.3 Traditional AMP mechanisms of attack, showing accumulation of peptide in the outer leaflet, and the barrel-stave (A), carpet (B), and toroidal pore (C) mechanisms[37]

The third mechanism of attack is the carpet mechanism where the AMPs remain parallel to the membrane until the saturation limit at which point they cause fragmentation of the outer leaflet and, subsequently, membrane disruption. It is referred to as the detergent mechanism as there is no pore formation only local 'transient' pores. As the library of known antimicrobial peptides has grown, additional mechanisms of attack have been proposed (Figure 1.4). Though these mechanisms appear to be variations of the three main mechanisms, they vary significantly from each other. These 'new' mechanisms include the disordered toroidal pore,[38] the membrane thickening,[39] charged lipid clustering,[40] non-bilayer intermediate,[41] and the non-lytic membrane depolarization[42] mechanisms. No direct correlation has been established between peptide secondary structure and mechanism of interaction.

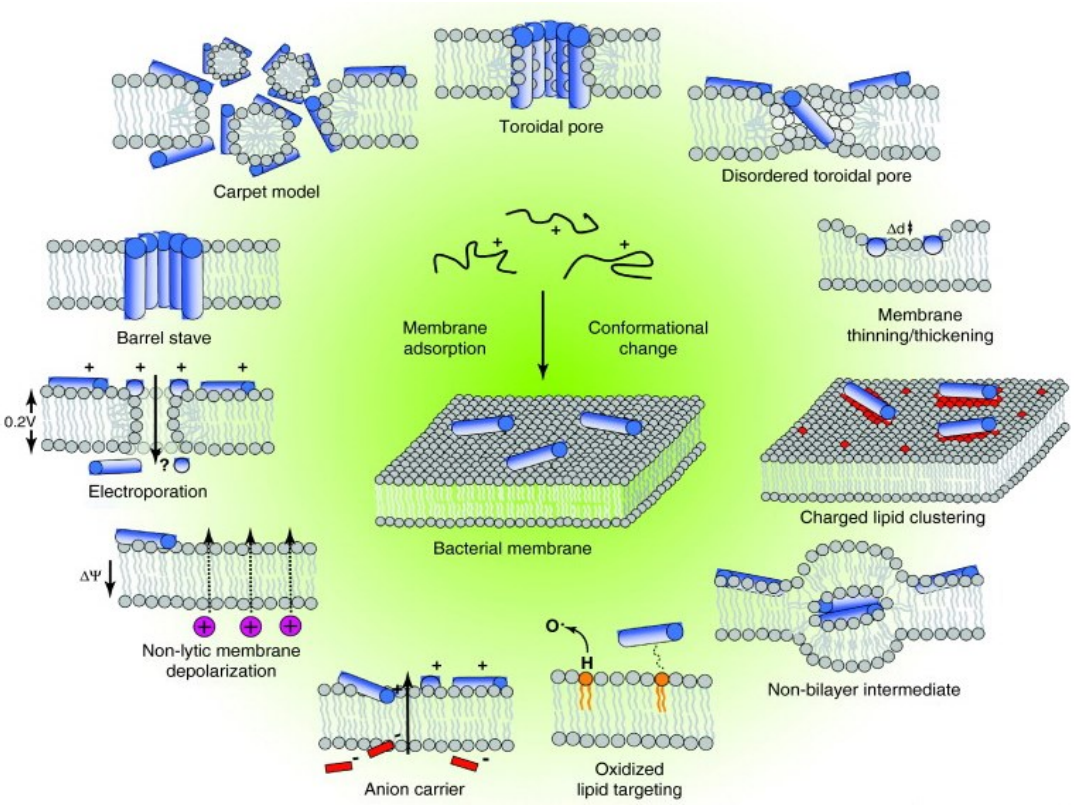

Figure 1.4 Other proposed AMP mechanisms of attack[43]

1.4. Human parotid secretory and the GL13 peptides

The human parotid secretory protein (hPSP), otherwise known as short palate, lung and nasal epithelium clone 2 (sPLUNC 2) or human salivary protein BPIFA2,[44] is a human salivary protein that is structurally related to the bactericidal/permeability increasing protein (BPI), the cholesteryl ester transport protein, and the lipopolysaccharide-binding protein (LBP), with a sequence similarity of 22%.[45] Bactericidal activity assays showed that it binds lipopolysaccharide (LPS) and is bacteria-agglutinating.[45,46] By using the sequence of hPSP and the known structure of BPI, various peptides were made with the goal of designing a new synthetic antimicrobial peptide.

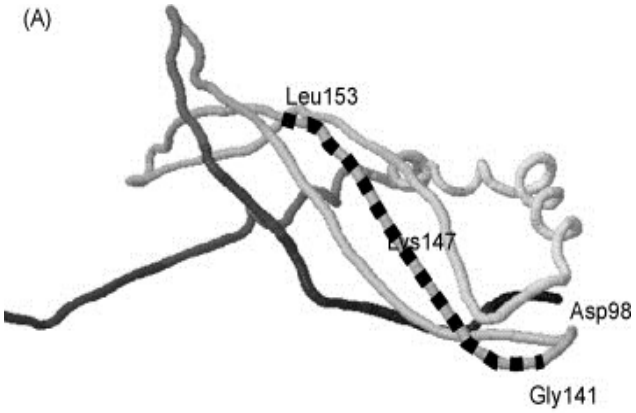

1 *MLQLWKLVLL CGVLTGTSES* LLDNLGNDLS NVVDKLEPVL HEGLETVDNT LKGILEKLKV
61 DLGVLQKSSA WQLAKQKAQE AE**KLLNNVIS KLL**PTNTDIF GLKISNSLIL DVKAEPIDDG
121 KGLNLSFPVT ANVTVAGPII GQIINLKASL DLLTAVTIET DPQTHQPVAV LGECASDPTS
181 ISLSLLDKHS QIINKFVNSV INTLKSTVSS LLQKEICPLI RIFIHSLDVN VIQQVVDNPQ
241 HKTQLQTLI

Figure 1.5 Structure and sequence of hPSP, where the sequence used in the design of the GL13 peptides has been underlined[46]

Various peptides were designed based on the known behavior of BPI and BPI peptides, and the C-terminus of the GL13 peptides was amidated to increase their positive charge. The peptide GL13K was designed based on the hemolytic, hemoagglutinating, and bacteria-agglutinating characterization of the wild-type sequence peptide GL13NH2.[47]

Table 1.1 shows the sequences and some properties of the three GL13 peptides of interest. GL13NH2 is positions 141-153 of PSP's sequence with an amide-functionalized carboxy-terminus. The modification of GL13NH2's aspartate at position eleven to an asparagine increased the net positive charge of the peptide from +1 to +2 (Table 1.1) and weakened its selectivity (Table 1.2). The residues in GL13NH2 at positions two, five, and eleven were changed to lysine to increase the net positive charge of GL13K. These modifications induced bactericidal activity in GL13K. GL13K is effective against bacteria of very different membrane compositions while being neither hemolytic nor hemoagglutinating.[47]

Peptide	Sequence	Charge at physiological pH	pI
GL13NH2	GQIINLKASLDLL-NH_2	+1	10.1
GL13D/N	GQIINLKASLNLL-NH_2	+2	14
GL13K	GKIIKLKASLKLL-NH_2	+5	14

Table 1.1: Properties of the GL13 peptides

Biological activity	GL13NH2	GL13D/N	GL13K
Bactericidal	**Yes**	**Unknown**	**Yes**
Effective against biofilms	**No**	**Unknown**	**Yes**
Inhibits TNF-α secretion	**Yes**	**Unknown**	**Yes**
Hemolytic	**No**	**Yes** (Not in the presence of 5% serum)	**No**
Hemaglutinating	**Yes** (Not in the presence of 5% serum)	**Yes**	**No**
Bacterial agglutinating	**Yes**	**Yes**	**No**

Table 1.2 Behaviour of GL13 peptides in biological systems[46–48]

1.4.1. Biophysical characterization of GL13 peptides

The structural behaviour of GL13NH2, GL13D/N, and GL13K has been studied by various biophysical techniques, with GL13K being the most studied due to its potential as an antibacterial therapy. While GL13K is highly soluble and remains unstructured in solution, GL13D/N and GL13NH2 are much more hydrophobic and, subsequently, fold into both α-helices and β-sheets in solution.[49] This pre-folding appears to drive membrane insertion and lower the peptide's specificity. GL13K, on the other hand, is highly specific for anionic membranes and does not fold in the presence of zwitterionic membranes.[50]

1.5. Compositional differences between bacterial and eukaryotic membranes

1.5.1. Phospholipid composition and membrane charge

One of the most significant differences between bacterial and eukaryotic membranes is the charge of the outer membrane. While the proportions of negatively-charged phosphatidylglycerol (PG) headgroups and phosphatidylethanolamine (PE) vary between Gram-positive and Gram-negative bacteria, bacterial plasma membranes consist predominately of anionic lipids.[7,51,52] The cell wall of Gram-positive and the outer membrane of Gram-negative bacteria are also both anionic due to the presence of lipoteichoic acid (LTA) and lipopolysaccharide (LPS), respectively (Figure 1.6).[51] Eukaryotic membranes, on the other hand, are predominately zwitterionic. The main components are phosphatidylcholine (PC), phosphatidylethanolamine (PE), phosphatidylserine (PS), phosphatidylinositol (PI) and phosphatidic acid (PA).[53]

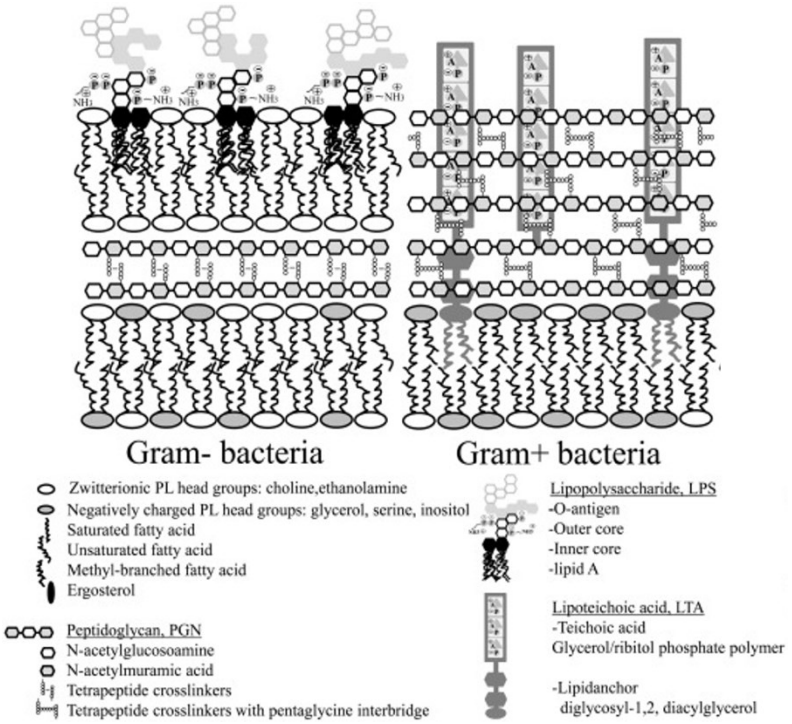

Figure 1.6 Structural differences between the membranes and bacterial envelopes of Gram-positive and Gram-negative bacteria[51]

Another significant difference between bacterial and eukaryotic membranes is that eukaryotic membranes are significantly more rigid due to the presence of cholesterol and sphingomyelin which increases the ordering and packing density of the bilayers.[54]

1.5.2. Cholesterol in model membranes

Cholesterol (Ch) is a known membrane rigidifier. Cholesterol concentration in eukaryotic membranes varies in the 20-40 mol% range.[55,56] The incorporation of cholesterol into membranes has been shown to decrease membrane permeability and hinder the incorporation of peptides into the lipid bilayer.[57–59]

Due to its structure (Figure 1.7), cholesterol intercalates within the hydrophobic tails of the lipid bilayer with its single hydroxyl functional group oriented into the headgroup region.[60] The interaction of the rigid sterol ring with the acyl chains reduces the mobility of neighboring lipids and increases the spacing between the lipid headgroups.[61] Additionally, cholesterol causes de-wetting of lipid head groups, altering the dipole of the membrane.[62] While there is experimental evidence that cholesterol only forms condensed films at a fixed stoichiometry independent of

cholesterol content,[63,64] other studies have shown the formation of specific, ordered cholesterol/phospholipid superlattices.[56,65–67] The miscibility of cholesterol in membranes varies depending on the lipid acyl chain length and level of saturation as they both contribute to transition temperature.[60] The miscibility of cholesterol is also influenced by headgroup structure.[68] In fluid membranes, cholesterol condenses the acyl chains via short-range (local) ordering, while it fluidizes liquid-ordered membranes by disrupting long-range (global) order.[56,60,67,69,70] Cholesterol can increase the viscosity of DOPC membranes by ~16% when the mole fraction of cholesterol ($\chi_{cholesterol}$) is 0.4.[71]

1.5.3. Studies with branched phospholipids

While cholesterol may not be present in bacterial membranes, branched lipids, particularly iso- and anteiso-branched lipids, are found in abundance.[72] The branched lipid that will be used in this study is diphytanoylphosphatidylglycerol (DPhPG), as the methyl-branched chains are found in archaebacterial membranes and not mammalian membranes (Figure 1.7).[73]

These lipids are chemically stable synthetic archael lipids that can form stable bilayers.[74] A molecular dynamics study comparing diphytanoylphosphatidylcholine (DPhPC) with dipalmitoylphosphatidylcholine (DPPC) concluded that DPhPC bilayers have slower rotational, translational, and chain-wobbling motions but faster headgroup wobbling and rotation.[61] X-ray and neutron scattering and permeability studies on DPhPC bilayers, and they concluded that DPhPC's bilayer thickness was similar to that of DOPC and that the branching in DPhPC lowers water permeation through the hydrocarbon region of the bilayer.[73–75] While Hung *et al.* proposed that these methylene groups on the lipid chains interdigitate,[76] studies with giant unilamellar vesicles (GUVs) and supported bilayers concluded that phytanoyl membranes are highly fluid and have very disordered acyl chains.[77] Differential thermal analyses confirmed that DPhPC bilayers do not form gel phases over the range from -120 to 120 °C,[78] and neutron reflectivity showed that the phytanoyl lipids occupy a larger volume per lipid molecule than paltimoyloleoylphosphatidylcholine (POPC) due the methyl branching on the acyl chains.[79] Diphytanoylphospholipids have been used to study AMP insertion mechanisms[80–83] despite the effect of branching on peptide insertion not being well defined.

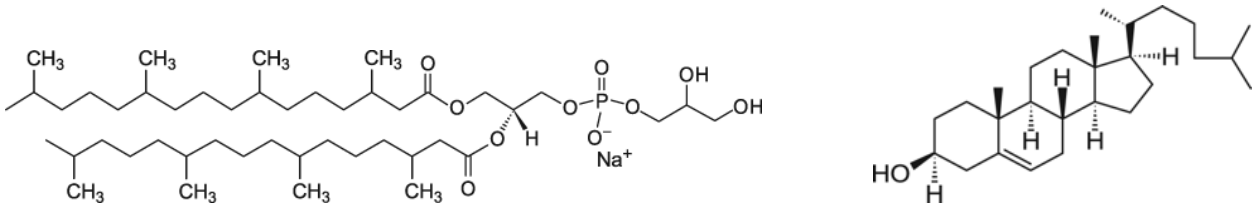

Figure 1.7 Lipid structures of 1,2-diphytanoyl-*sn*-phosphatidylglycerol (DPhPG) and cholesterol (Ch)

1.6. Bacterial resistance to AMPs

In the early years of antimicrobial peptide research, it was speculated that bacteria would not develop resistance to AMPs as this would require that bacteria develop mechanisms by which to modify their membranes.[84] It was later discovered that bacteria could develop resistance to AMPs, and the mechanisms by which they have become resistant are diverse and vary from species to species. Some examples include upregulation of protease production or modulation and subsequent masking of the negative charge of their membranes via D-alanylation of teichoic acids, acylation of the glycerol of PG headgroups, or amino-functionalization of phospholipids.[52,85–87] Of these, the most commonly studied amino-functionalization is the lysylation of phosphatidylglycerol headgroups.

1.6.1. The role of lysyl-phosphatidylglycerol

When resistant strains of *S. aureus* undergo stress e.g. growth at lower pH or in the presence of AMPs, they upregulate the multiple peptide resistance factor gene (*MprF*) which encodes the enzyme aminoacyl-PG synthase which is responsible for the lysyl-modification of the negatively-charged phosphatidylglycerol headgroups and translocation of the lysyl-phosphatidylglycerol (LPG) to the outer leaflet of the plasma membrane.[88,89] Rehal *et al.* found that the proportion of lysyl-phosphatidylglycerol in the membranes of methicillin-resistant strains of *S. aureus* (MRSA) was greater in cultures grown at pH 5.5 as compared to those grown at pH 7.4.[90] The cultures grown at pH 5.5 contained ~55% LPG, while those grown at pH 7.4 contained ~30%.

This modification shifts the net charge of LPG to either +1 or to net neutral, depending on the protonation state of the phosphate (pKa ~3), the alpha amine (pKa ~6.5), and the epsilon

(terminal) amine (pKa ~10).[91–93] Rehal *et al.* proposed that the epsilon amine loops up to interact with the phosphate of the LPG, a neighboring cardiolipin or DPPG in the membrane.[93] Due the labile nature of the ester linkage in the lysyl-phosphatidyl headgroup,[93,94] a stable synthetic analogue, 1,2-dipalmitoyl-3-azo-dehydroxy lysyl-phosphatidylglycerol (DP3adLPG), was synthesized (Figure 1.8). Previous studies used model membranes comprising dipalmitoylphosphatidylglycerol (DPPG), DP3adLPG, and cardiolipin to model the membrane of *Staphylococcus aureus.*[93]

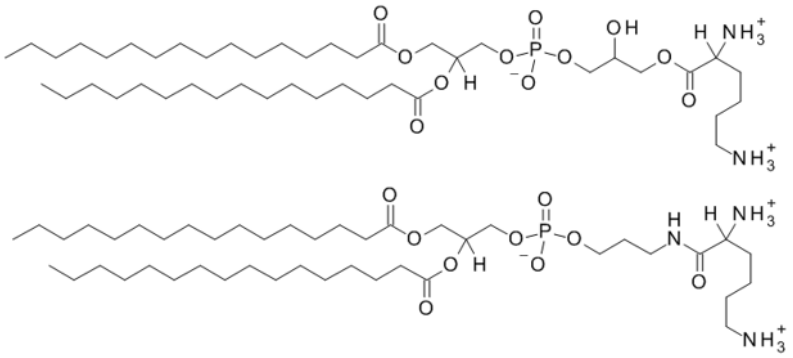

Figure 1.8 Chemical structures lysyl-phosphatidylglycerol (LPG) and 3-aza-dehydroxyl lysyl-phosphatidylglycerol (DP3AdLPG)

1.6.2. Effect of lysylation on AMP activity

Most antimicrobial peptides are cationic peptides whose specificity is in part due to electrostatic interactions between their charged residues and the anionic phospholipids of the outer leaflet.[95] The charge screening that occurs when LPG ion-pairs with these anionic phospholipids attenuates AMPs interaction with the lipid membrane. It has also been suggested that the LPG further inhibits the penetration of AMPs by decreasing the membrane permeability to cationic species.[87]

Rehal *et al.* found that at physiological pH, LPG was able to attenuate the activity of magainin. Andrä *et al.* studied the effect of LPG on the behaviour of both helical and β-sheet-forming peptides and found that the functionalization had very different effects on NK-2, melittin, or arenecin, the first two of which fold into helices while the third is a β-hairpin.[91] They found that while melittin was not affected by the lysyl headgroup, NK-2 was rendered inactive as even its

membrane binding capabilities were hindered.[91] Both of these peptides are of similar length (26 and 27 residues, respectively) but they differ in their net charge. While melittin has a net charge of +6, NK-2 has a net charge of +10.[96] This higher concentration of positive charge over a similar surface area (as they both form helices) may be the reason why NK-2 cannot sufficiently accumulate at the lipid interface to insert transmembrane. Arenicin, a 21-residue peptide with a +6 charge, was strongly modulated by the lysyl headgroup.[97] However, unlike NK-2, arenicin could still bind to the interface.

1.7. Specific Aims

The aim of this thesis is to develop a better understanding of the interfacial folding behaviour of GL13K so that it's secondary structure, interfacial orientation and organization can be correlated with its mechanism of action and activity. This understanding will be achieved by studying GL13K at the air/water interface in the absence and presence of a lipid monolayer, the latter to represent the outer leaflet of bacterial membranes.

In the first manuscript (Chapter 3), we studied the surface behaviour of GL13K to establish an understanding of the peptide's interfacial activity in the absence of phospholipids. This manuscript is of particular importance given the recent findings of β-sheet forming AMPs that exhibit amyloid behaviour at physiological pH. Experiments coupling the air/water interface with spectroscopic and diffraction techniques were conducted to determine whether GL13K forms fibrils at interfaces. The relevant theory of the techniques will be described in Chapter 2.

In the second manuscript (Chapter 4), we investigated the interfacial behaviour of GL13K when interacting with anionic model membranes. In previous work by the DeWolf group, the selectivity of GL13K was examined by introducing cholesterol into anionic and zwitterionic bilayers at 40 mol%.[47] To elucidate whether the effect observed was induced by the higher viscosity of lower permeability of the DOPG:Ch 60:40 membrane, four lipid systems were studied and compared. These included DOPG, DOPG:Ch mixtures and a DOPG:DPhPG mixture. Varying the model membrane composition enabled us to probe the effect of membrane viscosity on lipid-peptide interactions.

In the final manuscript (Chapter 5), the role of membrane composition modification as a mechanism of antimicrobial resistance were investigated. This contribution is specifically focused on the molecular mechanisms of resistance conferred via the lysylation of the phosphatidylglycerol headgroup. Two representative model membranes were used, namely a 1:2 and 1:1 mixture of a synthetic lysylphospholipid analogue, DP3AdLPG, and DPPG. The impact on lipid chain organization, peptide binding and insertion were investigated using interfacial spectroscopy and x-ray scattering methods. In addition to the conclusions that can be drawn regarding AMPs at interfaces, we demonstrated that ion displacement measurements using total reflection x-ray fluorescence (TRXF) provided a complementary, indirect method for monitoring peptide binding.

Chapter 2. Experimental Techniques

The behavior of GL13K at interfaces (both air/water and lipid interfaces) was studied using Langmuir monolayers and the surface-specific characterization techniques which are outlined below.

2.1. Langmuir monolayers

Langmuir film balances are an ideal approach for the characterization of surface behavior and the organization of lipids and peptides spread at the air/water interface. A Langmuir film balance consists of a Teflon trough and one or two Teflon barriers that are used for compression (Figure 2.1). Lipid films are typically spread from volatile solvents with high spreading coefficients (e.g. chloroform) onto a water or buffer subphase. Peptide films can either be spread from volatile solvents or aqueous solutions. Upon the evaporation of the spreading solvent, the barriers are closed and film compression begins.

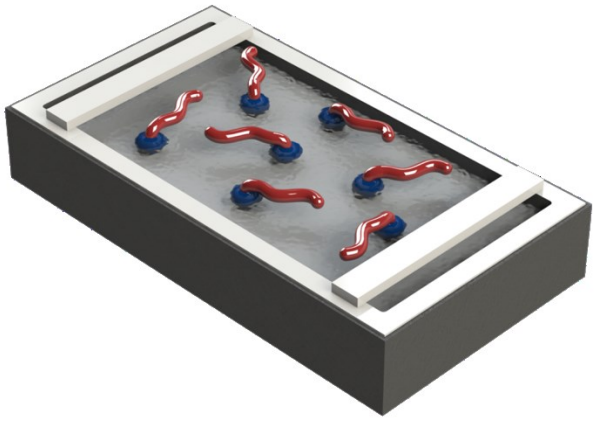

Figure 2.1 Schematic representation of lipids at the air/water interface after spreading

When a film is present, the surface tension of water is lowered, and the resulting change is reported as surface pressure. A Wilhelmy plate is used to measure the changes in surface tension, and surface pressure is the difference between the surface tension of water and the surface tension of water in the presence of a film.[98]

$$\Pi = \gamma_0 - \gamma \qquad \textbf{Equation 1}$$

Where Π is the surface pressure and γ_0 and γ are the surface tension in the absence and presence of the surface active molecules.

Compression results in an increase in surface pressure as lipid molecules are forced closer together. Surface-pressure-area isotherms are analogous to pressure-volume isotherms and can be used to determine changes in lipid organization e.g. phase transitions from gaseous to liquid expanded to condensed (Figure 2.2). Note that not all lipids exhibit all phase transitions at a given temperature.

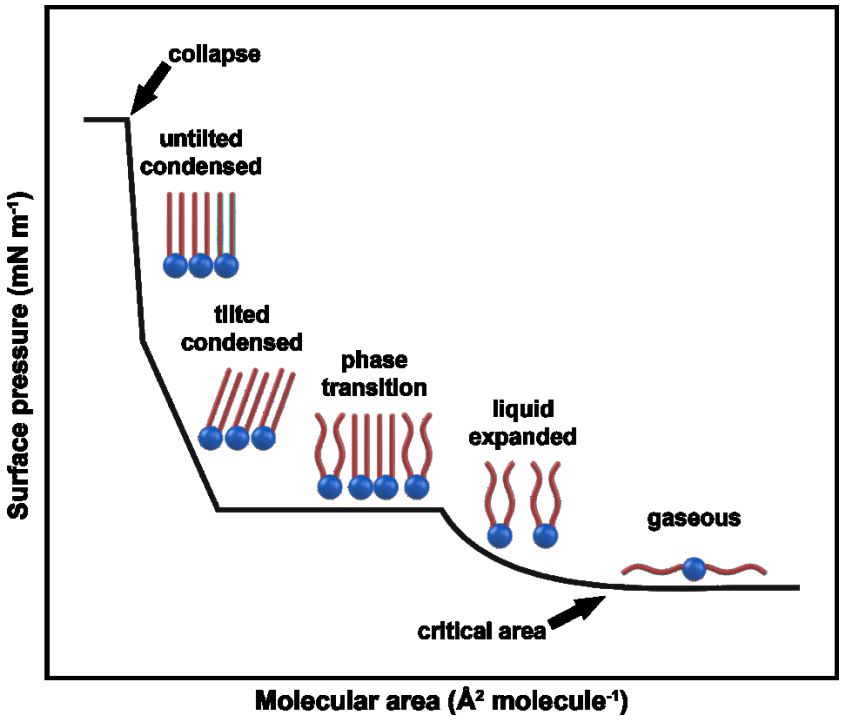

Figure 2.2 Schematic of an ideal surface pressure-area isotherm

Langmuir film balances can be coupled with spectroscopic, diffraction, and reflectivity techniques to conduct an *in situ* investigation of the interactions occurring at the air/water interface.

2.1.1. Spreading methods

Traditionally, lipids are spread from volatile solvents at sufficiently large areas that they are consider to be in a two-dimensional gaseous phase. However, in the cases where it is preferable to use very small subphase volumes e.g. for experiments when large peptide concentrations are used, use of the barriers can be forsaken and lipid can be spread until the desired pressure is obtained. In the case of the following manuscripts, the biologically-relevant target pressure is ~30 mN/m.[99] Using this approach, the full trough need not be used and an insert of smaller volume e.g. 20 mL or less can be used. It must be noted that this approach is heavily dependent upon the nature of the lipid films that are being used. Lipids that undergo a phase transition may not exhibit the same surface behavior when spread to high surface pressures. Moreover, for this method, the surface pressure can be measured but cannot be controlled due to the absence of barriers. This means that stability of the film is paramount for the success of the experiment.

2.2. Infrared reflection absorption spectroscopy (IRRAS) and polarization modulation-infrared reflection absorption spectroscopy (PM-IRRAS)

Both IRRAS and PM-IRRAS can be used to study conformational changes that occur in molecules at the air/water interface. As with any other IR technique, absorption of light by different functional groups results in distinctive bands associated with transitions between vibrational energy levels. Table 2.1 contains some of the IR absorption bands that can be observed for lipid and peptides. The CH_2 stretching bands of the lipid acyl chains are sensitive to both lipid packing and chain conformation. The shift of the asymmetric CH_2 stretching band from ~2924 cm^{-1} to 2916 cm^{-1} can be correlated to the conformational change of the lipid chains from gauche to all-trans i.e. a phase transition.[100] The symmetric CH_2 stretching band can also be used to qualitatively track conformational changes (Table 2.1).

The secondary structure of interfacial peptides can be determined based on the positions and intensities of the amide bands. The amide I (mainly C=O stretching) band and amide II (C-N stretching and N-H in-plane bending) band are sensitive to hydrogen bonding, thus the band position reflects distinct secondary structure hydrogen bond patterns (Table 2.2).[101,102]

	Vibrational mode	Frequency (cm^{-1})
Phospholipid acyl chain	CH_2 asymmetric stretch	2916-2924
	CH_2 symmetric stretch	2849-2854
Phospholipid headgroup	C=O stretch (ester)	1710-1740
	PO_2^- asymmetric stretch	1220-1250
	PO_2^- symmetric stretch	~1090
Peptide backbone	Amide I (mostly C=O stretch)	1610-1690
	Amide II (N-H in-plane bend, C-N stretch)	1520-1560
	Amide A (N-H stretch)	3200-3400

Table 2.1 Important IR vibrational bands in lipids and peptides[102]

Secondary structure	Frequency (cm^{-1})
α-helix	1642-1660
β-sheet	1615-1641
β-sheet	1672-1695
turns	1653-1691
disordered	1639-1654

Table 2.2 Assignment of amide I frequencies to peptide secondary structure[101]

IRRAS involves the reflection of an IR beam of either parallel (s) or perpendicular (p) polarization at a range of incident angles usually between 30 and 70°. The reflected light is detected at an angle identical to the angle of incidence. The orientation of interfacial molecules

can be determined based on the preferential absorption of the s or p polarized light since the ratio of the reflected light at a specific angle is dependent upon the orientation of the bond relative to the interface. Typically, IRRA spectra are presented as $-\log(R/R_0)$, where R is the reflectance of the sample and R_0 is the reflectance of the reference. IRRAS is conducted using a shuttle trough, where both troughs contain the same subphase but only the larger sample trough has the movable barriers and pressure sensor for sample measurements (Figure 2.3).

A more comprehensive description of the technique can be found in reviews by Richard Mendelsohn *et al.*[100,102]

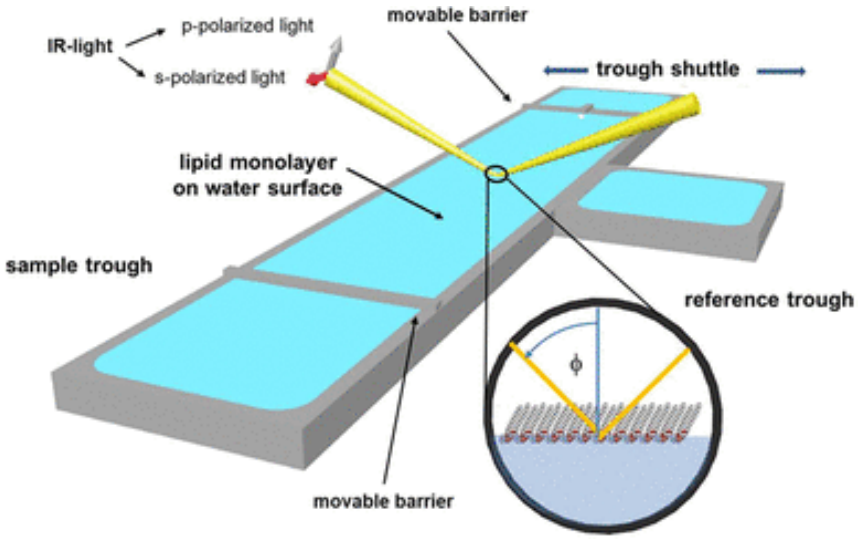

Figure 2.3 Schematic of a shuttle trough used in IRRAS experiments[103]

PM-IRRAS is a technique that was developed by Blaudez *et al.* where the polarization of the incident beam is rapidly modulated between s and p polarization and reflected from the interface.[104] A lock-in amplifier is used to electronically filter and demodulate the reflected beam. Whereas with IRRAS the IR absorption of the subphase is measured throughout the duration of the experiment whenever the trough is shuttled (see below), with PM-IRRAS, the subphase spectrum is measured once at the beginning of the experiment. The differential reflectivity spectrum is calculated using:

$$\frac{\Delta S}{S} = \frac{S(d) - S(o)}{S(o)} \qquad \textbf{Equation 2}$$

where S(d) is the signal from the sample and S(o) is the signal from the subphase.

Both techniques are surface-specific infrared techniques for which the evanescent wave decays exponentially with penetration depth. The two techniques compensate water evaporation (and subsequent water vapour interference in the 1400-1800 cm^{-1} region of spectra) differently: IRRAS does so by using a shuttle trough such that the reflection of the bare subphase can be subtracted from the reflection of the sample. This approach minimizes the contribution of water vapour to the spectra. The photoelastic modulation in PM-IRRAS removes water vapor vibrational bands from the spectra due to the isotropic nature of their absorption i.e. signals from bonds that are randomly oriented are detected with lower efficiency. It is for this reason that signal from unstructured peptide cannot be measured by PM-IRRAS.

Comparison of spectra from both techniques with simulations allows for orientation determination. In the case of PM-IRRAS data in the subsequent chapters, the orientation of GL13K will be determined by comparing with simulation spectra published by Blaudez *et al.*[105]

2.3. Surface-specific x-ray techniques

Surface-specific x-ray techniques require high energy x-rays from synchrotron sources so that the information obtained can be at the molecular level. Figure 2.4 summarizes the three surface-specific x-ray techniques that will be discussed.

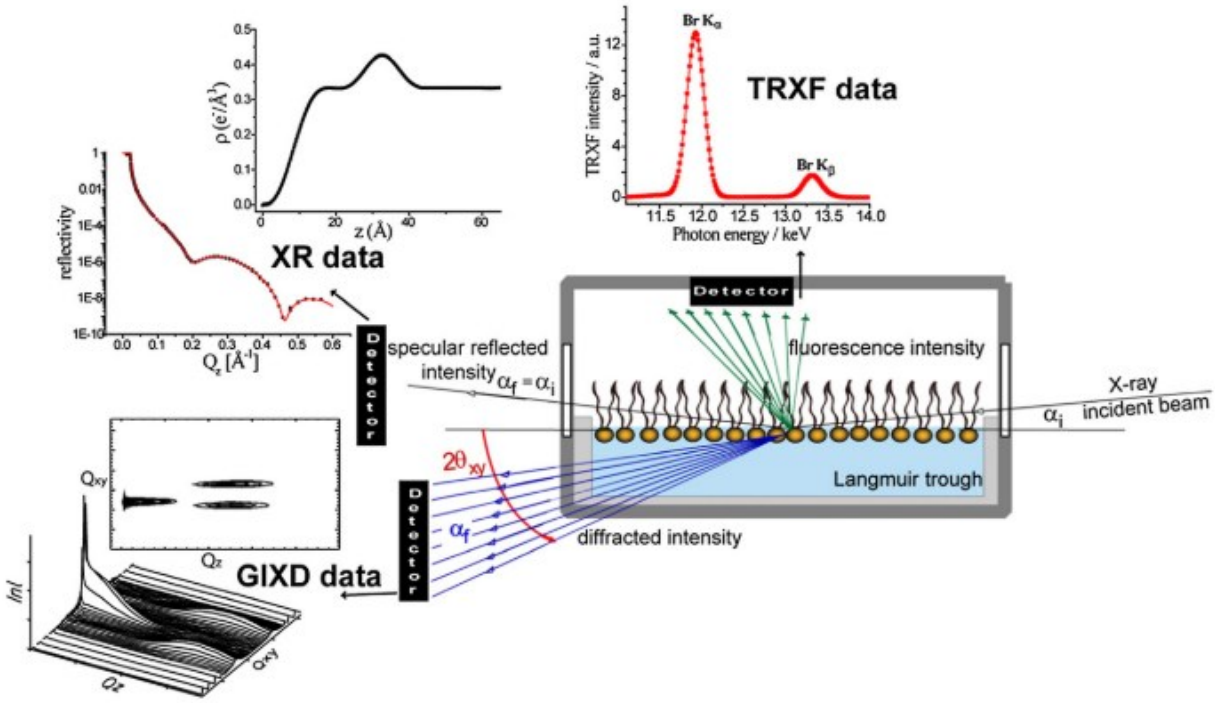

Figure 2.4 Schematic representation of the surface specific x-ray techniques at the air/water interface: grazing incidence x-ray diffraction (GIXD), x-ray reflectivity (XR), and total reflection x-ray fluorescence (TRXF)[106]

2.3.1. Grazing incidence x-ray diffraction

Grazing incidence x-ray diffraction is a technique from which information about the packing and lateral ordering of crystalline material at the air water interface can be obtained. In the case of lipids, this ordered material is typically the alkyl chains, however, peptides have been shown to form crystalline organizations as well.

For GIXD experiments, the constant incident angle α_i must be lower than the critical angle α_c, where the critical angle is a function of the intensity of the x-ray beam. The diffracted intensity is measured as a function of vertical scattering angle α_f and the horizontal scattering angle 2θ.[106] These are then converted into the in-plane and out-of-plane scattering vector components Q_{xy} and Q_z. (equations 3-7).[106,107]

$$Q_{xy} = k\sqrt{\cos^2 \alpha_i + \cos^2 \alpha_f - 2\cos \alpha_i \cos \alpha_f \cdot \cos 2\theta_{xy}} \qquad \textbf{Equation 3}$$

$$Q_{xy} \simeq k\sqrt{1 + \cos^2 \alpha_f - 2\cos \alpha_i \cos \alpha_f \cdot \cos 2\theta_{xy}} \qquad \textbf{Equation 4}$$

$$Q_{xy} \simeq 2k \cdot \sin\left(\frac{1}{2} \cdot 2\theta_{xy}\right) + Order\left(\alpha_f^2\right) \qquad \textbf{Equation 5}$$

$$Q_z = k\left(\sin \alpha_i + \sin \alpha_f\right) \qquad \textbf{Equation 6}$$

$$Q_z \simeq k \sin \alpha_f \qquad \textbf{Equation 7}$$

From the number of peaks and their positions, the unit cell can be calculated (Figure 2.5).[107,108] For lipid films, the parameters include the lattice dimensions a and b, the intervening angle γ as well as the tilt angle (relative to the normal) and tilt direction of the alkyl chain (Figure 2.6). When untilted, and in free-rotator phase, the alkyl chains frequently arrange in a hexagonal lattice

(a=b, γ=120°). When the acyl chains tilt, the unit cell elongates in the direction of the tilt (the tilt azimuth) leading to either a centred rectangular lattice (a≠b, γ=90°) or an oblique lattice (a≠b, γ≠90°).[107]

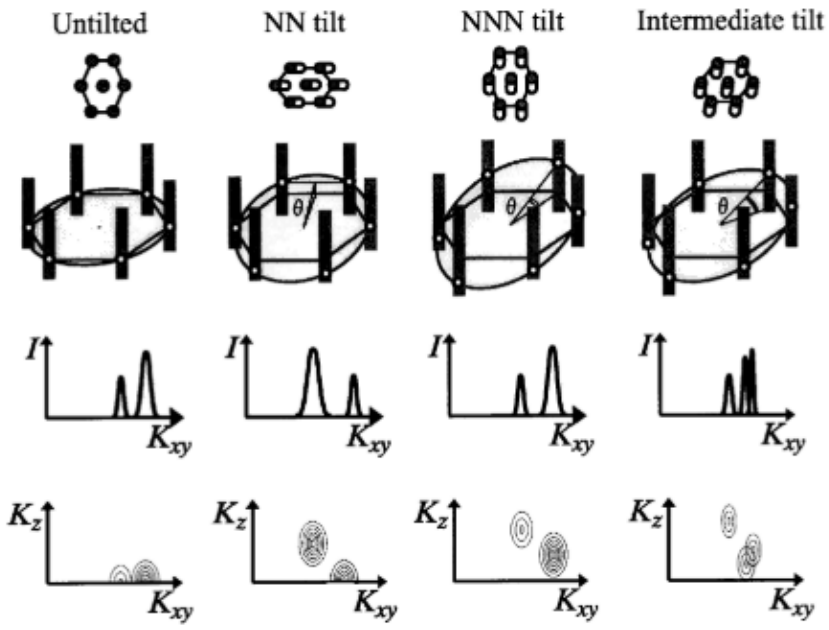

Figure 2.5 GIXD diffraction peak patterns for various tilt directions and unit cells (left to right): distorted hexagonal with untilted chains, centered rectangular unit cell with tilt towards next-neighbor (NN), centered rectangular unit cell with tilt towards next-nearest-neighbor (NNN), and an oblique unit cell with and intermediate tilt (between NN and NNN)

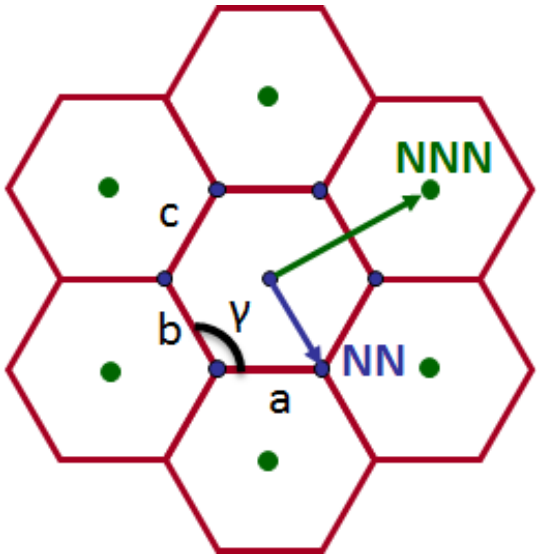

Figure 2.6 Schematic representation of unit cell parameters a, b, and γ as well as tilt directions NN and NNN.

The d-spacings (d) and correlation lengths (L_c) can be calculated using

$$d = \frac{2\pi}{Q_{xy}} \qquad \textbf{Equation 8}$$

$$L_C = 0.9\left[\frac{2\pi}{FWHM}\right] \qquad \textbf{Equation 9}$$

where, Q_{xy} is the position of the Bragg peak and FWHM is the full width of the Bragg peak at half maximum.[107]

2.3.2. X-ray reflectivity

Whereas GIXD only provides information about condensed regions of the film, x-ray reflectivity is used to generate an electron density profile that reflects the laterally-averaged vertical structure of the film. This is of great importance for localizing the peptide within the lipid monolayer i.e. whether it is interacting with the lipid headgroups or has penetrated into the acyl chain region.

X-ray reflectivity probes the electron density variation of the vertical structures at the air/water interface and is measured as a function of the vertical scattering vector component (Q_z). Unfortunately current instruments are only able to measure reflected intensity not phase, so it is not possible to directly determine the vertical structure of the film. Instead the reflectivity data are normalized relative to the Fresnel reflectivity and fit using the model-independent method and boxes of defined thickness, electron density, and roughness. The reflected intensities are measured at various α_i, such that they can be plotted in terms of Q, where α_f is the exiting angle

$$Q_z = \frac{2\pi}{\lambda}\left(\sin\alpha_f + \sin\alpha_i\right) \qquad \textbf{Equation 10}$$

$$Q_x = \frac{2\pi}{\lambda}\left(\cos\alpha_f - \cos\alpha_i\right) \qquad \textbf{Equation 11}$$

Figure 2.7 presents the electron density profile generated for the peptide gramicidin A, where the x-ray reflectivity data were fit with two boxes. The boxes become less rigid by increasing the roughness of the fit.

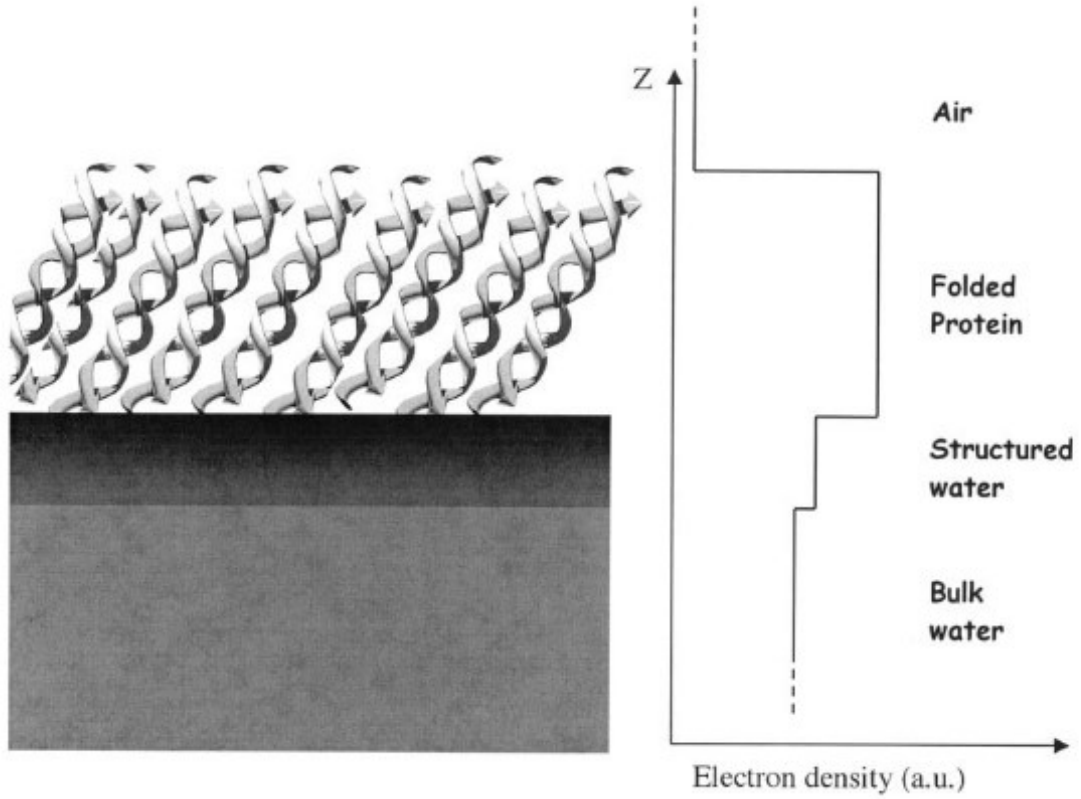

Figure 2.7 Sample electron density profile of gramicidin A at the air/water interface[109]

2.3.3. Total reflection x-ray fluorescence (TRXF)

TRXF is a relatively new technique that quantitatively measures the elemental composition of the interfacial region.[106] As with GIXD, x-ray beams interact with the interface at a grazing incidence thus limiting the depth of penetration to 8 nm from the surface. X-ray emission is measured at an offset angle. When an atom is irradiated with a photon of sufficient energy, an inner electron is ejected and the vacancy subsequently filled by an outer shell electron. This shift between from a higher energy orbital to a lower energy orbital causes the emission of quantized energy that is characteristic of the element. Detection of the distinct x-ray fluorescence enables

identification of the surface species present; the intensity is calibrated to the surface concentration and is used to quatify the relative amounts of these species. The maximum intensity of the incident x-ray beam must be greater than the emission energy of the ions or elements of interest i.e. to measure the K_α band of Br^- ions (Figure 2.4), an x-ray beam of 15 keV or greater is required.

In this work, this method is used to indirectly monitor the ionic state of the lipids by measuring the x-ray fluorescence emission of the counterions that are attracted to the interface.

2.4. Brewster angle microscopy (BAM)

BAM is a technique that allows for visualization of the morphology of film at the air/water interface and is based on the difference between the refractive indices of the subphase (water) and the spread film.[110] The Brewster angle, θ_B, of a substance is defined as the incident angle at which p-polarized light is completely refracted i.e. no light is reflected. The relationship between refractive incidences, n, and Brewster angle of the air-water interface is

$$\tan \theta_B = \frac{n_{water}}{n_{air}} = 53.15° \qquad \textbf{Equation 12}$$

In the absence of a film, no reflected light is detected as the p-polarized light is set to the Brewster angle of the air-water interface (Figure 2.8). The refractive index of lipids is sufficiently different from that of water that, at the Brewster angle of water, the presence of a coherent lipid film will result in reflection which can subsequently be imaged. Different phases have sufficiently different optical properties that they can be detected. One of the limitations of BAM is that only domains that are within the resolution of the microscope can be visualized. This means that features that are less than 1 μm cannot be visualized with a 532 nm laser and 20X objective.

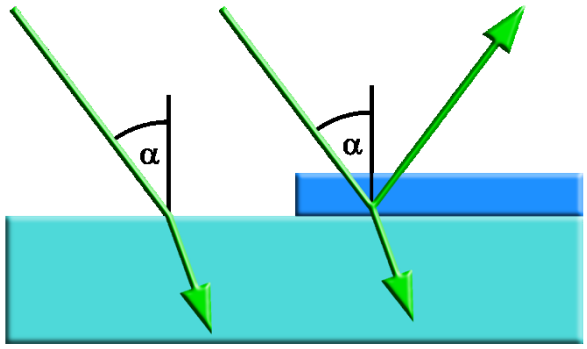

Figure 2.8 Schematic representations of the interaction of p-polarized light at the Brewster angle of an air-water interface in the absence (left) and presence (right) of a lipid film.

2.5. Atomic force microscopy (AFM)

AFM is a high resolution scanning probe microscopy that is used to image thin films that have been transferred to solid supports. The thin film can be transferred from the air/water interface via multiple methods, however, only the Langmuir-Blodgett (LB) deposition method was used.

LB deposition consists of inserting a piece of mica into the subphase prior to spreading the lipid or peptide solution and then, once the desired surface pressure is reached, slowing withdrawing the solid support (Figure 2.9a) while maintaining the film at constant surface pressure.[111] The film adheres to the surface and can subsequently be imaged. With AFM, a cantilever scans across the surface of the sample in tapping mode due to the soft nature of the film (Figure 2.9b). In tapping mode, the cantilever oscillates while scanning the surface. The force amplitude at which the tip scans is kept low to prevent damage to the film. Changes in the position of the cantilever result in the deflection of the laser beam that has been aligned with the top of the cantilever and subsequently this deflection is transformed into an topological image from which the features of the film e.g. height and domain sizes can be determined.

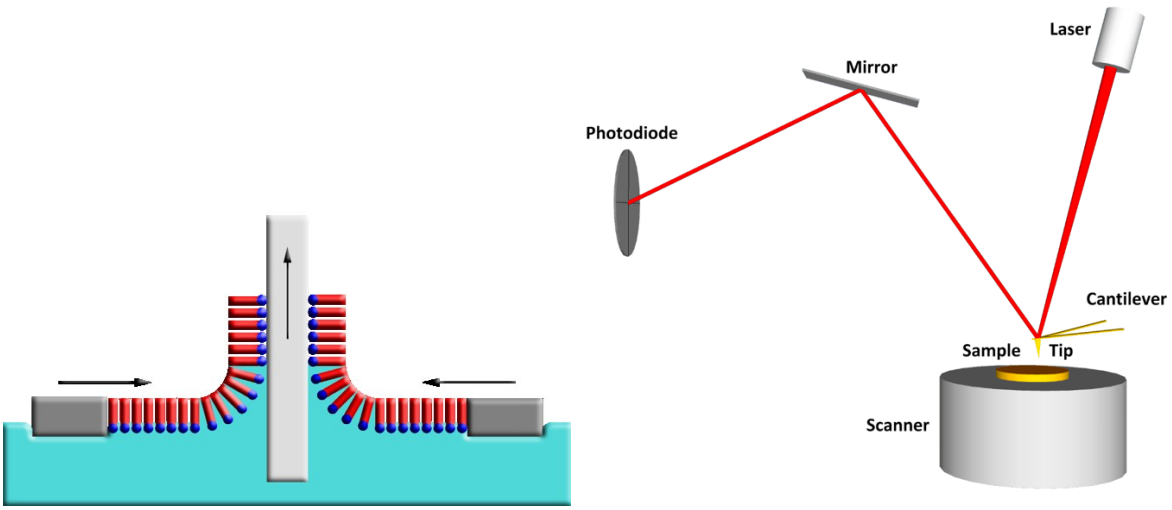

Figure 2.9 Schematic representation of the Langmuir-Blodgett deposition technique (a) and the working principle of an atomic force microscope (b)

Chapter 3. The interfacial self-assembly of antimicrobial peptide GL13K into non-fibral crystalline β-sheets

3.1. Abstract

The need for new and potent antibiotics in an era of increasing multi-drug resistance in bacteria has driven the search for new antimicrobial agents, including the design of synthetic antimicrobial peptides. While a number of β-sheet forming antimicrobial peptides have been proposed, their similarity to β-amyloids raises a number of concerns associated with neurodegenerative states. GL13K is an effective, synthetic antimicrobial peptide that selectively folds into β-sheets at anionic interfaces. Moreover, it is one of relatively few antimicrobial peptides that preferentially folds into β-sheets without bridging disulfides. The interfacial activity of GL13K has not been investigated nor its propensity to form amyloidic fibrils. Using structural studies at the air-water interface and in the absence of anionic lipids, we demonstrate that while GL13K does form crystalline β-sheets, it does not self-assemble into fibrils. This work emphasizes the requirement for a single charged amino acid in the hydrophobic face to prevent fibril formation in synthetic peptides.

3.2. Introduction

Antibiotic resistance in bacteria has driven the search for new antimicrobial agents, including the design of synthetic antimicrobial peptides whose functionality can be optimized to improve their bactericidal capabilities. While the majority of antimicrobial peptides (AMPs) preferentially fold into amphipathic α-helices and subsequently induce membrane disruption and cell death, there is a smaller subsection of AMPs that fold preferentially into β-sheets e.g. arenicin-1, protegrin-1, tachyplesin, gramicidin S, defensin, and labaditin. [14–16,19–21] For the most part, these AMPs depend on disulfides to maintain their secondary structures and bactericidal activities.[22–24]

GL13K is a synthetic thirteen-residue, cationic antimicrobial peptide that effectively kills both Gram-positive and Gram-negative bacteria.[112–114] It has a net positive charge of +5 at physiological pH, and biophysical characterization showed that the peptide preferential folds into β-sheets in the presence of anionic bilayers but remains unstructured in buffer and in the presence of zwitterionic membranes.[50] NMR studies showed that GL13K has a propensity to fold

into α-helices in zwitterionic micelles but confirmed the preferential folding into β-sheets in anionic bicelles.[115]

β-sheet forming amyloids have been linked to numerous neurodegenerative diseases including Parkinson's disease, Alzheimer's disease, spongiform encephalopathies (mad cow disease), and type II diabetes.[25] While there is no distinct sequence similarities between amyloid β (Aβ) peptides, prion proteins (PrP) and islet amyloid polypeptide (IAPP), all three form the characteristic cross-β structure.[29] It has been proposed that there is a functional link between antimicrobial peptides and amyloids in that they both disrupt cell membranes and induce cell death.[26] Despite their different sequences and properties, some AMPs have been shown to cross-β structures, for example protegrin-1 was found to undergo amyloidosis and form fibrils with much faster kinetics than Aβ 1-42,[35] implying a potential risk in using β-sheet forming AMPs as antimicrobial agents.

To further pursue GL13K as a potential therapeutic, it is essential to understand its interfacial behaviour and to determine whether it is a fibril-forming peptide at physiological pH. Previous studies showed that GL13K formed twisted fibrils when stored in buffers of pH greater than 9 for extended periods[116] and similarly, deprotonation of the amino-terminus has been shown to drive fibril formation in pentapeptides.[117] Using an approach employed for the study of peptides, including amyloid β peptides, NK2, and arenecin,[30,118–120] we have investigated GL13K organization at the air/water interface to ascertain whether the GL13K folds at the air/water interface in the absence of a membrane, and if so, whether it preferentially folds into β-sheets and whether these sheets are aggregated into fibrils.

3.3. Materials and Methods

3.3.1. Materials

Sodium phosphate monobasic monohydrate ($NaH_2PO_4 \cdot H_2O$) and sodium phosphate dibasic heptahydrate ($Na_2HPO_4 \cdot 7H_2O$) salts purchased from Sigma Aldrich and Fischer Scientific, respectively were of purity > 98%. All experiments were conducted using 10 mM sodium

phosphate buffer that was adjusted to pH 7.4. GL13K (sequence GKIIKLKASLKLL-NH2) was purchased from BioBasic Inc. (ON, Canada) with a purity of > 95%. No further purification was conducted. Stock peptide solutions of 1-2 mg/mL were prepared by dissolving the peptide in ultrapure water (18.2 MΩ cm^{-1}) obtained from a Barnstead Easypure II purification system. This water was used to prepare all buffer and peptide solutions.

3.3.2. Surface Pressure-Area Isotherms

Surface pressure-area isotherms were obtained using a NIMA Langmuir film balance with a surface area of 80 cm^2. Peptide was spread on the surface of 10 mM sodium phosphate (pH 7.4) buffer and allowed to equilibrate at the interface for thirty minutes prior to compression. The film was compressed at a speed of 5 cm^2/min using mobile barriers. Surface pressure-area isotherms were measured at least 5 times to ensure reproducibility of the peptide film. All experiments were conducted at room temperature.

3.3.3. Grazing Incidence X-ray Diffraction and X-ray Reflectivity

Grazing incidence x-ray diffraction (GIXD) and x-ray reflectivity (XR) experiments were conducted at NSF's ChemMatCARS beamline 15 ID-C at Argonne National Laboratory (Lemonte, IL, USA). Experiments were conducted using a 340 cm^2 NIMA Langmuir film balance and the same experimental procedure was followed with the exception of the compression speed which was increased to 10 cm^2/min given the larger surface area of this trough. The trough was sealed in a chamber and then flushed with water-saturated helium to reduce scattering by oxygen in the air.

The parameters of the x-ray beams were: wavelength 1.239 Å, incidence angle 0.09061°, horizontal and vertical sizes 20 μm and 120 μm, respectively, producing a beam footprint of 20μm by 7.6 cm. The x-rays were diffracted from the air/water interface, and the diffracted intensity was monitored using a 2D Swiss Light source PILATUS 100K detector set to single-photon counting mode. Two sets of slits, one placed in front of the detector and the other placed 280.0 mm from the sample, were used to minimize intense low-angle scattering. Data was patched using software developed by Wei Bu, a beamline scientist at ChemMatCARS. The in-plane Bragg peaks in the GIXD data were fit using Lorentzian functions using OriginLab Graphing and Analysis software. The position and full width at half maximum (FWHM) of these

peaks were used to determine the d-spacing and correlation lengths, respectively, as has been described previously.[107]

For x-ray reflectivity measurements,[121,122] the reflectivity intensities at Q_z angles ranging between 0.01 and 0.7 $Å^{-1}$ were measured. These intensities were then normalized by the Fresnel reflectivity and analyzed using a ChemMatCARS software developed by Wei Bu to generate an electron density profile. The slab model was used to fit the normalized reflectivity data and generate an electron density profile. This electron density profile is an average over the footprint of the beam and represents the vertical distribution of electron density in the film. Starting electron densities were estimated based on values in the literature followed by optimization to improve the fit.

3.3.4. Polarization Modulation Infrared Reflection Absorption Spectroscopy

PM-IRRAS experiments were conducted at Université Laval (Québec City, QC, CA) on an instrument that has been described in detail by Bourque *et al.*[123] A home-built Langmuir film balance of surface area 180 cm^2 and 5 mm depth coupled with a NIMA pressure sensor. Infrared light from a Nicolet iS50 Fourier transform IR spectrophotometer (Thermo Scientific, Madison, WI) was reflected off the air/water interface at a grazing angle and measured using a photovoltaic MCT detector (Kolmar Technologies, Newburyport, MA). The polarization of the beam was modulated with a photoelastic modulator PEM-90 (Hinds Instruments, Hillsboro, OR) that was set for optimum efficiency at 1600 cm^{-1}.

Spectra were generated from the co-addition of 1024 scans that were recorded at a scanning mirror velocity of 0.47 cm/s and a resolution of 8 cm^{-1}. Normalized spectra were obtained by plotting the difference of the spectra of the covered and bare subphase divided by the spectra of the bare subphase. The OMNIC software was used to process the spectra and correct the baselines. PM-IRRAS selection rules state that transition dipoles that are parallel with the surface will produce positive bands, whereas transition dipoles that are oriented perpendicular to the interface will yield negative bands.[124] Spectra of α-helices and β-sheets were compared to simulations by Blaudez *et al.* to determine the orientation of peptides at the interfaces.[105]

3.3.5. Atomic Force Microscopy (AFM)

AFM imaging was performed on peptide films transferred onto mica substrate from the air/water interface via the Langmuir-Blodgett (LB) deposition method.[111] By this method, the freshly-cleaved mica is submerged in the subphase prior to spreading the peptide. Once the desired surface pressure has been reached, the substrate was pulled out of the subphase at a speed of 1 mm/min while holding the surface pressure constant. Transfers were conducted at surface pressures of 5, 10, 15, 20, and 30 mN/m, and images were collected in air at room temperature.

A Nanoscope IIIa (Digital Instruments, Santa Barbara, CA) was used in tapping mode with etched silicon cantilevers with a tip radius of <10 nm, frequency of ~300 kHz, nominal spring constant of 20-80 N/m and scan rate of 1 Hz. An oscillation amplitude of 175 mV and medium damping (~25%) were employed.

3.4. Results and Discussion

GL13K is extremely surface active on 10 mM sodium phosphate and forms a very stable monolayer (Figure 3.1). The critical area, the area at which the peptides begin to interact and form a coherent film, corresponds with the dimensions of a fully extended peptide and indicates that the peptides lie flat at the interface prior to compression. Brewster angle microscopy has been used to visualize in situ changes in morphology in response to compression of peptide monolayers.[125,126] With GL13K, the emergence of a coherent film at higher surface pressures yielded a subtle change in light intensity but no distinct morphological features could be distinguished (data not shown). Thus, if peptide aggregates are present, they must be below the resolution of BAM (< 1 μm).

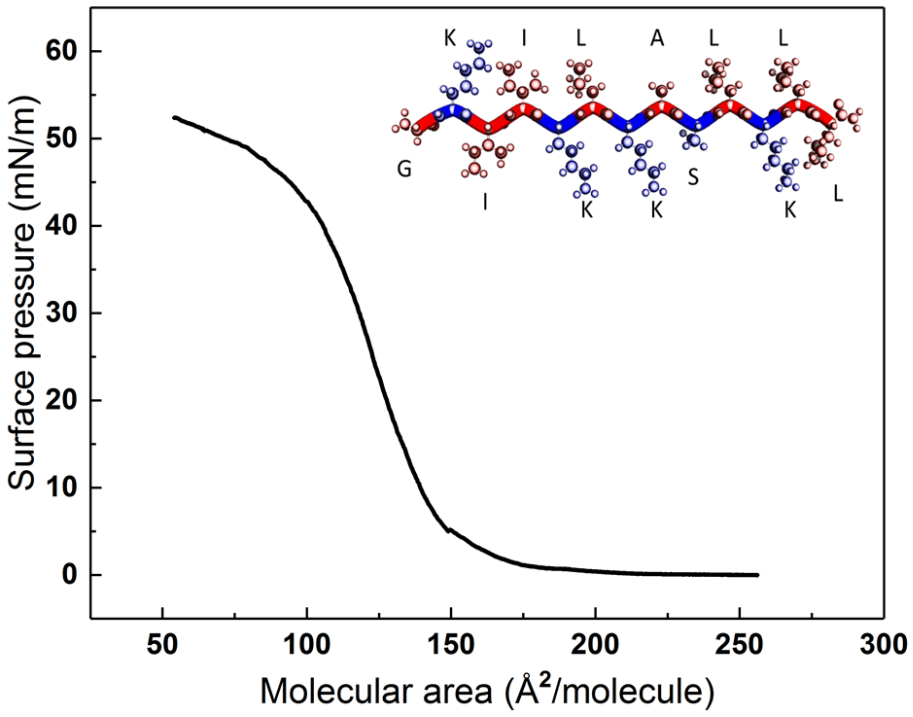

Figure 3.1 Schematic representation of the sequence of GL13K (inset, hydrophilic and charged residues are blue) and surface pressure-area isotherm of GL13K on a 10 mM sodium phosphate buffer, pH 7.4 subphase

Vertical electron density profiles and lateral organization were derived from x-ray scattering methods. The electron density profiles (Figure 3.2a) were generated using a two-slab model by fitting the normalized x-ray reflectivity data (Supplemental Materials, Table 3.1). The second slab was added to improve the quality of the fit and account for the contribution of adsorbed ions and structured water.[109] It was not possible to fit the data to a simple one-slab model. There does not appear to be a significant vertical reorganization at the air/water interface as the GL13K film is compressed. The electron density profiles imply that there is a single layer of peptide at the interface with a diffuse layer of ions directly underneath. The latter likely results from the high charge density of the peptide. The electron density and roughness of the second layer decrease with increasing surface pressure indicating that the ion layer becomes less diffuse attributed to a higher surface charge density as the peptides become closer-packed.

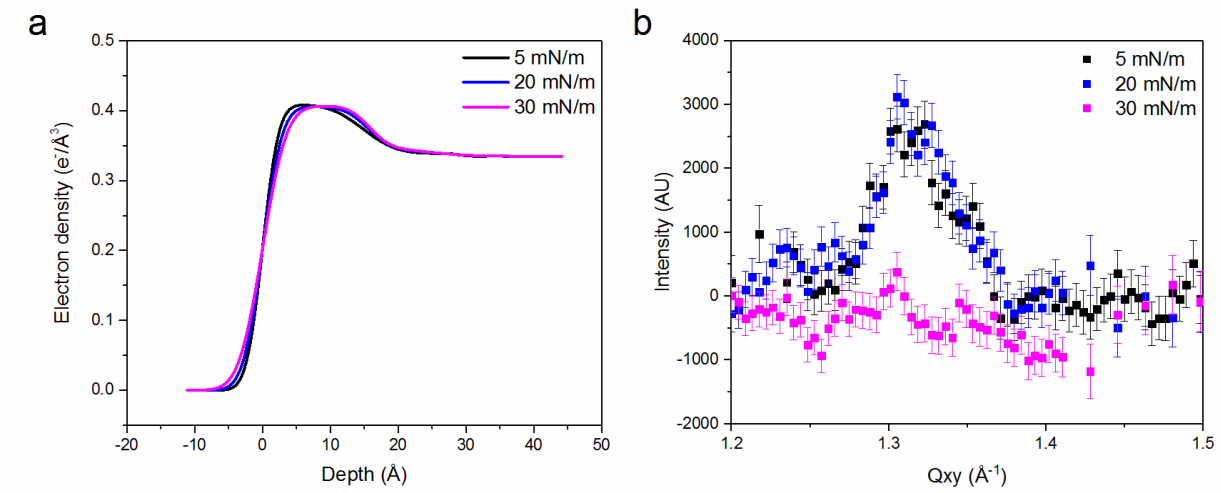

Figure 3.2 Fitted electron density profiles (a) and Bragg peak profiles as a function of the in-plane scattering vector component Q_{xy} (b) for GL13K at the air/water interface at 5, 20 and 30 mN/m

While x-ray reflectivity provides information about vertical organization at the interface, GIXD provides information about lateral organization. Peptides that organize into crystalline β-sheets have been shown to exhibit a peak at Q_{xy} ~1.3 and 0.1-0.2 $Å^{-1}$, corresponding to the inter-strand spacing due to hydrogen bonding and the repeat distance (end-to-end) between the peptides along the backbone axis, respectively.[118,127–129]

The GIXD intensity (integrated over Q_z) as a function of Q_{xy} for GL13K is shown in Figure 3.2b. A Bragg peak is observed at the Q_{xy} position 1.32 $Å^{-1}$, but no peak was observed at lower Q_{xy}. This shows that the peptide organizes into crystalline β-sheets at surface pressures as low as 5 mN/m, but this crystallinity is one-directional given the absence of the low Q_{xy} peak. The crystallinity at 5 and 20 mN/m, given by the correlation length (Supplemental Materials, Table 3.2), is similar to that observed for Aβ40 but significantly weaker than that of the short, 12-residue amyloid-like peptide LSFD for which a coherence length greater than 500 Å was observed.[130] As the film is compressed to small surface areas, the crystallinity of the peptide peak weakens from a length corresponding to ~ 6 peptides to the point of being negligible at a

surface pressure of 30 mN/m. In all cases, the peaks remain at or near $Q_z = 0$ Å^{-1}, showing that the β-sheets are not significantly bending or twisting at the interface.[127]

To ensure that the method of formation of the film does not alter the peptide organization, GIXD measurements were performed and compared for spread monolayers and adsorbed monolayers, the latter from both dilute solution and after injection of a concentrated stock into the subphase. All three methodologies yield the same Bragg peak, a lack of Bragg peaks at low Q_{xy} and similar electron density profiles (Supplemental Materials, Tables 3.1 and 3.2).

While GIXD demonstrates a loss of β-sheet crystallinity, it does not indicate the overall secondary structure of the peptide at the interface. PM-IRRAS provides information about ordered secondary structures as well as their orientation at the air/water interface.[105] Figure 3.3 shows the PM-IRRA spectra for GL13K spread at the interface. At all surface pressures, the amide I band position is ~1620 cm^{-1}. Typically, amide I bands of β-sheets are at positions closer to 1630 cm^{-1}, however, the band position can shift as low as 1619 cm^{-1} with increasing number of strands.[101] This supports the GIXD results indicating that GL13K forms an extended β-sheet network, not just single β-strands. A weak second amide I band at 1696 cm^{-1} and the amide II band at 1538 cm^{-1} are also assigned to β-sheet formation. The ratio of the intensities of the main amide I and amide II bands can be used to determine the orientation of the peptide. By comparison to simulated data for interfacial β-sheets,[105] it can be seen that the peptide does not lie completely flat at the interface and becomes more tilted with compression. The angle of the long axis of the peptide relative to normal of the interface (denoted as θ by Blaudez *et al.*) is ~90° i.e. parallel with the interface, however the angle of the carbonyls relative to the interface (Ψ) is between 0 and 45°. Compression of the film causes the axes of the peptide to become more tilted, i.e. θ to become smaller and Ψ to become 45°. At 20 mN/m, θ is ~70°, and at 30 and 40 mN/m, θ is ~50°. This increase in tilt would explain the slight increase in thickness of the peptide monolayer observed by x-ray reflectivity (Supplemental Materials, Table 3.1).

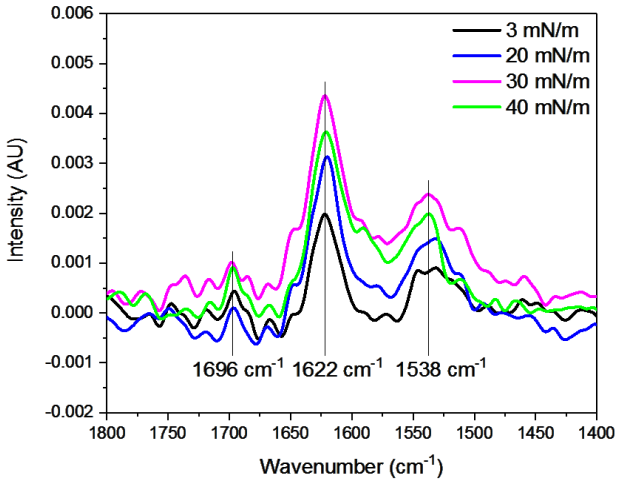

Figure 3.3 PM-IRRAS spectra overlay at GL13K surface pressures 5, 20, 30, and 40 mN/m

To determine if fibrils were forming at the interface, despite the low crystallinity, AFM was conducted on transferred peptide films (Figure 3.4). At surface pressures of 15 mN/m and below, small amorphous agglomerations (bright spots) can be observed (Figure 3.4a). These resemble the structures observed by Ye *et al.* after GL13K was incubated for 8 days at pH 9.4.[116] At higher surface pressures, the number of small agglomerations decreases. In contrast, Shin *et al.* observed an increase in amorphous agglomerations with increasing surface pressure for films of synthetic polypeptides, which they attributed to surface micelle structures[131] that appear to form due to the block copolymer nature of their peptide. In addition to agglomerations, small domains that are about 1 nm above the background can also be observed. These domains appear more prominently in the transfers conducted at 20 mN/m and grow with further compression (Figure 3.4b, 3.4c). Although the domains can grow to sizes nominally greater than the lateral resolution of BAM, these were not observed due to the high density of smaller domains in the surrounding matrix, such that there is insufficient contrast in the optical properties between the phases. The height difference between the domain and the background matrix suggests a co-existence between ordered β-sheets and random coil peptides. Although the thickness of the β-sheet regions is comparable to that observed for the amyloid-like peptide LSFD deposited onto solid substrate, there is no evidence of the regular, close-packed fibrils observed for this peptide.[126]

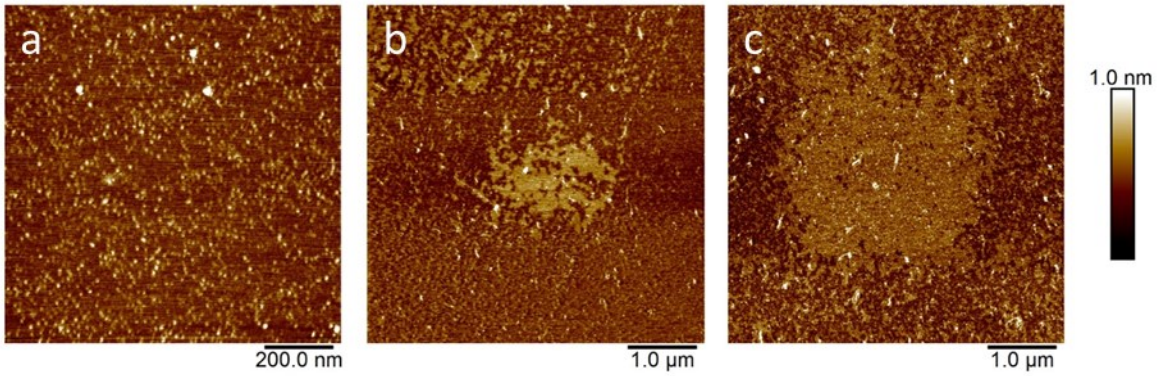

Figure 3.4 AFM images of GL13K deposited on mica at 15 (a), 20 (b), and 30 mN/m (c)

This surface organization of GL13K is in agreement with both experimental and computational findings that the propensity to form β-sheets does not necessarily imply fibril formation.[33,34] Computational studies with eight-residue peptides of varying sequences found a hydrophobic-polar-hydrophobic (HPH) sequence motif was important for the formation of β-sheets.[34] Amyloid fibril formation, which is driven by specific coulombic interactions and hydrophobic interactions, is dependent on a nucleation seed,[30–32]. For example, the side-chains often form an interdigitated steric zipper motif[29] for which a Ile > Leu mutation has been shown to prevent fibril formation by disruption of the close-contact face of the peptides.[33]

Multiple variables have been suggested as contributors to amyloidosis. Increasing the net positive charge of the peptide has been shown to lower peptide self-association even when the hydrophobic face of amphipathic peptides is unaltered as this produces a peptide that has a lower net hydrophobicity.[132] Peptide length may also contribute since biomimetic β^{3R3}-peptides ranging from 8 to 17 β-amino acids exhibited a loss of crystallinity and inter-peptide networking with increased length.[129] It has also been suggested that the presence of a lysine on the non-polar face modulates peptide self-association.[132] All of these factors apply to GL13K and explain why it does not form fibrils. On the other hand, while protegrin-1 has a net charge of +7, and has arginine residues on its hydrophobic face (PDB 1PG1), it does form fibrils. Notably, protegrin-1 adopts an internal β-hairpin conformation held by two disulfide bridges, thus despite its longer sequence it actually forms a shorter β-sheets.

3.5. Conclusions

GL13K is an antimicrobial peptide that assembles preferentially into antiparallel β-sheets. At high surface pressures, the peptides continue to exhibit β-sheet behaviour but lose crystallinity and do not form fibrils. This loss in crystallinity appears to be driven by a compression-induced increase in peptide tilt. Fibril formation is also likely prevented by GL13K's net charge of +5 and the lysine on its hydrophobic face. Since GL13K has been reported to form fibrils at high pH, presumably the pH is required to deprotonate the lysine that lies on the hydrophobic face, which should have a lower pKa than the amino-terminus, thus driving the hydrophobic interactions required for fibril formation. For therapeutic applications, this residue must remain protonated to prevent amyloidic behaviour.

3.6. Supplementary Material

3.6.1. Adsorbed peptide film formation

The surface behaviour of GL13K in adsorbed films was investigated and compared to the spread film reported. These films were prepared using two methods: injection of peptide from a concentrated stock solution and pre-dissolution of peptide into a large volume subphase (from the same concentrated peptide stock). The main differences between these two approaches are the peptide concentration and the adsorption kinetics. In the former, the final concentration of peptide is 10 μM and the rate of surface saturation is rapid (under five minutes), while in the latter the peptide concentration is 200 nM and the peptide is allowed to adsorb over a twelve hour period.

Given the large amount of peptide required for the injection experiment, experiments were conducted using a Teflon trough insert of dimensions 6.6 cm x 6.6 cm x 0.35 cm and volume of 20 mL (GIXD and XR). The overnight incubation of the peptide subphase and subsequent compression measurements were conducted on the same trough following the same protocol as the spread peptide films. All experiments were conducted using the same 10 mM sodium phosphate buffer adjusted to pH 7.4. The results of these experiments have been included below.

3.6.2. GIXD and XR fits

System	Surface Pressure (mN/m)	Slab 1			Slab 2			χ^2
		Thickness (Å)	ρ (e/Å^3)	σ (Å)	Thickness (Å)	ρ (e/Å^3)	σ (Å)	
GL13K spread	5	14.8	0.409	1.9	14.2	0.339	3.8	16
	20	15.6	0.406	2.3	10.8	0.343	2.8	18
	30	15.7	0.407	2.8	8.3	0.348	2.4	18
GL13K adsorption 0.2 μM	5	15.5	0.369	2.9	11.5	0.349	1.0	28
	20	16.1	0.400	2.5	7.8	0.350	1.8	17
	30	16.5	0.401	2.9	8.8	0.347	1.9	13
GL13K injected 10 μM	16	14.9	0.419	2.5	10.6	0.346	2.9	27

Table 3.1 Fitting parameters for x-ray reflectivity data of all peptide systems, d is the thickness of the slab, ρ is the electron density, and σ is the roughness of the slab. Slabs are numbered from air to subphase, and the electron density of the buffer subphase was 0.335 $e^-/Å^3$

System	Pressure (mN/m)	Qxy ($Å^{-1}$)	FWHM	d-spacing (Å)	Correlation length (Å)
GL13K spread	5	1.32	0.0918	4.78	62
	20	1.32	0.0636	4.77	89
	30	-	-	-	-
GL13K absorption 0.2 μM	5	1.32	0.0118	4.76	-
	20	1.32	0.0429	4.77	132
	30	1.32	0.0558	4.78	101
GL13K injected 10 μM	16	1.32	0.0490	4.77	115

Table 3.2 Fitted GIXD Bragg peak positions, fitting information for all peptide peaks

The GIXD peaks were fit as Lorentzian peaks, and the d-spacing and correlation lengths were calculated using the values of Qxy and FWHM, respectively. The correlation length for the adsorbed GL13K was not included at 5 mN/m because, while the peak was present, it was too weak, so the value calculated was not representative of the actual correlation length.

Chapter 4. Membrane fluidity governs the insertion of the antimicrobial peptide GL13K

4.1. Abstract

Antimicrobial peptides have emerged as potential antibiotics due to their ability to specifically target and disrupt bacterial cells. Membrane compositional differences, in particular the preponderance of anionic lipids in bacterial membranes, is now a well-established basis of their selectivity. However, an additional difference between eukaryotic and bacterial membranes is their cholesterol content, where cholesterol is a known modifier of membrane rigidity. In this work, we probe the impact of membrane fluidity on the interfacial insertion and assembly of the antimicrobial peptide GL13K using monolayer model membranes comprising mixtures of the anionic lipid 1,2-dioleoylphosphatidylglycerol (DOPG) mixed with either cholesterol or 1,2-diphytanoylphosphatidylglycerol (DPhPG). Both cholesterol and DPhPG decrease the permeability of membranes, but, while cholesterol increases membrane viscosity, DPhPG membranes are known to remain fluid. Surface spectroscopy and x-ray scattering techniques show that while the mixture with DPhPG modulated the interaction of GL13K, the presence of cholesterol prevented peptide insertion into the lipid acyl chains. The resulting localization of GL13K in the headgroup region of the membrane drives the formation of more crystalline β-sheets than in the fluid DOPG or DOPG:DPhPG membranes. This work highlights the role of cholesterol, and more importantly the role of membrane fluidity in preventing eukaryotic membrane disruption by antimicrobial peptides and in contributing to the membrane selectivity of this class of antimicrobials.

4.2. Introduction

Abuse of antibiotic administration has resulted in multidrug resistant bacteria. One of the promising fields of study for alternative treatment of bacterial infections is antimicrobial peptides. Natural antimicrobial peptides are an integral component of innate immunity and are effective against a wide range of pathogens.[7] Many synthetic peptides have been designed with modifications to enhance peptide effectiveness, e.g. the addition lysine or arginine residues.[133] GL13K (GKIIKLKASLKLL-NH2) is a thirteen residue antimicrobial peptide whose sequence has been derived from the sequence in the human parotid secretory protein (hPSP) which is

responsible for the protein's lipopolysaccharide (LPS)-binding capabilities.[47,112] While the native sequence has been shown to be bacteria-agglutinating, GL13K is effective against Gram-positive and Gram-negative bacteria, and preventative of biofilm formation and growth while being neither hemolytic nor cytotoxic.[112]

Model membrane studies have been used to develop a better understanding of peptide selectivity for bacterial membranes as compared to eukaryotic membranes.[7] One of the main differences between bacterial and eukaryotic membranes is the charge of the outer membrane. While the proportions of negatively-charged phosphatidyl glycerol (PG) and phosphatidylethanolamine (PE) headgroups vary between Gram-positive and Gram-negative bacteria, bacterial plasma membranes consist predominately of anionic lipids.[7,51,52] Eukaryotic membranes, on the other hand, are predominately zwitterionic. The main components are phosphatidylcholine (PC), phosphatidylethanolamine (PE), phosphatidylserine (PS), phosphatidylinositol (PI) and phosphatidic acid (PA).[53] Additionally, the cell wall of Gram-positive bacteria and the outer membrane of Gram-negative bacteria are both anionic due to the presence of lipoteichoic acid (LTA) and lipopolysaccharide (LPS), respectively.[51]

Circular dichroism (CD) studies of GL13K with model membranes indicated that it is highly selective for anionic dioleoylphosphatidylglycerol (DOPG) membranes compared to zwitterionic dioleoylphosphatidylcholine (DOPC) membranes.[50] While the peptide exhibited random coil conformation in the presence of DOPC liposomes, it folded into β-sheets with DOPG membranes. Nuclear magnetic resonance (NMR) studies showed that GL13K did indeed interact with zwitterionic membranes at concentrations too low to be detected in solution by optical spectroscopy.[115] Solid-state NMR studies with ^{2}H- and ^{15}N-labelled peptides showed that GL13K folds into helices in zwitterionic bicelles while it folds into β-sheets with as little as 25 mol% DOPG.[115] They determined that the peptide strongly disturbed the lipid bilayer and hypothesized that this is due to peptide association and a high peptide density in the membrane.

The second difference is cholesterol (Ch) content. The concentration of cholesterol in eukaryotic membranes varies between 20 and 40%,[55,56] and it contributes significantly to the membrane rigidity and packing density and is associated with the formation of lipid rafts.[54] Cholesterol fluidizes liquid-ordered membranes by disrupting long-range (global) order and condenses the acyl chains of liquid-expanded (fluid) membranes via short-range (local) ordering.[56,60,67,69,70] The

subsequent increase in lipid chain packing density of fluid membranes can increase membrane viscosity by approximately 16% in DOPC:Ch 60:40 membranes.[71] Some studies have shown that the presence of cholesterol hinders insertion of peptides into lipid bilayers,[57–59] but whether this is due to charge dilution or increased viscosity has yet to be fully resolved. Previous GL13K studies showed significant liposome aggregation when GL13K interacts with DOPG:Ch 60/40 bilayers but no interaction was observed in the DOPC:Ch control.[49]

As monolayers mimic the outer leaflet of the phospholipid bilayer, they have been widely used to determine the nature and kinetics of interaction of peptides and proteins with lipid interfaces.[103,134,135] Numerous interfacial spectroscopic and diffraction techniques have been developed to characterize these peptide/lipid interactions at the air/water interface. In this work, the secondary structure and orientation of the peptides at the monolayer were determined with polarization modulation infrared absorption spectroscopy (PM-IRRAS), which couples Fourier transform IR reflection spectroscopy with rapid polarization modulation.[136] Information about lipid ordering and the formation of crystalline structures was obtained using grazing incidence x-ray diffraction (GIXD)[134] while X-ray specular reflectivity (XR) was used to determine monolayer thickness and the electron density distribution at the air-water interface, i.e. if the peptide sits between the lipid head groups or if it is deeper in the monolayer and is in the tail and head group region.[137]

While cholesterol may not be present in bacterial membranes, branched lipids, particularly iso- and anteiso-branched lipids, are found in abundance.[72] Diphytanoylphospholipids are chemically stable synthetic archael lipids that forms membranes of similar thickness as those formed by dioleoyl analogues.[73,74] They remain highly fluid with disordered chains despite the increased packing density of the acyl chains due to the eight additional methyl groups per phospholipid.[77,78] Membranes composed of diphytanoylphosphatidylcholine contain fewer packing defects than membranes containing an oleoyl acyl chain, e.g. POPC,[79] due to this increased chain packing density. Mixtures of DOPG and either cholesterol or DPhPG were used to alter the membrane permeability and/or fluidity and to probe the impact of these factors on the membrane insertion of GL13K.

4.3. Materials and Methods

4.3.1. Materials

1,2-dioleoyl-sn-glycero-3-phospho-(1'-rac-glycerol) (DOPG) and 1,2-diphytanoyl-sn-glycero-3-phospho-(1'-rac-glycerol) (DPhPG) were purchased from Avanti Polar Lipids Inc. in powder form at 99% purity. Cholesterol and HPLC-grade chloroform were purchased from Sigma Aldrich. Sodium phosphate monobasic monohydrate ($NaH_2PO_4 \cdot H_2O$) and sodium phosphate dibasic heptahydrate ($Na_2HPO_4 \cdot 7H_2O$) salts were purchased from Sigma Aldrich and Fischer Scientific, respectively, at purity >98%. GL13K (sequence GKIIKLKASLKLL-NH2) was synthesized at the University of Minnesota peptide synthesis facility at > 95% purity and generously provided by S.-U. Gorr. Stock lipid solutions were prepared in chloroform at concentrations ranging from 1-5 mg/mL, and spreading solutions were prepared at concentrations of 0.4-0.6 mg/mL. All lipid mixture compositions are reported in mol%. Stock peptide solutions of 1-2 mg/mL were prepared by dissolving the peptide in ultrapure water (18.2 MΩ cm^{-1}) obtained from a Barnstead Easypure II purification system. This water was used to prepare all buffer and peptide solutions. All experiments were conducted using 10 mM sodium phosphate buffer that was adjusted to pH 7.4.

4.3.2. Surface Pressure-Areas Isotherms

Surface pressure-area isotherms were measured using a NIMA Langmuir film balance with a surface area of 80 cm^2. Lipids were spread from chloroform solutions at amounts such that they remained in the gaseous phase and were compressed at a speed of 5 cm^2/min using mobile barriers after a wait period of 10 minutes. All experiments were conducted on 10 mM sodium phosphate at room temperature.

4.3.3. Experiment Design

Given the large quantity of peptide required to prepare 10 μM peptide solutions, experiments were conducted using an insert of dimensions 6.6 cm x 6.6 cm x 0.35 cm and a volume of 20 mL (GIXD and XR) and an insert of dimensions 4 cm x 4.5 cm x 0.3 cm and a volume 6 mL (PM-IRRAS).

Lipids were spread dropwise onto the air/water interface until a biologically-relevant surface pressure (~30 mN/m)[99] was reached. Once the surface pressure of the film stabilized, measurements of the lipid alone were conducted followed by peptide injection into the sodium phosphate subphase for a final peptide concentration of 10 μM. The kinetic insertion profile of the peptide was monitored using changes in the surface tension.

4.3.4. Surface-specific X-ray Characterization Techniques

Grazing incidence x-ray diffraction (GIXD) and x-ray reflectivity (XR) experiments were conducted at NSF's ChemMatCARS beamline 15 ID-C at Argonne National Laboratory (Lemonte, IL, USA). Experiments were conducted using a 6.6 cm x 6.6 cm x 0.35 cm trough insert which was sealed in a chamber flushed with water-saturated helium. The parameters of the x-ray beams were: wavelength 1.239 Å, incidence angle 0.09061°, horizontal and vertical sizes 16 μm and 120 μm, respectively. The x-rays were diffracted from the air/water interface, and the diffracted intensity was monitored using a 2D Swiss Light source PILATUS 100K detector set to single-photon counting mode. Two sets of slits, one placed in front of the detector and the other placed 280.0 mm from the sample, were used to minimize intense low-angle scattering. Data was patched using software developed by Wei Bu, a beamline scientist at ChemMatCARS. The in-plane Bragg peaks in the GIXD data were fit using Lorentzian functions using OriginLab Graphing and Analysis software. The position and full width at half maximum (FWHM) of these peaks were used to determine the d-spacing and correlation lengths, respectively, as has been described previously.[107]

For x-ray reflectivity measurements,[121,122] the reflectivity intensities at Q_z angles ranging between 0.01 and 0.7 $Å^{-1}$ were measured. These intensities were then normalized by the Fresnel reflectivity and analyzed using ChemMatCARS software developed by Wei Bu to generate an electron density profile. The slab model was used to fit the normalized reflectivity data and generate an electron density profile. This electron density profile is an average over the footprint of the beam and represents the vertical distribution of electron density in the film. Starting electron densities were estimated based on values in the literature followed by optimization to improve the fit.

4.3.5. Polarization Modulation Infrared Reflection Absorption Spectroscopy

PM-IRRAS experiments were conducted at Université Laval (Québec City, QC, CA) on an instrument that has been described in detail in Bourque *et al*.[123] A trough insert of dimensions 4 cm x 4.5 cm x 0.3 cm was coupled with a NIMA pressure sensor. Infrared light from a Nicolet iS50 Fourier transform IR spectrophotometer (Thermo Scientific, Madison, WI) was reflected off the air/water interface at a grazing angle and measured using a photovoltaic MCT detector (Kolmar Technologies, Newburyport, MA). The polarization of the beam was modulated with a photoelastic modulator PEM-90 (Hinds Instruments, Hillsboro, OR) that was set for optimum efficiency at 1600 cm^{-1}.

Spectra were generated from the co-addition of 1024 scans that were recorded at a scanning mirror velocity of 0.47 cm/s and resolution of 8 cm^{-1}. Normalized spectra were obtained by plotting the difference of the spectra of the covered and bare subphase divided by the spectra of the bare subphase. All spectra are presented as difference spectra such that the lipid spectra have been subtracted and the bands represent contributions from the peptide. The OMNIC software was used to process the spectra and correct the baselines. PM-IRRAS selection rules state that transition dipoles that are parallel with the surface produce positive bands, whereas transition dipoles that are oriented perpendicular to the interface yield negative bands.[124] Spectra were compared to the simulated spectra published by Blaudez *et al*. [105] for β-sheet forming peptides. They defined two angles for β-sheets at interfaces: the angle of the axis of the peptide relative to normal of the interface (θ) and the angle of the backbone carbonyls relative to the interface (Ψ). Variation in these angles leads to intensity changes in both the amide I and amide II bands, thus the interfacial orientation of the peptide (defined by these angles) can be correlated to the intensity ratio (amide I:amide II).

4.4. Results and Discussion

Four model membranes were studied to represent a highly charged anionic membrane surface (DOPG), minimum and maximum proportions of cholesterol in eukaryotic cells (80:20 DOPG:Ch and 60:40 DOPG:Ch, respectively), and a comparable maximal proportion of phytanol lipid (60:40 DOPG:DPhPG). Surface pressure-area isotherms in the absence of peptide (Figure 4.1) show that all four films remain liquid expanded throughout the isotherm and exhibit

film collapse at similar surface pressures. The isotherms of the DOPG:Ch films are at much lower molecular areas than those of DOPG and DOPG:DPhPG films due to the smaller size of cholesterol indicative of the denser packing in these films. From the isotherms the compressibility modulus (C_s^{-1}) can be calculated as the inverse of the compressibility C_s[138] defined as

$$\boldsymbol{C_s = -\frac{1}{A}\left(\frac{\partial A}{\partial \Pi}\right)_T} \qquad \textbf{Equation 13}$$

The compressibility moduli for each of the DOPG, DPhPG, and mixed lipid (DOPG:DPhPG and DOPG:Ch) monolayers are all below 75 mN/m indicating the formation of a fluid, liquid-expanded phase[139,140] (data not shown).

Brewster angle microscopy (BAM)[125,126] is an *in situ* visualization technique that was used to confirm that the components are miscible at the biologically relevant surface pressure of 30 mN/m[99] (data not shown). No distinct morphological features were observed with any of the mixed lipid films, indicating that either the domains were below the 1 μm resolution of BAM or the cholesterol was miscible and the films were homogenous. Bag *et al.* studied DOPC:Ch systems and determined that at 33 mol%, the proportion of cholesterol was not sufficient to induce a liquid ordered phase.[70]

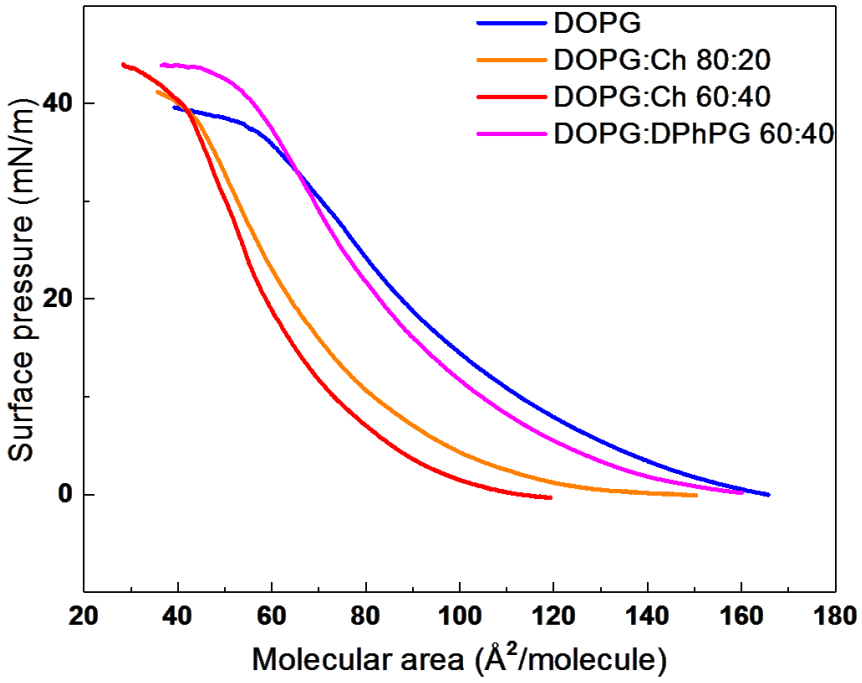

Figure 4.1 Surface pressure-area isotherms of DOPG, DOPG:Ch and DOPG:DPhPG model membranes on a 10 mM sodium phosphate buffer, pH 7.4 subphase

Peptide insertion was characterized using XR, GIXD, and PM-IRRAS. The normalized reflectivity data for each of the films before and after peptide insertion were fit (Table 4.1, Supplementary information Figure 4.5) to generate vertical electron density profiles (Figure 4.2). These electron density profiles show that the electron distribution of all of the model membranes in the absence of peptide are similar. All the films have a distinct acyl chain region (slab 1), headgroup region (slab 2), and an ordered water/ adsorbed counterion region (slab 3). Cholesterol causes a slight elongation of the acyl chain region of the monolayer (slab 1) and a lengthening of the headgroup region. It also lowers the electron density of the headgroup region while increasing the electron density of the chains. This is most noticeable with DOPG:Ch 60:40 (Figure 4.2a).

The impact of GL13K on lipid organization varies significantly between the four films. In the DOPG and DOPG:DPhPG films, there is a substantial shift in the electron density as the electron density of the chain region increases and that of the headgroup decreases (Figure 4.2b and Table

4.1). This implies that GL13K is inserting sufficiently to disrupt the organization of both regions and subsequently reduce the distinct difference in the electron density between the two slabs. Such behaviour was observed with the POPG monolayer in the presence of the linear, β-sheet forming AMP C/S-Ar-1.[141] In comparison, the DOPG:Ch films undergo relatively minor shifts upon interaction with GL13K. DOPG:Ch 80:20 in the presence of GL13K requires an additional slab to achieve an acceptable fit. Notably, for this 80:20 DOPG:Ch system, the redistribution of the thicknesses and electron densities of the top two slabs imply that the ends of the acyl tails have more conformational freedom and space, whereas the three remaining slabs suggest that there is a significant amount of peptide present and the peptides may be structured in multilayers, similar to what was proposed by Neville *et al*. with protegrin.[142] This peptide multilayer appears to be present but less distinct with the DOPG:Ch 60:40 as the thickness of the third slab is comparable to the thickness of the third and fourth slabs of DOPG:Ch 80:20 when GL13K is present. Thus, the x-ray reflectivity suggests that while GL13K inserts into the tail region in DOPG and DOPG:DPhPG 60:40, it is trapped in the headgroup region in DOPG:Ch 80:20 and DOPG:Ch 60:40.

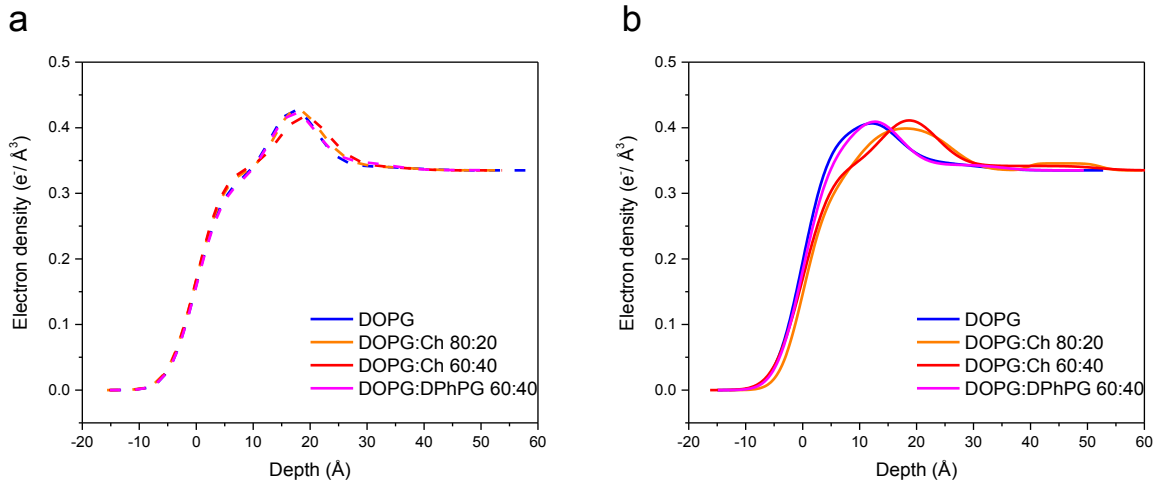

Figure 4.2 Fitted electron density profiles of DOPG, DOPG:Ch 80:20, DOPG:Ch 60:40, and DOPG:DPhPG 60:40 before (a) and after (b) peptide insertion

System	Slab 1			Slab 2			Slab 3			Slab 4			χ^2
	d (Å)	ρ ($e^-/Å^3$)	σ (Å)	d (Å)	ρ ($e^-/Å^3$)	σ (Å)	d (Å)	ρ ($e^-/Å^3$)	σ (Å)	d (Å)	ρ ($e^-/Å^3$)	σ (Å)	
DOPG	14.0	0.320	3.77	5.7	0.500	3.54	18.0	0.341	3.84				15
DOPG +GL13K	10.7	0.391	3.74	4.9	0.439	2.95	14.4	0.348	4.05				15
DOPG:Ch 80:20	14.4	0.335	2.89	5.8	0.491	3.73	18.4	0.340	4.62				26
DOPG:Ch 80:20 + GL13K	8.9	0.290	3.22	17.4	0.402	4.06	13.4	0.335	3.99	12.9	0.346	1.21	11
DOPG:Ch 60:40	15.4	0.337	3.82	6.9	0.461	3.61	14.4	0.342	4.15				26
DOPG:Ch 60:40 + GL13K	14.6	0.339	4.06	8.1	0.446	4.05	29.3	0.342	4.30				10
DOPG:DPhPG 60:40	14.4	0.316	3.79	4.6	0.528	3.74	15.3	0.348	3.84				20
DOPG:DPhPG 60:40 + GL13K	10.8	0.362	3.72	4.7	0.48	4.00	19.6	0.34	4.00				24

Table 4.1 Fitting parameters for x-ray reflectivity data of all lipid systems before and after peptide insertion, d is the thickness of the slab, ρ is the electron density, and sigma is the roughness of the slab. Slabs are numbered from air to subphase, and the electron density of the buffer subphase was 0.335 $e^-/Å^3$

GIXD data show that GL13K forms crystalline β-sheets when interacting with any of the four model membranes (Figure 4.3). No lipid Bragg peaks are observed, indicating that the peptide does not have a measurable condensing effect on the lipid film, even at the highest proportion of cholesterol. The position of the Bragg peaks with respect to the in-plane scattering vector Q_{xy} is identical for all films (Supplemental Information, Table 4.2). Peaks at this position correspond to the inter-strand distance for β-sheets and have been observed for a range of β-sheet forming peptides including amyloid β and arenicin-1.[118,127–129] The correlation length calculated from the FWHM is indicative of the extent of crystallinity, i.e. the larger the correlation length the more crystalline the system. GL13K in the presence of the DOPG:Ch mixed lipid systems formed the most crystalline β-sheets, where the correlation length in upon adsorption to DOPG:Ch 80:20 films was slightly higher. The correlation lengths were almost double of those found for GL13K

interacting with DOPG and DOPG:DPhPG 60:40. The peptide correlation lengths with DOPG and DOPG:DPhPG 60:40 indicate β-sheets of similar crystallinity despite the larger difference in intensity (Figure 4.3). This difference cannot be attributed to the intensity of the beam (which was comparable among the four experiments) and can only be explained by the presence of fewer crystalline β-sheet domains within the footprint of the beam.

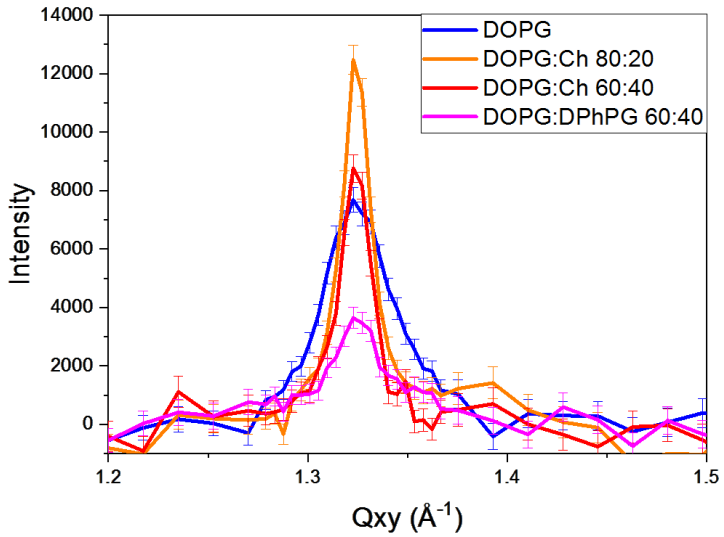

Figure 4.3 Bragg peaks (in-plane scattering vector Qxy) of GL13K inserted into the lipid monolayers at surface pressures ~30 mN/m

All PM-IRRAS spectra in Figure 4.4 show a distinct amide I band at ~1620 cm^{-1} and a band at 1696 cm^{-1} indicating that GL13K is organized into crystalline anti-parallel β-sheets at each of these interfaces. However, the intensities of the amide I and amide II (positioned at ~1530 cm^{-1}) bands vary between the four systems, indicating a different peptide orientation in each of the films. Blaudez *et al.*[105] simulated the spectra for three different values of Ψ: 0° (parallel the interface), 45° or 90° (perpendicular to the interface). For each of these, they varied the angle of the long axis of the peptide relative to normal of the interface (θ) from 0° to 90°. By comparing the intensity ratio of the amide I and amide II bands to that obtained by Blaudez *et al.*, the orientation of GL13K was be approximated. The GL13K carbonyls appear to be parallel with the interface (Ψ = 0°) for all systems. GL13K is most tilted in DOPG (θ ~ 45°), with similar tilts in

the three mixed lipid films: ~ 70° in DOPG:DPhPG 60:40 and DOPG:Ch 80:20, and ~ 80° in DOPG:Ch 60:40.

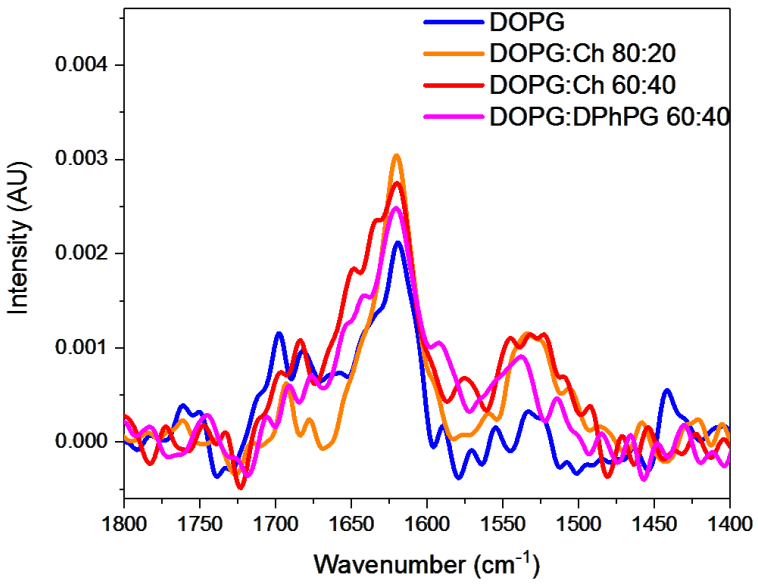

Figure 4.4 PM-IRRAS spectra overlay of GL13K absorbed to the lipid monolayers

While x-ray reflectivity and GIXD data indicate that GL13K inserted similarly into DOPG and DOPG:DPhPG 60:40, the PM-IRRAS spectra show, via the lower peptide tilt angle, that membrane packing induced by the methylene groups of DPhPG does influence peptide insertion. Experimental studies using neutron reflectivity have suggested DPhPC membranes have fewer local defects and a more uniform, space-filling organization of the chains than POPC membranes.[79]

On the other hand, Garten *et al.* hypothesized, based on molecular dynamics simulations, that DPhPG caused larger packing defects than mono- and polyunsaturated lipids, and that these packing defects promoted adsorption of the much larger (140-residue) α-helical protein, α-synuclein[143] Herein, no direct evidence of increased adsorption was observed, however a more extensive study of the adsorption kinetics is required to confirm whether this also occurs with a short β-sheet forming peptide. Valincius *et al.* demonstrated that the bilayer conductance of DOPC:DPhPC 50:50 membranes was greater than DPhPC membranes but less than DOPC

membranes, and theses differences were greater than those between saturated and unsaturated chains.[144] To date, there are relatively few studies on the effect of phytanoyl chains on the kinked chains of oleoyl phospholipids. The organization of GL13K in the presence of DOPG:Ch film is slightly more complex. Cholesterol induces short-range, local ordering in fluid membranes and an increased packing density. This forces localization of the peptide in the headgroup region, in agreement with the tilt angles obtained from the PM-IRRA spectra. Presumably, GL13K is inserted with its charged face toward the headgroup and the hydrophobic face oriented towards the buffer. Hydrophobic interactions would drive the formation of a peptide bilayer, which could contribute to the higher crystallinity of the peptide β-sheets and the larger peptide slab thickness in the x-ray reflectivity. Such a bilayer or even multilayer structure has been proposed for protegrin based on x-ray reflectivity measurements.[142]

4.5. Conclusions

Attenuation of AMPs by cholesterol has been reported for gramicidin, protegrin-1 and LL-37,[57,59,145] suggesting that eukaryotic cells are protected by more than the zwitterionic nature of their outer membranes. However, it was not clear whether this protection was afforded by an increase in membrane viscosity or the lower membrane permeability. Despite the additional space-filling by the methyl groups in the chain region for DPhPG, which is assumed to contribute to the decreased permeability, GL13K readily inserts into DOPG:DPhPG monolayers, as evident form the electron density profile obtained by X-ray reflectivity. However, the methylation of the acyl chains does modulate the tilt angle of the peptide at the interface, presumably due to a reduction in the available space. Cholesterol causes local short-range ordering of the acyl chains, which not only leads to decreased permeability but also increased viscosity. This effect not only alters the angle of GL13K insertion but the peptide no longer inserts into the chain region and is confined to the headgroup region. This forced localization drives the increase in peptide crystallinity (the correlation length doubles). This opens the discussion of the role of β-sheet crystallinity in AMP activity.

4.6. Supplemental Information

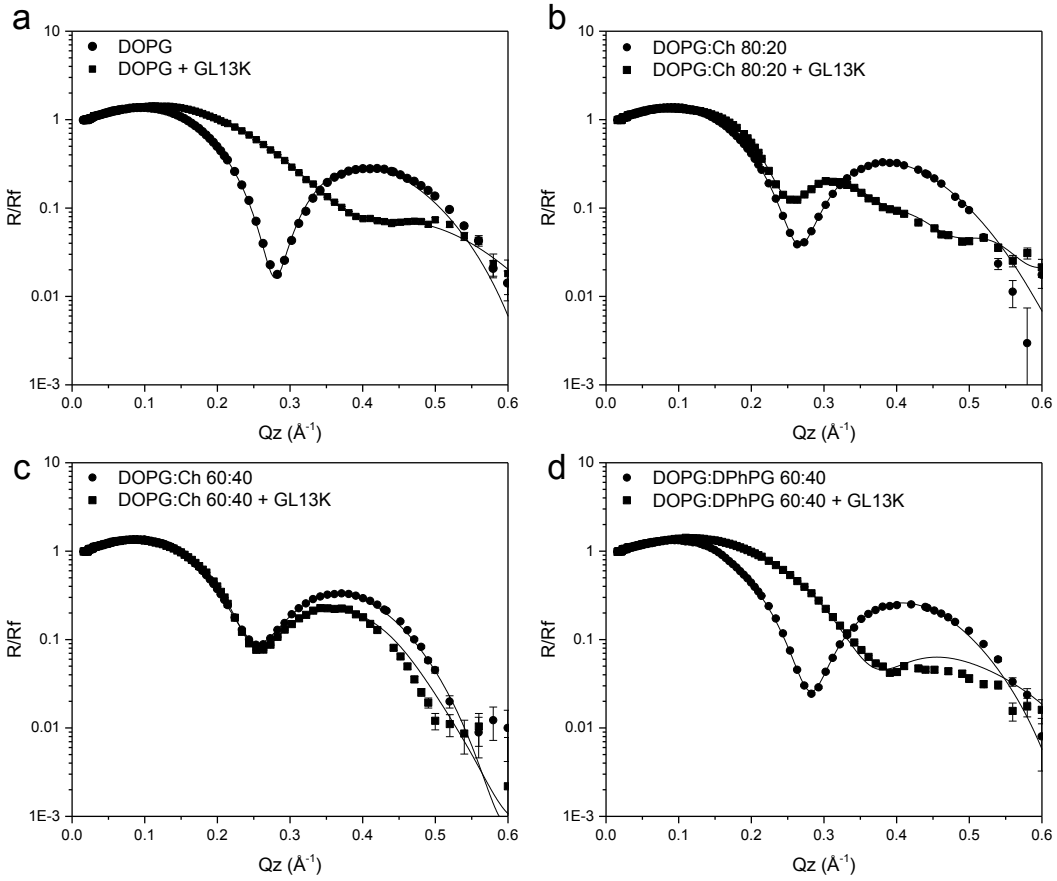

Figure 4.5 X-ray reflectivity data and corresponding fits normalized by Fresnel reflectivity plotted against scattering vector (Qz) of all the lipid films before (circles) and after (squares) peptide insertion for DOPG (a), DOPG:Ch 80:20 (b), DOPG:Ch 60:40 (c), and DOPG:DPhPG 60:40 (d)

System	Qxy ($Å^{-1}$)	FWHM	d-spacing (Å)	Correlation length (Å)
DOPG +GL13K	1.32	0.038	4.76	149
DOPG:Ch 80:20 + GL13K	1.32	0.015	4.76	377
DOPG:Ch 60:40 + GL13K	1.32	0.016	4.76	353
DOPG:DPhPG 60:40 + GL13K	1.32	0.034	4.76	166

Table 4.2 GIXD fitting parameters for the GL13K Bragg peaks

The GIXD peaks were fit as Lorentzian peaks, and the d-spacing and correlation lengths were calculated using the values of Qxy and FWHM, respectively.

Chapter 5. Lysyl headgroup modifications disrupts the organization of antimicrobial peptides bound to the membrane interface

5.1. Abstract

Antimicrobial peptides (AMPs) are thought to target bacteria membranes due to the high proportion of anionic lipids in their membranes. Lysyl-functionalization of the negatively-charged phosphatidylglycerol headgroup in *Staphylococcus aureus* is one of the ways in which bacteria have become resistant to AMPs. Beyond a simple charge-modulation, the molecular mechanisms through which lysylation confers resistance remain largely unknown, in particular for AMPs that are non-pore forming. Using a β-sheet forming AMP, GL13K and lipid monolayer model membranes, we show that the presence of lysyl-functionalized phosphatidylglycerol headgroup modulates but does not prevent the adsorption of the peptide at the membrane interface. The orientation of the lysyl headgroup, which can loop back on itself or extend from the membrane surface, and the corresponding exposure of the cationic charge appear to be critical in defining the interaction with the peptide. We show that in anionic membranes, the GL13K adopts a more crystalline β-sheet at biologically relevant surface pressures while a loss of crystallinity is observed with increasing proportions of lysylphosphoglycerol. These results contribute to an understanding of bacterial resistance mechanisms which can be used to design more effective AMPs.

5.2. Introduction

Antimicrobial peptides are important contributors to the innate immune response of organisms as they kill bacteria by permeabilizing their membranes and also attenuate cytokine production and macrophage differentiation.[84,146,147] In the early years of antimicrobial peptide research, it was speculated that bacteria would not develop resistance to AMPs as this would require extensive modification to their membranes.[84] Unfortunately, it was later discovered that bacteria have developed various mechanisms by which they became less susceptible to AMPs, including upregulation of protease production and modulation and subsequent masking of the negative charge of their membranes via D-alanylation of teichoic acids and the L-lysylation of

phospholipids.[85–87] When resistant strains of *S. aureus* undergo stress, e.g. growth at lower pH or in the presence of AMPs, they upregulate the multiple peptide resistance factor gene (*MprF*) which encodes the enzyme aminoacyl-PG synthase which is responsible for the lysyl-modification of the negatively-charged phosphatidylglycerol headgroups and translocation of the lysyl-phosphatidylglycerol (LPG) to the outer leaflet of the plasma membrane.[88,89] This modification shifts the net charge of LPG to either +1 or to net neutral, depending on the protonation state of the phosphate (pKa ~3), the alpha amine (pKa ~6.5), and the epsilon (terminal) amine (pKa ~10).[91–93] Rehal *et al.* proposed that the epsilon amine loops up to interact with the phosphate of the LPG, a neighboring cardiolipin or DPPG in the membrane.[93]

Most antimicrobial peptides are cationic peptides whose specificity is in part due to the electrostatic interactions that occur between their charges residues (typically lysine or arginine) and the anionic phospholipids of the outer leaflet.[95] The charge screening that occurs when LPG ion-pairs with these anionic phospholipids then prevents AMPs from interacting with the lipid membrane. It has also been suggested that the LPG further inhibits the penetration of AMPs by decreasing the membrane permeability to cationic species.[87] Rehal *et al.* found that at physiological pH, LPG was able to attenuate the activity of magainin. Andrä *et al.* studied the effect of LPG in liposomes and planar bilayers on the behaviour of both helical and β-sheet-forming peptides and found that the functionalization had very different effects on NK-2, melittin, arenecin, of which the first two fold into helices and the third is a β-hairpin.[91] To elucidate the nature of the lipid/AMP interactions at the outer leaflet surface, our study used lipid monolayers coupled with x-ray diffraction techniques and surface IR.

Due the labile nature of the ester linkage in the lysyl-phosphatidyl headgroup,[93,94] a stable synthetic analogue, 1,2-dipalmitoyl-3-azo-dehydroxy lysyl-phosphatidylglycerol (DP3adLPG), was synthesized (Figure 5.1). Whereas prior studies used model membranes comprising dipalmitoylphosphatidylglycerol (DPPG), DP3adLPG, and cardiolipin,[93] the models for this study have been simplified to a two-lipid system consisting of DP3adLPG and DPPG.

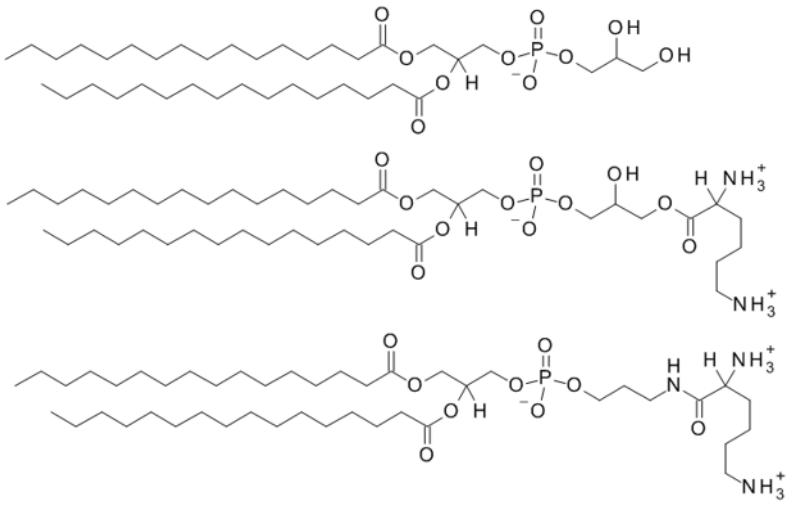

Figure 5.1 Chemical structures of dipalmitoylphosphatidylglycerol (DPPG), lysyl-phosphatidylglycerol (LPG) and 3-aza-dehydroxyl lysyl-phosphatidylglycerol (DP3AdLPG)

Rehal *et al.* found that the proportion of lysyl-phosphatidylglycerol in the membranes of methicillin-resistant strains of *S. aureus* (MRSA) was greater in cultures grown at pH 5.5 as compared to those grown at pH 7.4.[90] The cultures grown at pH 5.5 contained ~55% LPG, while those grown at pH 7.4 contained ~30%. Based on these findings, two representative model mixtures were used, namely DP3AdLPG:DPPG 1:2 and 1:1, with the single component DPPG monolayers used as a control. These monolayers were studied in the absence of peptide then compared to their organization in the presence of peptide. The AMP used was GL13K which is a thirteen-residue cationic peptide with net charge of +5 whose sequence was derived from the human parotid secretory protein (hPSP).[112] Additionally, it preferentially forms extended β-sheets at anionic lipid interfaces,[50,115] so the effect of the lysyl headgroup on peptide self-assembly can be determined.

5.3. Materials and Methods

5.3.1. Materials

The 1,2-dipalmitoyl-*rac*-glycero-3-phosphoglycerol (DPPG) was purchased from Avanti Polar Lipids and DP3AdLPG was synthesized at the Institute of Pharmaceutical Science, King's College London according to the procedure previously reported.[148] Purity was confirmed by

NMR, MS and TLC. Cesium bromide, cesium hydroxide, and EDTA are purchased from Sigma-Aldrich at purity > 98%. GL13K (sequence GKIIKLKASLKLL) was purchased from BioBasic Inc. (ON, Canada) with a purity of > 95%.

Lipid solutions were prepared in HPLC-grade chloroform purchased from Sigma-Aldrich such that final concentrations were 1 mM. The subphase used in all experiments was 1 mM CsBr, 50 μM EDTA, pH adjusted to 7.4 using 1 mM CsOH. To ensure a homogenous distribution of peptide, the subphase was prepared by addition of GL13K from an aqueous stock solution no greater than 2 mg/mL such that the final concentration was 300 nM.

5.3.2. Film preparation

Three lipid films were investigated: pure DPPG, DP3AdLPG:DPPG 1:2, and DP3AdLPG:DPPG 1:1. For all experiments, the lipid spreading solution was prepared from stock spreading solutions of the pure lipids. These mixed spreading solutions were spread on the subphase. For experiments in the absence of the peptide, monolayers were spread in the gaseous phase and subsequently compressed. For experiments with the peptide, the lipid was spread on a peptide containing subphase until a surface pressure of 2-3 mN/m was reached after which peptide absorption was allowed to occur for ninety minutes prior to compression. In all cases the surface pressure increased by 4-5 mN/m with peptide adsorption. The surface behaviour of these films and subsequent behaviour of GL13K were characterized using grazing incidence x-ray diffraction, total reflection x-ray fluorescence and infrared reflection absorption spectroscopy.

5.3.3. Grazing Incidence X-ray Diffraction (GIXD)

GIXD experiments were conducted at beamline P08 at PETRA III of DESY (Hamburg, Germany), where the photon energy was 15 keV (λ = 0.826 Å). The incident beam is set at the grazing incidence α_i = 0.07 degrees. The diffracted signal was measured using a vertically-oriented position sensitive (PSD) detector (MYTHEN, PSI, Villigen, Switzerland) and scanning through 2θ which is correlated to the in-plane component Qxy of the scattering vector $\boldsymbol{Q}$. A Soller collimater was used to limit the in-plane divergence of the diffracted beam to 0.09°. The out-of-plane component Qz of the scattering vector was derived from the position of the PSD channels which spans the range 0.0 to 1.2 $Å^{-1}$. Integration of the Bragg peaks over a defined Qz range and subsequent fitting with Lorentzian functions was used to determine the Bragg peak

position. Similarly, the position of the Bragg rods in Qz was determined by integrating over a defined Qxy range and fitting with a Gaussian function. The tilt of the lipid chains is obtained from the Q_z positions of the peaks, and the in-plane lattice repeat distance were determined using Bragg's law $d = 2\pi/Q\text{xy}$.[107] Data were exported using MATLAB and Bragg peaks and rods were fit using OriginLab.

Experiments were conducted using a temperature-controlled R&K Langmuir trough (Riegler & Kirstein, Potsdam, Germany) at 20 °C.

5.3.4. Total Reflection X-ray Fluorescence (TRXF)

TRXF measurements were conducted on the same films as the GIXD measurements. The X-ray spectra were recorded with an Amptek X-1235DD detector that was set at an offset angle, and the peaks of interest were fit as Lorenztian functions using OriginLab. The intensities of the spectra were determined to be within 5% of each other by comparing the maximum intensities of the Compton (direct beam) peak.

5.3.5. Infrared Reflection Absorption Spectroscopy (IRRAS)

IRRA spectra were measured using a Vertex 70 FT - IR spectrometer (Bruker, Germany) coupled with an R&K Langmuir film balance (Riegler & Kirstein, Potsdam, Germany). The trough and external reflectance unit were sealed in a container to minimize fluctuations in atmosphere and water vapour. Experiments were conducted with an incident IR beam at 40°. Spectra were collected on both a reference trough and a sample trough via a shuttle trough such that 200 scans were co-added for the s-polarized light and 400 scans were co-added for the p-polarized light. Reflected light was detected at an angle equal to the incident angle by a MCT detector with a resolution of 8 cm^{-1}. The spectra are plotted as $-\lg(R/R_0)$, where R is the spectrum of the sample and R_0 is the spectrum of the reference. Spectra were collected every 2 mN/m until a surface pressure of 40 mN/m or greater was reached.

5.4. Results

In the absence of peptide, all three lipid systems exhibit three Bragg peaks, indicating an oblique unit cell with a tilt azimuth between nearest neighbour and next nearest neighbour (Figure 5.2a).

The fitted peak positions and corresponding unit cell parameters are shown in the supplemental information (Supplemental Tables 5.1-5.5).

In the absence of peptide, all films show a typical decrease in the tilt angle as the film is compressed (Figure 5.2b). At all pressures, the tilt angle of DPPG is lower than the tilt angles of the mixtures which are relatively similar to one another. This difference could be attributed to the larger headgroup of the DP3AdLPG but also to the attractive interactions between the negatively-charged PG headgroup and the positive charge of the lysine which has been reported to cause a looping of the headgroup.[93]

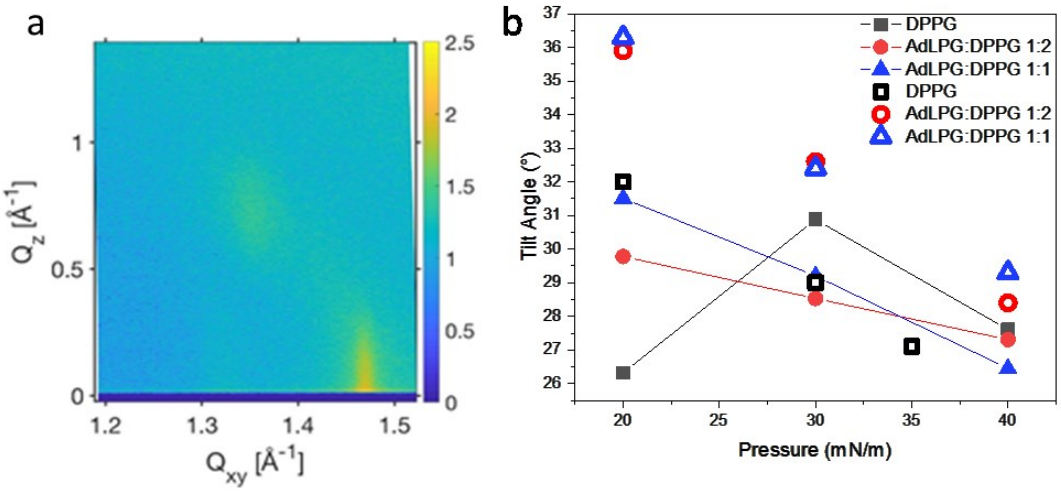

Figure 5.2 GIXD contour plot of the diffraction intensity as a function of the in-plane (Q_{xy}) and out-of-plane (Q_z) components of the scattering vector for DP3AdLPG:DPPG 1:1 in the presence of GL13K at a surface pressure 30 mN/m (a) and calculated tilt angles for each of the films in the absence (open symbols) and presence of peptide (solid symbols) as a function of surface pressure (b)

Although there is no change in the unit cell with the addition of peptide, i.e. it remains an oblique lattice, the GIXD data clearly show the condensing effect of GL13K on the lipid chains at a surface pressure of 20 mN/m as the lipid chains have untilted by 5-6° for all systems. As with the lipid films in the absence of peptide, the DP3AdLPG:DPPG mixtures with peptide all exhibit a linear decrease in tilt angle with increasing pressure. On the other hand, DPPG exhibits an increase in tilt upon compression from 20 to 30 mN/m which may be induced by a partial peptide

squeeze-out from the tail region to the lipid headgroup region. This relocalization of the peptide out of the chain region generates additional space promoting a higher tilt angle. By 40 mN/m, the tilt of the lipid chains for all three systems in the presence of peptide converges at ~27 °, which is still more tilted than DPPG (with peptide) at 20 mN/m. None of the films return to the organization observed in the absence of peptide, even at 40 mN/m, thus even if GL13K is squeezed out of the alkyl chain region, the peptide must still be interacting with the lipid films.

Since GIXD only provides information about crystalline lipid chains, IRRAS was employed to monitor the symmetric CH_2 stretching bands which are sensitive to their environment. The position of the band shifts from 2925 cm^{-1} for more fluid chains to 2919 cm^{-1} for condensed phase chains.[102] Thus, the impact of the peptide on the lipid phase transitions can be determined. As can be seen in Figure 5.3, the addition of the peptide causes both a shift in the phase transition to higher surface pressures and a broadening of the gauche-to-all-trans conformational change, which is more pronounced in the case of DPPG. Such a broadening of the phase transition of DPPG has been observed previously with the β-sheet forming peptide arenicin, where the peptide lies in the plane of the bilayer, but not the α-helical, transmembrane pore forming peptide melittin.[97] The end of the phase transition at 30 mN/m appears to correlate with the removal of the peptide from the alkyl chain region.

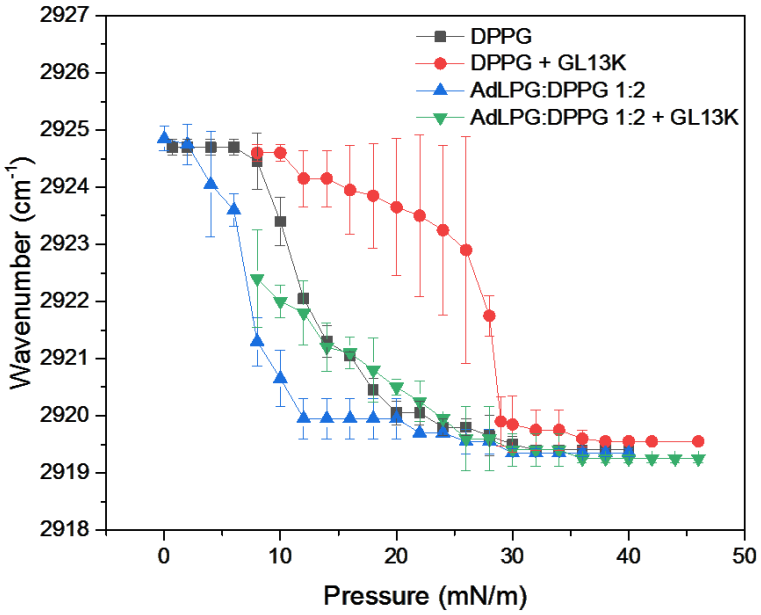

Figure 5.3 Position of the CH_2 asymmetric stretching band from the IRRA spectra of DPPG and DP3AdLPG:DPPG 1:2 in the presence and absence of GL13K as the lipid film is compressed

GIXD and IRRAS showed a significant effect of peptide on DPPG films but a reduced impact on the DP3AdLPG:DPPG mixed films. TRXF provides an indirect method of evaluating the presence of the peptide at the interface by monitoring its displacement of counterions (Cs^+ and Br^-) at the lipid surface. In the absence of peptide, as should be expected with an anionic lipid film, there is significantly more Cs^+ adsorbed at the lipid-subphase interface than Br^- (See Supplemental Table 5.6) and the amount of Cs^+ decreases with decreasing proportion of the anionic DPPG.

For DPPG, the presence of peptide (Figure 5.4) induces a large screening of Cs^+ ions at all surface pressures as the integrated peak intensities are significantly reduced in comparison to the same film in the absence of peptide (Table 5.5). At low surface pressures (5 mN/m) where the peptide is thought to be embedded in the alkyl chain region, the anionic phosphatidylglycerol headgroups would still be sufficiently exposed to attract Cs^+ and repel Br^- from the interface. Once peptide squeeze-out into the headgroup region occurs at 30 mN/m, there is a decrease in

the amount of Cs^+ and a concurrent increase in the amount of Br- detected at the interface. As the pressure increases to 40 mN/m there is a sharp increase in the Cs^+ at the interface (to be discussed below).

The mixtures show neither a large adsorption of Cs^+ ions in the presence of peptide at higher surface pressures. This can be attributed to repulsion either by the presence of the cationic peptide or by the cationic lysyl headgroups. At all surface pressures, the amount of adsorbed Br^- exceeds the amount observed in the absence of peptide and increases as the film is compressed. This supports the hypothesis that GL13K is present in the headgroup region of the lipid monolayers. A significant difference between the 1:1 and 1:2 mixtures can be observed at 30 mN/m, where the 1:1 ratio has significantly more adsorbed Br^-. However, by 40 mN/m the amount of Br^- present is again similar between the two mixtures. In order to understand these changes, the impact of film composition on the secondary structure and organization of the peptide itself must be investigated.

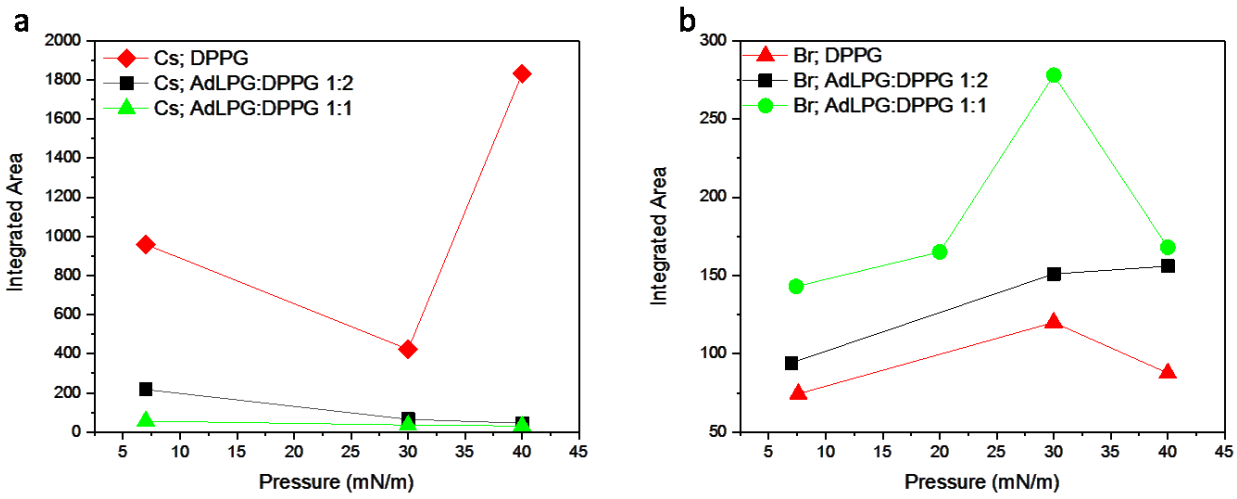

Figure 5.4 Integrated TRXF peak intensities for the cesium ion emission energy bands ($L\alpha_1$,$L\alpha_2$, $L\beta_1$, and $L\beta_2$) and bromide ion emission energy bands ($K\alpha$) for lipid films in the presence of GL13K

Both IRRAS and GIXD can additionally be used to probe the peptide secondary structure since it has been previously shown that GL13K forms crystalline β-sheets (Chapters 3 and 4). Interfacial

crystalline β-sheets have been shown to exhibit a GIXD Bragg peak at Qxy ~1.32 Å which correlates to the interstrand distances.[118,127–129] A relatively weak diffraction peak at approximately Qxy = 1.32 Å is observed for all three lipid films, but not at all surface pressures. For GL13K interacting with the DPPG and DP3AdLPG:DPPG 1:2 films, the peptide only becomes crystalline at higher pressures (see Figure 5.5) as no Bragg peak is observed at surface pressures below 30 mN/m. Notably, the film is more crystalline with DPPG (see correlation lengths given in Table 5.6) and only crystalline at 30 mN/m for DP3AdLPG:DPPG 1:2. Corresponding IRRAS spectra (Figure 5.6) for DPPG films show the appearance of an amide I band at 1619 cm^{-1} indicative of β-sheet formation at pressures greater than 29 mN/m (a similar band was not observed for the DP3AdLPG:DPPG 1:2 mixture, but may be masked by the amide band of the AdLPG headgroup). In the DP3AdLPG:DPPG 1:1, the film with the lowest negative charge, the GIXD shows that it forms crystalline β-sheets at lower surface pressures (20 mN/m) but loses crystallinity with further compression. At high surface pressures, incorporation of DP3AdLPG into the film induces either peptide unfolding or the disruption of extended β-sheets into smaller fragments, both of which could explain the large presence of Br^- at the interface.

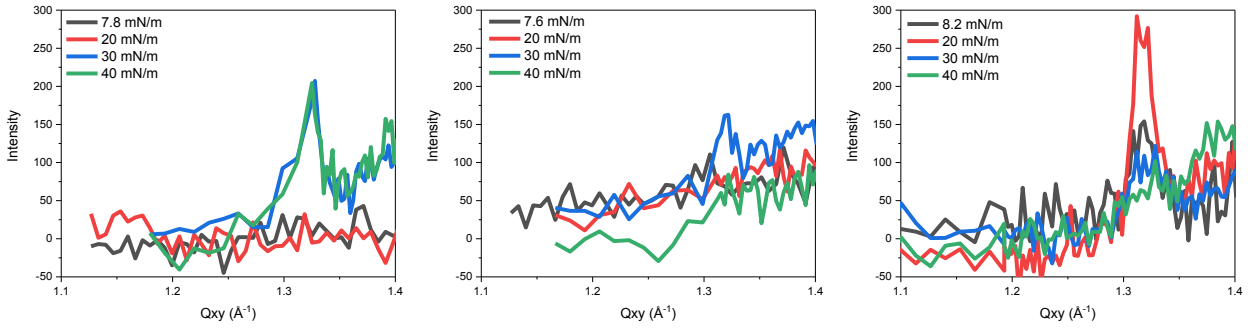

Figure 5.5 GIXD data for DPPG (left), AdLPG:DPPG 1:2 (center), and AdLPG:DPPG 1:1 (right) showing the Qxy range in which crystalline β-sheet diffraction peaks can be found.

5.5. Discussion

At the low concentrations employed, GL13K has low surface activity in the buffer used over the 90 minute time-scale over which the peptide is allowed to adsorb when there is no lipid present, i.e. no significant increase in surface pressure is observed. Thus, any peptide adsorption to the interface that is observed is due to an attraction to the negatively-charged phosphates of the phospholipids This attraction induces the increased pressure during the incubation. There appear to be two different resultant organizational changes occurring, depending on the film composition: with lower proportions of DP3AdLPG, the peptide β-sheets become more crystalline with compression, while in the system for which DP3AdLPG is the majority component, the reverse is true.

In the presence of DPPG, GL13K does not form crystalline β-sheets until ~30 mN/m, at which point it has been squeezed out from the acyl chain region. The crystallinity of GL13K increases with further compression. This suggests that at low surface pressures (< 10 mN/m), while the lipids are still liquid expanded, the amphipathic peptide inserts into the chain region where it has hydrophobic interactions with the acyl chains and electrostatic interactions with the phosphatidylglycerol headgroup. This incorporation of peptide into the membrane enables it to remain unstructured at the air/water interface (amide I band) and concomitantly prevents chain ordering in the lipids (CH_2 stretching band). At the physiologically relevant surface pressure of 30 mN/m, the peptide appears to be squeezed out of the chain region and is trapped among the lipid headgroups where it forms crystalline β-sheets. This increases the charge screening of the headgroups and reduces the amount of bound Cs^+ to the phosphate, while the presence of the exposed cationic peptide concurrently increases the attraction of counterions (Br^-) to the interface. As the surface pressure increases to 40 mN/m, the higher peptide crystallinity and re-balancing of counterions suggests the formation of more localized domains of with a high density of peptide.

The behaviour of GL13K in the DP3AdLPG:DPPG 1:2 is similar to that seen with GL13K and DPPG, with the IRRAS showing a broadened phase transition due to the incorporation of unstructured (GIXD) peptide (GIXD) at low surface pressures and subsequent squeeze-out of the peptide into the headgroup region inducing crystalline β-sheets. The major difference occurs at

40 mN/m where the peptide is no longer crystalline (GIXD). The DP3AdLPG lysine may extend, rather than loop, at higher compressions, which either causes the formation of smaller, less crystalline β-sheets or it drives a proportion of the peptide to unfold into an extended conformation. In either case, the lysyl headgroup does not prevent interaction between GL13K (evident from both the lipid GIXD and the low number of counterions at the interface) and the membrane only modulates perturbation of the acyl chains, which is in agreement with finding with other AMPs.[149]

For the system with the highest proportion of DP3AdLPG, DP3AdLPG:DPPG 1:1, GL13K is already structured into crystalline β-sheets prior to compression. Whereas the other two films have a net negative charge, the situation with DP3AdLPG:DPPG 1:1 is less clear. The alpha amine has been reported to have a pKa of 6.5 such that this amine may be partially charged, leading to a film that is either neutral or has a slight negative net charge. Moreover, this charge could depend on the headgroup conformation and compression state. The ion-pairing of the phosphate with the DP3AdLPG amines clearly reduces the driving force for penetration of the peptide into the acyls chain region, forcing it to reside in the headgroup region. This highlights that the penetration of the peptide into the acyl region is not just based on peptide amphipathicity but requires the electrostatic ion-pairing with the lipid phosphate. Nevertheless, the peptide resides at the interface, as is evident from both GIXD and IRRAS, and still forms crystalline β-sheets. As the film is compressed, the extension of the DP3AdLPG headgroup, rather than looping, exposes the charged amine leading to unfolding or smaller β-sheets, as described above. The greater proportion of DP3AdLPG induces this disruption at lower surface pressures.

The role of the lysyl headgroup in producing bacterial resistance is not as simple as a charge-modulation-preventing interaction. Additionally, one has to discriminate between peptides that insert transmembrane to form pores and those that induce membrane disruption via a carpet and/or detergent mechanism. In the case of the former, the charge of both the membrane and the peptide play a significant role. For example, Andra *et al.* found that while melittin was not affected by the lysyl headgroup, NK-2 was rendered inactive as even its membrane binding capabilities were hindered.[91] Both of these peptides are of similar length (26 and 27 residues, respectively) but they differ in their net charge. While melittin has a net charge of +6, NK-2 has a net charge of +10.[96] This higher concentration of positive charge over a similar surface area (as

they both form helices) may be the reason why NK-2 cannot sufficiently accumulate at the lipid interface to insert transmembrane. Similar to melittin, the bacteriocidal activity of Arenicin, a 21 residue peptide also with a +6 charge, was strongly modulated by the lysyl headgroup.[97] However, it was shown to still bind to the interface. This may be associated with the secondary structure and mechanism of association with the membrane. Arenicin forms a two-stranded antiparallel β-sheet via a β-hairpin which binds laterally at the interface. Its activity (and the activity of a linear derivative), however, derives from its ability to oligomerize and form transmembrane toroidal pores.[150] GL13K has been shown to act via a carpet mechanism[50] and does not orient transmembrane (Chapter 4). For such peptides, the insertion of the peptide into the plane of the monolayer or bilayer causes acyl chain disruption depending on the depth of penetration. The previous work on the interaction of the β-sheet forming arenicin with the lipid bilayer focused only on the shift of the main phase transition by monitoring the acyl chain conformation using IR. We also see the same shift and broadening of the phase transition, however GIXD provides additional evidence that even in the condensed phase, the peptide binding to the headgroups can induce subtle organizational changes within the lipids. Additionally, we were able to show the influence of the DP3AdLPG on the crystallinity of the peptide aggregates bound to the surface.

5.6. Conclusions

The lysylation of the headgroup of DP3AdLPG does not prevent peptide adsorption. However, at biologically relevant surface pressures, it can attenuate the formation of crystalline β-sheets. Higher proportions of AdLPG lower the surface pressure required to observe this effect. The orientation of the DP3AdLPG headgroup appears to be a key parameter, and this is controlled by both compression and composition. DP3AdLPG hinders crystalline β-sheet formation potentially by disrupting the hydrogen bond network once compression and membrane packing have driven it into the lipid headgroup region.

5.7. Supplemental Information

				Peak 1		Peak 2		Peak 3	
Film	Subphase	Pressure (mN/m)		Qxy	Qz	Qxy	Qz	Qxy	Qz
DPPG	CsBr	20	xc	1.351	0.769	1.388	0.657	1.473	0.112
			w	0.067	0.3	0.098	0.3	0.021	0.3
			L_c	85		58		276	
		30	xc	1.384	0.699	1.411	0.602	1.479	0.097
			w	0.080	0.3	0.044	0.3	0.018	0.3
			L_c	71		128		318	
		35	xc	1.400	0.663	1.428	0.549	1.485	0.114
			w	0.066	0.3	0.061	0.3	0.020	0.3
			L_c	86		93		290	
DP3AdLPG:DPPG 1:2	CsBr	20	xc	1.322	0.847	1.331	0.749	1.467	0.098
			w	0.05	0.306	0.087	0.306	0.017	0.306
			L_c	112		65		330	
		30	xc	1.349	0.768	1.367	0.685	1.473	0.083
			w	0.033	0.302	0.620	0.302	0.0180	0.302
			L_c	170		9		313	
		40	xc	1.388	0.692	1.4339	0.591	1.479	0.101
			w	0.064	0.3	0.135	0.3	0.01966	0.3
			L_c	89		42		288	
DP3AdLPG:DPPG 1:1	CsBr	20	xc	1.314	0.812	1.33	0.6656	1.466	0.14717
			w	0.020	0.3	0.041	0.3	0.0161	0.3
			L_c	227		137		351	
		30	xc	1.352	0.768	1.363	0.669	1.472	0.099
			w	0.031	0.3	0.061	0.3	0.0174	0.3
			L_c	184		92		325	
		40	xc	1.381	0.699	1.403	0.618	1.477	0.081
			w	0.044	0.3	0.166	0.3	0.0168	0.3
			L_c	130		34		337	

Table 5.1 GIXD fitted peak position (x_c in $Å^{-1}$), peak width (w) and correlation length (L_c in Å) for Bragg peaks attributed to the lipid chains for all films in the absence of peptide

				Peak 1		Peak 2		Peak 3	
Film	Subphase	Pressure (mN/m)		Qxy	Qz	Qxy	Qz	Qxy	Qz
DPPG	300 nM GL13K CsBr	20	xc	1.375	0.632	1.408	0.511	1.482	0.121
			w	0.027	0.505	0.036	0.505	0.0208	0.505
			L_c	207		158		271	
		30	xc	1.340	0.753	1.388	0.609	1.47324	0.144
			w	0.128	0.340	0.049	0.340	0.01858	0.340
			L_c	44		115		304	
		40	xc	1.373	0.680	1.412	0.517	1.479	0.163
			w	0.033	0.349	0.067	0.349	0.0194	0.349
			L_c	171		84		290	
DP3AdLPG:DPPG 1:2	300 nM GL13K CsBr	20	xc	1.356	0.729	1.388	0.563	1.47252	0.16584
			w	0.034	0.397	0.029	0.397	0.01467	0.397
			L_c	166		193		385	
		30	xc	1.355	0.710	1.443	0.524	1.4715	0.1862
			w	0.062	0.424	0.157	0.424	0.0215	0.42408
			L_c	91		36		263	
		40	xc	1.378	0.70487	1.45916	0.436	1.47575	0.13444
			w	0.062	0.349	0.09951	0.349	0.0218	0.349
			L_c	91		57		259	
DP3AdLPG:DPPG 1:1	300 nM GL13K CsBr	20	xc	1.328	0.75984	1.386	0.607	1.46778	0.15313
			w	0.049	0.47	0.136	0.47	0.02149	0.47
			L_c	115		42		263	
		30	xc	1.353	0.70341	1.442	0.600	1.472	0.103
			w	0.070	0.04256	0.043	0.043	0.020	0.043
			L_c	81		133		287	
		40	xc	1.376	0.632	1.401	0.521	1.476	0.111
			w	0.045	0.349	0.023	0.349	0.02	0.349
			L_c	126		246		283	

Table 5.2 GIXD fitted peak position (x_c, in $Å^{-1}$), peak width (w) and correlation length (L_c in Å) for Bragg peaks attributed to the lipid chains for all films in the presence of peptide

System	Subphase	Pressure	a	b	γ	tilt	Axy
DPPG	CsBr	20	4.99	5.13	115	32.0	23.2
		30	4.96	5.06	116	29.0	22.5
		35	4.92	5.02	117	27.1	22.1
DP3AdLPG:DPPG 1:2	CsBr	20	5.12	5.16	113	36.0	24.3
		30	5.05	5.11	114	32.6	23.5
		40	4.91	5.07	117	28.4	22.2
DP3AdLPG:DPPG 1:1	CsBr	20	5.12	5.18	113	36.3	24.5
		30	5.06	5.10	114	32.4	23.5
		40	4.99	5.04	116	29.2	25.6

Table 5.3 Unit cell and tilt parameters calculated from Bragg peak and Bragg rod positions (Table 5.1) for lipid films in the absence of peptide

System	Subphase	Pressure	a	b	γ	tilt	Axy
DPPG	300 nM GL13K CsBr	20	4.95	5.07	116	26.3	22.6
		30	5.00	5.10	115	30.9	23.1
		40	4.95	5.08	116	27.6	22.6
DP3AdLPG:DPPG 1:2	300 nM GL13K CsBr	20	5.00	5.12	115	29.8	23.2
		30	4.87	5.19	117	28.5	22.6
		40	4.85	5.13	117	27.3	22.1
DP3AdLPG:DPPG 1:1	300 nM GL13K CsBr	20	4.98	5.20	115	31.5	23.6
		30	4.87	5.19	117	29.2	22.6
		40	4.98	5.07	116	26.5	22.8

Table 5.4 Unit cell and tilt parameters calculated from Bragg peak and Bragg rod positions (Table 5.2) for lipid films in the presence of peptide

Fraction DP3adLPG	Integrated Area of Cs^+	Integrated Area of Br^-
0	5640	42
0.33	2594	41
0.5	710	93

Table 5.5 Integrated TRXF peak intensities for the cesium ion emission energy bands ($L\alpha_1$,$L\alpha_2$, $L\beta_1$, and $L\beta_2$) and bromide ion emission energy bands ($K\alpha$) for lipid films at 30 mN/m when no peptide is present

System	Subphase	Pressure (mN/m)	Q_{xy} (Å)	FWHM	L_c (Å)
DPPG	300 nM GL13K CsBr	30	1.324	0.0207	273
		40	1.323	0.0156	363
DP3AdLPG:DPPG 1:2	300 nM GL13K CsBr	30	1.320	0.051	111
DP3AdLPG:DPPG 1:1	300 nM GL13K CsBr	8.2	1.318	0.0260	218
		20	1.318	0.0258	219
		30	1.328	0.0615	92

Table 5.6 Fitted peak position in Q_{xy}, corresponding full width at half maximum (FWHM), and coherent length of the peptide Bragg peak

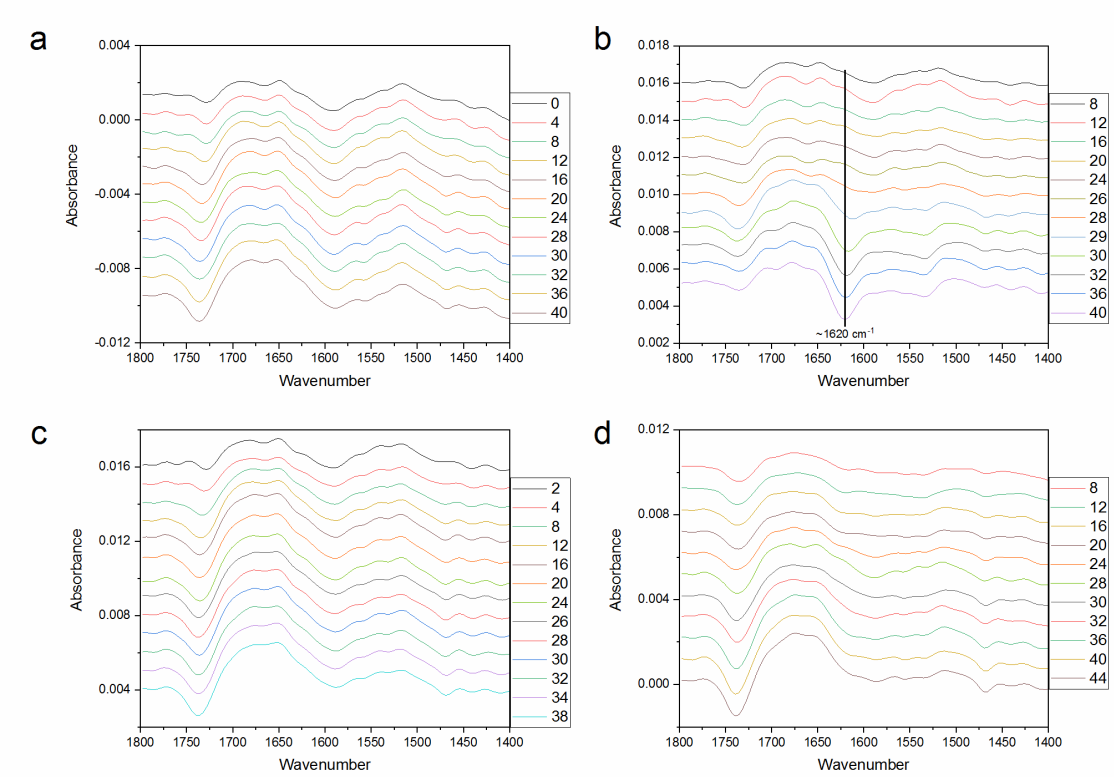

Figure 5.6 IRRA spectra of the amide region of DPPG (a and b) and DP3AdLPG:DPPG 1:2 (c and d) in the absence and presence of peptide, respectively

Chapter 6. Conclusions and Future Directions

6.1. Interfacial secondary structure of GL13K

Until recently, GL13K had only been characterized in solution. Our studies thus far with GL13K at the air/water interface have demonstrated that it is a short cationic AMP that preferentially forms crystalline anti-parallel β-sheets at interfaces.

In Chapter 3, we showed that compression induces the tilting of the peptide which results in the loss of β-sheet crystallinity. While the peptide remained in β-sheets at the interface, the positively-charged lysine residues must prevent the peptide from packing into well-defined structures.

GL13K did not assemble into fibrils at the interface or when transferred to solid support. While crystalline β-sheet formation has been observed in other β-sheet peptides, most of these peptides are crystalline in two directions. GL13K is only crystalline in one direction and does not organize in the head-to-tail direction, neither at the bare interface nor in the presence of lipids. Arenicin, a β-hairpin peptide, also forms crystalline sheets in two directions as does its linear derivative, C/S Ar-1, however, it appears that it also forms a turn, despite the loss of the disulfide bridge.[120]

In addition to lacking the head-to-tail ordering, GL13K also loses crystallinity upon compression. Multiple factors including GL13K's short length, +5 charge, and the lysine on its hydrophobic face contributed to this behaviour. The deprotonation of this lysine in particular at higher pH may explain why Ye *et al.* observed extensive fibril formation.[116] An approach to determine the extent of the importance of a cationic residue at this position would be to perform similar surface assembly studies with GL13K analogues with different residues at this position. It would be particularly interesting to compare the glutamine variant as GL13NH2 (native sequence) and GL13D/N both have glutamine in this position and previous work has shown that variation of as little as one residue between GL13NH2 and GL13D/N can change the membrane specificity of a peptide and its mechanism of action.[49] Similarly, the impact of membrane composition on potential fibril formation should be investigated.

6.2. Headgroup localization and peptide crystallinity

Given that AMPs are thought to target compositional differences in membranes, it was essential to characterize peptide organization and influence on model membranes. Specifically, we investigated the interaction of GL13K with anionic lipid monolayers. In fluid, anionic membranes, GL13K formed crystalline β-sheets with correlation lengths greater than those observed in the absence of phospholipids. This suggests that the electrostatic interactions between the lysine side chains and the phosphatidylglycerol headgroups stabilize the peptide's supramolecular organization. This electrostatic interaction induces the adsorption of low concentrations of peptide.

In Chapter 4, we showed that GL13K preferentially inserts into both the headgroup and tail regions of the phospholipid monolayer and that greater space-filling nature of the branched lipids did not prevent peptide penetration into the acyl chains but did modulate the angle of insertion. Cholesterol increased membrane viscosity by inducing local ordering and, subsequently, prevented peptide insertion beyond the headgroup region. The forced localization would prevent the "flip and dip" transition[151] where the peptide reorients itself at the interface to bury its hydrophobic face in the acyl chain region. This leaves the hydrophobic residues exposed and drove the peptide to form more crystalline β-sheets. Our x-ray data suggest that additional peptides adsorb from the subphase and provide the hydrophobic interactions to stabilize the peptide bound to the membrane interface. Previous bilayers studies suggested that GL13K drove aggregation of DOPG:Ch 60:40 liposomes (DLS data and visualized by cryo-TEM).[49] The results of Chapter 4 support this hypothesis (Figure 6.1) and suggest that the exposed hydrophobic face of the peptide surface bound in the headgroup region could be responsible for inducing this aggregation via the hydrophobic effect. Whether the peptide crystallinity contributes to his effect has yet to be investigated.

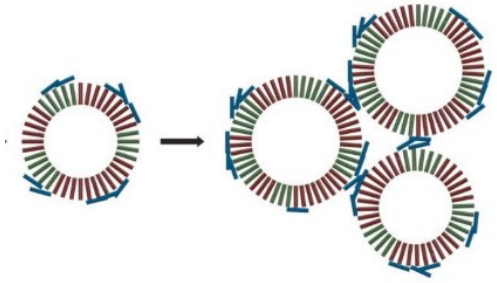

Figure 6.1 Schematic representation of mechanism of attack proposed by V. Balhara when GL13K interacts with DOPG:Ch 60:40

6.3. Relationship between β-sheet crystallinity and peptide function

There does not appear to be a direct correlation between peptide crystallinity and peptide activity as GL13K is most crystalline when trapped among lipid headgroups. While peptides can still disrupt membranes via more discrete mechanisms like charged lipid clustering and membrane thinning/thickening (Figure 1.4), GL13K causes the most membrane disruption when it inserts into the acyl tail region. Neutron diffraction has been used to follow such changes[90,152–154] and could be used to identify the mechanisms of disruption for GL13K in crystalline β-sheet, β-strand and random forms.

The lack of direct correlation between crystallinity and peptide activity is also shown in Chapter 5 as peptide crystallinity wa influenced by both lipid composition, lipid density, charge dilution and the lysyl functionalization of DP3AdLPG. In the pure anionic (DPPG) film, GL13K does not fold into crystalline β-sheets until the film was compressed to physiologically-relevant surface pressures when it was forced into the headgroup region, much like what was observed with the DOPG films. The β-sheets must be stabilized by the phospholipid headgroups or else crystallinity would be lost much like what was observed in Chapter 1. The presence of DP3AdLPG modulated, but did not prevent, the adsorption of the peptide at the membrane interface. The orientation of the lysyl headgroup, which can loop back on itself or extend from the membrane surface, and the corresponding exposure of the cationic charge appear to be critical in defining the interaction with the peptide. More extensive IRRAS or PM-IRRAS experiments studying the headgroup orientation of AdLPG in each of the mixtures are required to characterize the looping and unlooping of the lysyl headgroup. Deuteration of the lysyl

headgroup would shift IR absorption so that the secondary structure of GL13K can be resolved beyond the crystallinity of β-sheets. NMR studies with labelled-headgroups or peptides would also contribute to this discussion and may explain the driving force behind the loss of crystallinity that was observed with increasing proportions of lysyl-phosphatidylglycerol and compression of the DP3AdLPG-containing films. X-ray reflectivity would contribute information about the localization of GL13K in each of these membranes. The effect of the lysylation appears to extend beyond mere electrostatic repulsion given that GL13K adsorbed to all three films and the shift in surface pressure during the incubation period was comparable between all three films.

The model membranes studied in this thesis were limited to binary systems in an attempt to design a bottom-up approach by which the mechanism and specificity of GL13K could be clarified. However, these models are not representative of the complexity in composition of bacterial membranes. While the membranes are predominately negatively charged, membrane composition varies even between species of bacteria.[51,52] None of the models discussed in this work addressed the contribution of phosphatidylethanolamine headgroups in bacteria,[51] especially since the ethanolamine headgroup is smaller than the PG headgroup.[155]

S.-U. Gorr and collaborators synthesized an all D-enantiomer version of GL13K whose bactericidal activity is greater than that of GL13K.[156] D-peptides are of current interest due to the proposed ability to evade proteolysis.[157,158] Moreover, the chiral environment of the lipid membrane may induce changes to the interaction of the peptide at the interface. While Zhou *et al.* found that D-GL13K peptides are more susceptible to fibril formation at higher pH, at this time little to no information has been published about the mechanism of insertion of this D-peptide.[116]

A sequence modification that may improve the activity of GL13K (either enantiomer) would be to substitute one or more of the lysine residues with arginine residues. While both residues are cationic, it has been observed that arginine interacts more strongly with anionic phospholipids that lysine.[159] Simulations have suggested that while the amino group in lysine only interacts with the phosphate of phospholipids, arginine interacts with both the phosphate and the

glycerols.[160] Again, single and multiple substitutions would provide information about the relative contributions of each of the lysine residues.

Finally, the influence of GL13 peptide sequence on secondary structure and peptide/lipid interactions has not been studied beyond the work of Abdelhosseni and Balhara.[49,112] The GL13 peptides GL13NH2, GL13DN, and GL13K vary in three or fewer residues and they all have very different activities. GL13K is bactericidal, while GL13NH2 and GL13DN are both bacteria-agglutinating and hemoagglutinating, however, only GL13DN is hemolytic. Biophysical characterization with model membranes has shown that unlike GL13K which interacts preferentially as β-sheets with negatively-charged membranes and remains unstructured in buffer and in the presence of zwitterionic liposomes, GL13NH2 and GL13D/N shows less specificity and appear to favour α-helical structures even in buffer.[49] Investigation of these differences in preferred secondary structures will contribute to the discussion of the relationship between sequence and structure and can lead to the development of more effective peptide antimicrobial agents.

References

(1) Davies, J.; Davies, D. *Microbiology and Molecular Biology Reviews* **2010**, *74* (3), 417–433.

(2) Laxminarayan, R.; Duse, A.; Wattal, C.; Zaidi, A. K. M.; Wertheim, H. F. L.; Sumpradit, N.; Vlieghe, E.; Hara, G. L.; Gould, I. M.; Goossens, H.; Greko, C.; So, A. D.; Bigdeli, M.; Tomson, G.; Woodhouse, W.; Ombaka, E.; Peralta, A. Q.; Qamar, F. N.; Mir, F.; Kariuki, S.; Bhutta, Z. A.; Coates, A.; Bergstrom, R.; Wright, G. D.; Brown, E. D.; Cars, O. *The Lancet Infectious Diseases* **2013**, *13* (12), 1057–1098.

(3) WHO. Antimicrobial resistance: Fact sheet http://www.who.int/mediacentre/factsheets/fs194/en/ (accessed May 8, 2019).

(4) Reardon, S. *Nature News* **2014**, *509* (7499), 141–142.

(5) WHO. *Antimicrobial Resistance Global Report on Surveillance*; Geneva, 2014.

(6) O'Neill, J. *Antimicrobial Resistance: Tackling a crisis for the health and wealth of nations*; 2014.

(7) Zasloff, M. *Nature* **2002**, *415* (6870), 389–395.

(8) Wang, G. *Pharmaceuticals* **2013**, *6* (6), 728–758.

(9) Department of Pathology and Microbiology, UNMC. A Brief Guide to the APD http://aps.unmc.edu/AP/about.php (accessed Feb 11, 2017).

(10) Duclohier, H.; Molle, G.; Spach, G. *Biophysical Journal* **1989**, *56* (5), 1017–1021.

(11) Ketchem, R. R.; Lee, K. C.; Huo, S.; Cross, T. A. *Journal of Biomolecular NMR* **1996**, *8* (1), 1–14.

(12) Townsley, L. E.; Tucker, W. A.; Sham, S.; Hinton, J. F. *Biochemistry* **2001**, *40* (39), 11676–11686.

(13) Iwadate, M.; Asakura, T.; Dubovskii, P. V; Yamada, H.; Akasaka, K.; Williamson, M. P. *Journal of Biomolecular NMR* **2001**, *19* (2), 115–124.

(14) Andrä, J.; Jakovkin, I.; Grötzinger, J.; Hecht, O.; Krasnosdembskaya, A. D.; Goldmann, T.; Gutsmann, T.; Leippe, M. *Biochemical Journal* **2008**, *410* (1), 113–122.

(15) Mani, R.; Waring, A. J.; Lehrer, R. I.; Hong, M. *Biochimica et Biophysica Acta (BBA) - Biomembranes* **2005**, *1716* (1), 11–18.

(16) Kawano, K.; Yoneya, T.; Miyata, T.; Yoshikawa, K.; Tokunaga, F.; Terada, Y.; Iwanaga, S. *Journal of Biological Chemistry* **1990**, *265* (26), 15365–15367.

(17) Knappe, T. a.; Linne, U.; Zirah, S.; Rebuffat, S.; Xie, X.; Marahiel, M. A. *Journal of the American Chemical Society* **2008**, *130* (17), 11446–11454.

(18) Iwatsuki, M.; Tomoda, H.; Uchida, R.; Gouda, H.; Hirono, S.; Omura, S. *Journal of the American Chemical Society* **2006**, *128* (23), 7486–7491.

(19) Ashrafuzzaman, M.; Andersen, O. S.; McElhaney, R. N. *Biochimica et Biophysica Acta - Biomembranes* **2008**, *1778* (12), 2814–2822.

(20) Trabi, M.; Schirra, H. J.; Craik, D. J. *Biochemistry* **2001**, *40* (14), 4211–4221.

(21) Barbosa, S. C.; Cilli, E. M.; Dias, L. G.; Stabeli, R. G.; Ciancaglini, P. *Amino Acids* **2011**, *40* (1), 135–144.

(22) Mohanram, H.; Bhattacharjya, S. *Biochimica et Biophysica Acta - General Subjects* **2014**, *1840* (10), 3006–3016.

(23) Zhang, X.-J.; Zhang, X.-Y.; Zhang, N.; Guo, X.; Peng, K.-S.; Wu, H.; Lu, L.-F.; Wu, N.; Chen, D.-D.; Li, S.; Nie, P.; Zhang, Y.-A. *The Journal of Immunology* **2015**, *194* (10), 4974–4987.

(24) Fázio, M. A.; Oliveira, V. X.; Bulet, P.; Miranda, M. T. M.; Daffre, S.; Miranda, A. *Biopolymers* **2006**, *84* (2), 205–218.

(25) Qiang, W.; Yau, W.-M.; Schulte, J. *Biochimica et Biophysica Acta (BBA) - Biomembranes* **2015**, *1848* (1), 266–276.

(26) Zhang, M.; Zhao, J.; Zheng, J. *Soft Matter* **2014**, *10* (38), 7425–7451.

(27) Dobson, C. M.; Giannoni, E.; Baroni, F.; Chiti, F.; Ramponi, G.; Zurdo, J.; Formigli, L.; Stefani, M.; Bucciantini, M.; Taddei, N. *Nature* **2002**, *416* (6880), 507–511.

(28) Kayed, R.; Eichhoff, G.; Adelsberger, H.; Abramowski, D.; Wiederhold, K.-H.; Haass, C.; Staufenbiel, M.; Konnerth, A.; Garaschuk, O. *Science* **2003**, *300* (5618), 486–489.

(29) Eisenberg, D.; Jucker, M. *Cell* **2012**, *148* (6), 1188–1203.

(30) Thakur, G.; Micic, M.; Leblanc, R. M. *Colloids and Surfaces B: Biointerfaces* **2009**, *74* (2), 436–456.

(31) Murphy, M. P.; LeVine III, H. *Journal of Alzheimer's Disease* **2010**, *19* (1), 1–17.

(32) Goedert, M. *Science* **2015**, *349* (6248), 125555550–125555559.

(33) Lopez de la Paz, M.; Goldie, K.; Zurdo, J.; Lacroix, E.; Dobson, C. M.; Hoenger, A.; Serrano, L. *Proceedings of the National Academy of Sciences* **2002**, *99* (25), 16052–16057.

(34) Hung, N. B.; Le, D.; Hoang, T. X. *The Journal of Chemical Physics* **2017**, *147* (10), 105102.

(35) Jang, H.; Arce, F. T.; Mustata, M.; Ramachandran, S.; Capone, R.; Nussinov, R.; Lal, R. *Biophysical Journal* **2011**, *100* (7), 1775–1783.

(36) Sato, H.; Feix, J. B. *Biochimica et Biophysica Acta (BBA) - Biomembranes* **2006**, *1758* (9), 1245–1256.

(37) Zhu, M.; Liu, P.; Niu, Z.-W. W. *Chinese Chemical Letters* **2017**, *28* (4), 703–708.

(38) Cirac, A. D.; Moiset, G.; Mika, J. T.; Koçer, A.; Salvador, P.; Poolman, B.; Marrink, S. J.; Sengupta, D. *Biophysical Journal* **2011**, *100* (10), 2422–2431.

(39) Lohner, K.; Prenner, E. J. *Biochimica et Biophysica Acta (BBA) - Biomembranes* **1999**, *1462* (1–2), 141–156.

(40) Epand, R. M.; Epand, R. F. *Journal of Peptide Science* **2011**, *17* (5), 298–305.

(41) Haney, E. F.; Nathoo, S.; Vogel, H. J.; Prenner, E. J. *Chemistry and Physics of Lipids* **2010**, *163* (1), 82–93.

(42) Gifford, J. L.; Hunter, H. N.; Vogel, H. J. *Cellular and Molecular Life Sciences* **2005**, *62* (22), 2588–2598.

(43) Nguyen, L. T.; Haney, E. F.; Vogel, H. J. *Trends in Biotechnology* **2011**, *29* (9), 464–472.

(44) Bingle, C. D.; Seal, R. L.; Craven, C. J. *Biochemical Society Transactions* **2011**, *39* (4), 977–983.

(45) Geetha, C.; Venkatesh, S. G.; Fasciotto Dunn, B. H.; Gorr, S.-U. *Biochemical Society Transactions* **2003**, *31* (4), 815–818.

(46) Gorr, S. U.; Sotsky, J. B.; Shelar, A. P.; Demuth, D. R. *Peptides* **2008**, *29* (12), 2118–2127.

(47) Abdolhosseini, M.; Sotsky, J. B.; Shelar, A. P.; Joyce, P. B. M.; Gorr, S.-U. *Molecular and Cellular Biochemistry* **2012**, *359* (1–2), 1–8.

(48) Shelar, A. P. Characterization of Biological Activities and Toxicity of Synthetic Peptides Derived From Parotid Secretory Protein (PSP), University of Louisville, 2009.

(49) Balhara, V. Mechanism of Interaction of Human Parotid Secretory Protein - Derived Antimicrobial Peptides : A Biophysical Insight, Concordia University, 2014.

(50) Balhara, V.; Schmidt, R.; Gorr, S.-U.; DeWolf, C. *Biochimica et Biophysica Acta (BBA) - Biomembranes* **2013**, *1828* (9), 2193–2203.

(51) Malanovic, N.; Lohner, K. *Biochimica et Biophysica Acta (BBA) - Biomembranes* **2016**, *1858* (5), 936–946.

(52) Sohlenkamp, C.; Geiger, O. *FEMS Microbiology Reviews* **2015**, *40* (1), 133–159.

(53) Van Meer, G.; Voelker, D. R.; Feigenson, G. W. *Nature Reviews Molecular Cell Biology* **2009**, *101* (1), 1–4.

(54) Pokorny, A.; Almeida, P. F. F. *Biochemistry* **2005**, *44* (27), 9538–9544.

(55) Mouritsen, O. G.; Zuckermann, M. J. *Lipids* **2004**, *39* (11), 1101–1113.

(56) McMullen, T. P. W.; Lewis, R. N. A. H.; McElhaney, R. N. *Current Opinion in Colloid and Interface Science* **2004**, *8* (6), 459–468.

(57) Prenner, E. J.; Lewis, R. N. A. H.; Jelokhani-Niaraki, M.; Hodges, R. S.; McElhaney, R. N. *Biochimica et Biophysica Acta (BBA) - Biomembranes* **2001**, *1510* (1–2), 83–92.

(58) Zhao, H.; Sood, R.; Jutila, A.; Bose, S.; Fimland, G.; Nissen-Meyer, J.; Kinnunen, P. K. J. *Biochimica et Biophysica Acta (BBA) - Biomembranes* **2006**, *1758* (9), 1461–1474.

(59) Henderson, J. M.; Iyengar, N. S.; Lam, K. L. H.; Maldonado, E.; Suwatthee, T.; Roy, I.; Waring, A. J.; Lee, K. Y. C. *Biochimica et Biophysica Acta (BBA) - Biomembranes* **2019**, *1861* (10), 182977.

(60) Ohvo-Rekilä, H.; Ramstedt, B.; Leppimäki, P.; Slotte, J. P. *Progress in Lipid Research* **2002**, *41* (1), 66–97.

(61) Shinoda, W.; Mikami, M.; Baba, T.; Hato, M. *Chemical Physics Letters* **2004**, *390*, 35–40.

(62) Pilotelle-Bunner, A.; Beaunier, P.; Tandori, J.; Maroti, P.; Clarke, R. J.; Sebban, P. *Biochimica et Biophysica Acta (BBA) - Bioenergetics* **2009**, *1787* (8), 1039–1049.

(63) McConnell, H. M.; Radhakrishnan, A. *Biochimica et Biophysica Acta (BBA) - Biomembranes* **2003**, *1610* (2), 159–173.

(64) Ratajczak, M. K.; Chi, E. Y.; Frey, S. L.; Cao, K. D.; Luther, L. M.; Lee, K. Y. C.; Majewski, J.; Kjaer, K. *Physical Review Letters* **2009**, *103* (2), 028103.

(65) Chong, P. L. *Proceedings of the National Academy of Sciences* **1994**, *91* (21), 10069–

10073.

(66) Huang, J. *Biophysical Journal* **2002**, *83* (2), 1014–1025.

(67) Jurak, M. *Journal of Physical Chemistry B* **2013**, *117* (13), 3496–3502.

(68) McMullen, T. P. W.; Lewis, R. N. A. H.; McElhaney, R. N. *Biochimica et Biophysica Acta (BBA) - Biomembranes* **2009**, *1788* (2), 345–357.

(69) Kahya, N.; Schwille, P. *Journal of Fluorescence* **2006**, *16* (5), 671–678.

(70) Bag, N.; Yap, D. H. X.; Wohland, T. *Biochimica et Biophysica Acta (BBA) - Biomembranes* **2014**, *1838* (3), 802–813.

(71) Wu, Y.; Štefl, M.; Olzyńska, A.; Hof, M.; Yahioglu, G.; Yip, P.; Casey, D. R.; Ces, O.; Humpolíčková, J.; Kuimova, M. K. *Physical Chemistry Chemical Physics* **2013**, *15* (36), 14986–14993.

(72) Mitchell, N. J.; Seaton, P.; Pokorny, A. *Biochimica et Biophysica Acta (BBA) - Biomembranes* **2016**, *1858* (5), 988–994.

(73) Tristram-Nagle, S.; Kim, D. J.; Akhunzada, N.; Kučerka, N.; Mathai, J. C.; Katsaras, J.; Zeidel, M.; Nagle, J. F. *Chemistry and Physics of Lipids* **2010**, *163* (6), 630–637.

(74) Driessen, A. J. M.; van de Vossenberg, J. L. C. M.; Konings, W. N. *FEMS Microbiology Reviews* **1996**, *18* (2–3), 139–148.

(75) Balleza, D.; Garcia-Arribas, A. B.; Sot, J.; Ruiz-Mirazo, K.; Goñi, F. M. *Biophysical Journal* **2014**, *107* (6), 1364–1374.

(76) Hung, W. C.; Chen, F. Y.; Huang, H. W. *Biochimica et Biophysica Acta (BBA) - Biomembranes* **2000**, *1467* (1), 198–206.

(77) Andersson, M.; Jackman, J.; Wilson, D.; Jarvoll, P.; Alfredsson, V.; Okeyo, G.; Duran, R. *Colloids and Surfaces B: Biointerfaces* **2011**, *82* (2), 550–561.

(78) Lindsey, H.; Petersen, N.; Chan, S. I. *Biochimica et Biophysica Acta (BBA) -*

Biomembranes **1979**, *555* (1), 147–167.

(79) Valincius, G.; McGillivray, D. J.; Febo-Ayala, W.; Vanderah, D. J.; Kasianowicz, J. J.; Lösche, M. *The Journal of Physical Chemistry B* **2006**, *110* (21), 10213–10216.

(80) Huang, H. W.; Wu, Y. *Biophysical Journal* **1991**, *60* (5), 1079–1087.

(81) Paulmann, M.; Arnold, T.; Linke, D.; Özdirekcan, S.; Kopp, A.; Gutsmann, T.; Kalbacher, H.; Wanke, I.; Schuenemann, V. J.; Habeck, M.; Bürck, J.; Ulrich, A. S.; Schittek, B. *Journal of Biological Chemistry* **2012**, *287* (11), 8434–8443.

(82) Chen, F. Y.; Lee, M. T.; Huang, H. W. *Biophysical Journal* **2002**, *82* (2), 908–914.

(83) Wu, Y.; He, K.; Ludtke, S. J.; Huang, H. W. *Biophysical Journal* **1995**, *68* (6), 2361–2369.

(84) Pasupuleti, M.; Schmidtchen, A.; Malmsten, M. *Critical Reviews in Biotechnology* **2012**, *32* (2), 143–171.

(85) Nizet, V. *Journal of Allergy and Clinical Immunology* **2007**, *120* (1), 13–22.

(86) LaRock, C. N.; Nizet, V. *Biochimica et Biophysica Acta (BBA) - Biomembranes* **2015**, *1848* (11), 3047–3054.

(87) Roy, H. *IUBMB Life* **2009**, *61* (10), 940–953.

(88) Ernst, C. M.; Staubitz, P.; Mishra, N. N.; Yang, S. J.; Hornig, G.; Kalbacher, H.; Bayer, A. S.; Kraus, D.; Peschel, A. *PLoS Pathogens* **2009**, *5* (11), 1–9.

(89) Goldfine, H. *Virulence* **2014**, *5* (4), 451–453.

(90) Rehal, R. P.; Marbach, H.; Hubbard, A. T. M.; Sacranie, A. A.; Sebastiani, F.; Fragneto, G.; Harvey, R. D. *Chemistry and Physics of Lipids* **2017**, *206*, 60–70.

(91) Andrä, J.; Goldmann, T.; Ernst, C. M.; Peschel, A.; Gutsmann, T. *Journal of Biological Chemistry* **2011**, *286* (21), 18692–18700.

(92) Tocanne, J. F.; Ververgaert, P. H. J. T.; Verkleij, A. J.; van Deenen, L. L. M. *Chemistry and Physics of Lipids* **1974**, *12* (3), 201–219.

(93) Rehal, R.; Gaffney, P. R. J.; Hubbard, A. T. M.; Barker, R. D.; Harvey, R. D. *European Journal of Pharmaceutical Sciences* **2019**, *128*, 43–53.

(94) Cox, E.; Michalak, A.; Pagentine, S.; Seaton, P.; Pokorny, A. *Biochimica et Biophysica Acta (BBA) - Biomembranes* **2014**, *1838* (9), 2198–2204.

(95) Fjell, C. D.; Hiss, J. A.; Hancock, R. E. W.; Schneider, G. *Nature Reviews Drug Discovery* **2012**, *11* (1), 37–51.

(96) Gross, S.; Wilms, D.; Krause, J.; Brezesinski, G.; Andrä, J. *Journal of Peptide Science* **2013**, *19* (10), 619–628.

(97) Travkova, O. G.; Andrä, J.; Möhwald, H.; Brezesinski, G. *Langmuir* **2013**, *29* (39), 12203–12211.

(98) Langmuir, I. *Journal of the American Chemical Society* **1917**, *39* (9), 1848–1906.

(99) Marsh, D. *Biochimica et Biophysica Acta (BBA) - Reviews on Biomembranes* **1996**, *1286* (3), 183–223.

(100) Mendelsohn, R.; Flach, C. R. In *Handbook of Vibrational Spectroscopy*; Griffiths, P. R., Ed.; John Wiley & Sons, Ltd: Chichester, UK, 2006; Vol. 46, pp 305–334.

(101) Barth, A. *Biochimica et Biophysica Acta (BBA) - Bioenergetics* **2007**, *1767* (9), 1073–1101.

(102) Mendelsohn, R.; Mao, G.; Flach, C. R. *Biochimica et Biophysica Acta (BBA) - Biomembranes* **2010**, *1798* (4), 788–800.

(103) Blume, A. *ChemTexts* **2018**, *4* (1), 3.

(104) Blaudez, D.; Buffeteau, T.; Cornut, J. C.; Desbat, B.; Escafre, N.; Pezolet, M.; Turlet, J. M. *Applied Spectroscopy* **1993**, *47* (7), 869–874.

(105) Blaudez, D.; Castano, S.; Desbat, B. In *Biointerface Characterization by Advanced IR Spectroscopy*; Elsevier, 2011; pp 27–55.

(106) Stefaniu, C.; Brezesinski, G. *Current Opinion in Colloid & Interface Science* **2014**, *19* (3), 216–227.

(107) Jensen, T. R.; Kjaer, K. In *Novel Methods to Study Interfacial Layers*; Mobius, D., Miller, R., Eds.; Elsevier B.V: Amsterdam, 2001; Vol. 11, pp 205–254.

(108) Dutta, P. *Special Section: Surface Characterization* **2000**, *78* (12), 1478–1483.

(109) Lavoie, H.; Blaudez, D.; Vaknin, D.; Desbat, B.; Ocko, B. M.; Salesse, C. *Biophysical Journal* **2002**, *83* (6), 3558–3569.

(110) Hönig, D.; Möbius, D. *Thin Solid Films* **1992**, *210–211* (PART 1), 64–68.

(111) Motschmann, H.; Helmuth, M. In *Handbook of Applied Surface and Colloid Chemistry*; 2001; pp 629–648.

(112) Abdolhosseini, M.; Nandula, S. R.; Song, J.; Hirt, H.; Gorr, S.-U. *Peptides* **2012**, *35* (2), 231–238.

(113) Hirt, H.; Gorr, S.-U. *Antimicrobial Agents and Chemotherapy* **2013**, *57* (10), 4903–4910.

(114) Chen, X.; Hirt, H.; Li, Y.; Gorr, S.-U.; Aparicio, C. *PLoS ONE* **2014**, *9* (11), e111579.

(115) Harmouche, N.; Aisenbrey, C.; Porcelli, F.; Xia, Y.; Nelson, S. E. D.; Chen, X.; Raya, J.; Vermeer, L.; Aparicio, C.; Veglia, G.; Gorr, S.; Bechinger, B. *Biochemistry* **2017**, *56* (32), 4269–4278.

(116) Ye, Z.; Zhu, X.; Acosta, S.; Kumar, D.; Sang, T.; Aparicio, C. *Nanoscale* **2019**, *11* (1), 266–275.

(117) Do, T. D.; LaPointe, N. E.; Economou, N. J.; Buratto, S. K.; Feinstein, S. C.; Shea, J.-E.; Bowers, M. T. *The Journal of Physical Chemistry B* **2013**, *117* (37), 10759–10768.

(118) Chi, E. Y.; Frey, S. L.; Winans, A.; Lam, K. L. H.; Kjaer, K.; Majewski, J.; Lee, K. Y. C.

Biophysical Journal **2010**, *98* (10), 2299–2308.

(119) Olak, C.; Muenter, A.; Andrä, J.; Brezesinski, G. *Journal of Peptide Science* **2008**, *14* (4), 510–517.

(120) Travkova, O. G.; Andrä, J.; Möhwald, H.; Brezesinski, G. *ChemPhysChem* **2010**, *11* (15), 3262–3268.

(121) Behyan, S.; Borozenko, O.; Khan, A.; Faral, M.; Badia, A.; DeWolf, C. *Environmental Science: Nano* **2018**, *5* (5), 1218–1230.

(122) Bu, W.; Mihaylov, M.; Amoanu, D.; Lin, B.; Meron, M.; Kuzmenko, I.; Soderholm, L.; Schlossman, M. L. *Journal of Physical Chemistry B* **2014**, *118* (43), 12486–12500.

(123) Bourque, H.; Laurin, I.; Pézolet, M.; Klass, J. M.; Lennox, R. B.; Brown, G. R. *Langmuir* **2001**, *17* (19), 5842–5849.

(124) Blaudez, D.; Turlet, J.-M.; Dufourcq, J.; Bard, D.; Buffeteau, T.; Desbat, B. *Journal of the Chemical Society, Faraday Transactions* **1996**, *92* (4), 525–530.

(125) Leon, L.; Logrippo, P.; Tu, R. *Biophysical Journal* **2010**, *99* (9), 2888–2895.

(126) Lepère, M.; Chevallard, C.; Hernandez, J. F.; Mitraki, A.; Guenoun, P. *Langmuir* **2007**, *23* (15), 8150–8155.

(127) Vaiser, V.; Rapaport, H. *Journal of Physical Chemistry B* **2011**, *115* (1), 50–56.

(128) Rubinov, B.; Wagner, N.; Rapaport, H.; Ashkenasy, G. *Angewandte Chemie - International Edition* **2009**, *48* (36), 6683–6686.

(129) Mosca, S.; Dannehl, C.; Möginger, U.; Brezesinski, G.; Hartmann, L. *Organic & Biomolecular Chemistry* **2013**, *11* (33), 5399–5403.

(130) Lepère, M.; Muenter, A. H.; Chevallard, C.; Guenoun, P.; Brezesinski, G. *Colloids and Surfaces A: Physicochemical and Engineering Aspects* **2007**, *303* (1–2), 73–78.

(131) Shin, S.; Ahn, S.; Cheng, J.; Chang, H.; Jung, D. H.; Hyun, J. *Applied Surface Science*

2016, *388*, 551–556.

(132) Jiang, Z.; Vasil, A. I.; Hale, J. D.; Hancock, R. E. W.; Vasil, M. L.; Hodges, R. S. *Biopolymers* **2008**, *90* (3), 369–383.

(133) Michael Henderson, J.; Lee, K. Y. C. *Current Opinion in Solid State and Materials Science* **2013**, *17* (4), 175–192.

(134) Stefaniu, C.; Brezesinski, G.; Möhwald, H. *Advances in Colloid and Interface Science* **2014**, *208*, 197–213.

(135) Als-Nielsen, J.; Jacquemain, D.; Kjaer, K.; Leveiller, F.; Lahav, M.; Leiserowitz, L. *Physics Reports* **1994**, *246* (5), 251–313.

(136) Demers, É.; Boisselier, É.; Horchani, H.; Blaudez, D.; Calvez, P.; Cantin, L.; Belley, N.; Champagne, S.; Desbat, B.; Salesse, C. *Biochemistry* **2015**, *54* (16), 2560–2570.

(137) Chi, E. Y.; Ege, C.; Winans, A.; Majewski, J.; Wu, G.; Kjaer, K.; Lee, K. Y. C. *Proteins: Structure, Function, and Bioinformatics* **2008**, *72* (1), 1–24.

(138) Davies, J. T.; Rideal, E. K. *Interfacial Phenomena*; Academic Press: New York, NY, 1963.

(139) Matti, V.; Säily, J.; Ryhänen, S. J.; Holopainen, J. M.; Borocci, S.; Mancini, G.; Kinnunen, P. K. J. *Biophysical Journal* **2001**, *81* (4), 2135–2143.

(140) Alvares, D. S.; dos Santos Cabrera, M. P.; Ruggiero Neto, J. In *Advances in Biomembranes and Lipid Self-Assembly*; Elsevier Inc., 2016; Vol. 24, pp 43–73.

(141) Travkova, O. G.; Moehwald, H.; Brezesinski, G. *Advances in Colloid and Interface Science* **2017**, *247* (June), 521–532.

(142) Neville, F.; Ishitsuka, Y.; Hodges, C. S.; Konovalov, O.; Waring, A. J.; Lehrer, R.; Lee, K. Y. C.; Gidalevitz, D. *Soft Matter* **2008**, *4* (8), 1665–1674.

(143) Garten, M.; Prévost, C.; Cadart, C.; Gautier, R.; Bousset, L.; Melki, R.; Bassereau, P.;

Vanni, S. *Physical Chemistry Chemical Physics* **2015**, *17* (24), 15589–15597.

(144) Valincius, G.; Heinrich, F.; Budvytyte, R.; Vanderah, D. J.; McGillivray, D. J.; Sokolov, Y.; Hall, J. E.; Lösche, M. *Biophysical Journal* **2008**, *95* (10), 4845–4861.

(145) Sood, R.; Kinnunen, P. K. J. *Biochimica et Biophysica Acta (BBA) - Biomembranes* **2008**, *1778* (6), 1460–1466.

(146) Bechinger, B.; Gorr, S.-U. *Journal of Dental Research* **2017**, *96* (3), 254–260.

(147) van der Does, A. M.; Beekhuizen, H.; Ravensbergen, B.; Vos, T.; Ottenhoff, T. H. M.; van Dissel, J. T.; Drijfhout, J. W.; Hiemstra, P. S.; Nibbering, P. H. *The Journal of Immunology* **2010**, *185* (3), 1442–1449.

(148) Rehal, R. P. A Physicochemical and Biophysical Investigation Into the Role of Lysyl-phosphatidylglycerol in the Membrane of Staphylococcus aureus Under Mild Acidic Conditions, King's College London, 2014.

(149) Kilelee, E.; Pokorny, A.; Yeaman, M. R.; Bayer, A. S. *Antimicrobial Agents and Chemotherapy* **2010**, *54* (10), 4476–4479.

(150) Shenkarev, Z. O.; Balandin, S. V.; Trunov, K. I.; Paramonov, A. S.; Sukhanov, S. V.; Barsukov, L. I.; Arseniev, A. S.; Ovchinnikova, T. V. *Biochemistry* **2011**, *50* (28), 6255–6265.

(151) Reid, K. A.; Davis, C. M.; Brian Dyer, R.; Kindt, J. T. *Biochimica et Biophysica Acta (BBA) - Biomembranes* **2017**, *1860* (3), 792–800.

(152) Nielsen, J. E.; Bjørnestad, V. A.; Lund, R. *Soft Matter* **2018**, *14* (43), 8750–8763.

(153) Chen, X.; Liu, S.; Deme, B.; Cristiglio, V.; Marquardt, D.; Weller, R.; Rao, P.; Wang, Y.; Bradshaw, J. *Biochimica et Biophysica Acta (BBA) - Biomembranes* **2017**, *1859* (5), 910–916.

(154) Sharma, V. K.; Mamontov, E.; Anunciado, D. B.; O'Neill, H.; Urban, V. S. *Soft Matter* **2015**, *11* (34), 6755–6767.

(155) Wydro, P.; Flasiński, M.; Broniatowski, M. *Biochimica et Biophysica Acta (BBA) - Biomembranes* **2012**, *1818* (7), 1745–1754.

(156) Hirt, H.; Hall, J. W.; Larson, E.; Gorr, S. U. *PLoS ONE* **2018**, *13* (3), 1–16.

(157) Hamamoto, K.; Kida, Y.; Zhang, Y.; Shimizu, T.; Kuwano, K. *Microbiology and immunology* **2002**, *46* (11), 741–749.

(158) Oliva, R.; Chino, M.; Pane, K.; Pistorio, V.; De Santis, A.; Pizzo, E.; D'Errico, G.; Pavone, V.; Lombardi, A.; Del Vecchio, P.; Notomista, E.; Nastri, F.; Petraccone, L. *Scientific Reports* **2018**, *8* (1), 8888.

(159) Takechi, Y.; Tanaka, H.; Kitayama, H.; Yoshii, H.; Tanaka, M.; Saito, H. *Chemistry and Physics of Lipids* **2012**, *165* (1), 51–58.

(160) Wu, Z.; Cui, Q.; Yethiraj, A. *The Journal of Physical Chemistry B* **2013**, *117* (40), 12145–12156.